Stability tests of opto-electronic systems for use in the SLHC:

Radiation and temperature effects on performance

Jessica Elizabeth Hanzlik

December 17, 2011

Thesis submitted to the Faculty of the Graduate School

of the University of Oxford

in partial fulfillment of the requirements for the degree

of Masters of Science by Research in Particle Physics

Abstract

Stability tests of opto-electronic systems for use in the SLHC: Radiation and temperature effects on performance

Jessica Elizabeth Hanzlik

St. John's College

Masters of Science by Research in Particle Physics

Michaelmas Term 2010

The Large Hadron Collider (LHC) located at CERN is the world's most powerful particle accelerator, with plans to collide protons at a center of mass energy of 14 TeV. These proton-proton collisions occur within particle detectors located around the circumference of the accelerator. After approximately 10 years of running at this energy, the LHC accelerator will be upgraded to the super-LHC and it will be necessary to upgrade the constituent particle detectors, in particular the CMS and ATLAS detector experiments. The innermost layers of these detectors will have experienced a very high radiation environment over an extended period of time and will have reached the maximum radiation dose for which they were designed. Upgrades to the accelerator will increase the radiation dose rate and total dose experienced by the detectors, which will demand both increased radiation-hardness of detector components and improved detector performance to handle the increased data rate driven by accelerator upgrades.

This thesis presents results of tests performed as a part of the research and development of the LHC upgrade. In particular, we report on the optical fibres to be used in the readout systems of the inner detectors. Fibres were tested for performance variability in high radiation and temperature-variant environments.

Acknowledgements

I am immensely grateful to my supervisors Todd Huffman, Cigdem Issever, and Tony Weidberg for their patience and support throughout the research process and in particular for their continued support even as I chose not to continue in physics. The lessons and skills I've learned from struggling with recalcitrant lab equipment and my own inefficient analysis techniques will forever stand me in good stead.

As I wouldn't have had the opportunity to come to study at the University of Oxford without the generous support of the Rhodes Trust, I feel incredibly privileged to have been given the chance to explore my passions.

A wonderful component of life at Oxford is the thriving intellectual community, and so I also owe many thanks to my fabulous friends and classmates. I didn't expect discussions over tea and scones to provide such intellectual and social satisfaction as they have done and continue to do.

My family has always been unquestionably supportive of me throughout every decision I've ever made and every action I've ever taken. None of that changed as I entered graduate school and for that lasting stability I feel much love and gratitude.

Frederick Kuehn inspires me daily with his love and encouragement. I wouldn't have struggled through the countless particle physics problem sets without his help and I can't imagine a better model for how to approach graduate school, and life.

I wouldn't be at this point in my life without the support structure provided by a huge community of people at Ohio State University and beyond, all of whom want me to succeed and be happy. I'm sorry I can't name them individually but that doesn't diminish my indebtedness. Thank you.

Contents

1 Introduction **1**

2 Theory **5**
2.1 Light propagation in glass fibres 5
2.1.1 Geometrical optics 6
2.1.2 Maxwell's equations 7
2.1.3 Single-mode and multimode fibres 10
2.2 Contributions to attenuation of light in optical fibres 14
2.2.1 Radiative loss 14
2.2.2 Scattering 15
2.2.3 Absorption 16
2.3 Radiation damage 18
2.3.1 Bulk radiation damage 18
2.3.2 Ionizing radiation damage 19
2.3.3 Annealing 19

3 Experimental Setup **21**
3.1 Basic components 21
3.1.1 Single mode fibres 22
3.1.2 Multimode fibres 22
3.1.3 Versatile Link Common Project 23
3.1.4 Additional components used 23
3.2 Experimental apparatuses 25
3.2.1 Mode scramblers 25
3.2.2 Temperature-controlled environments 27

4 Results of laboratory tests **30**
4.1 Instabilities in the multimode system 30
4.1.1 Linear correlations in the data 35
4.1.2 Laser mode hopping 41
4.1.3 Mode scrambler tests 43
4.1.4 ModCon tests 49
4.1.5 Uncorrected and corrected data 55
4.2 Temperature-induced instabilities 59
4.2.1 Previous results 59

4.2.2 Temperature-variant regions of the SLHC 64
4.2.3 Temperature-dependent behaviour of fibre systems 64

5 Radiation tests **79**
5.1 Motivation 79
5.2 Test 1 82
5.2.1 Fibres under test 82
5.2.2 Region 1: Coolers on, radiation off 86
5.2.3 Region 2: Coolers on, radiation on 88
5.2.4 Region 3: Coolers on, radiation off 90
5.2.5 Region 4: Coolers on, radiation on 92
5.2.6 Region 5: Coolers off, radiation on 94
5.2.7 Conclusions 96
5.3 Test 2 97
5.3.1 Upgrades to the cooler vessel 97
5.3.2 Fibres under test 97
5.3.3 Region 1: Coolers on, radiation off 104
5.3.4 Region 2: Coolers on, radiation on 109
5.3.5 Region 3: Coolers on, radiation off 114
5.3.6 Region 4: Coolers off, radiation off 118
5.3.7 Region 5: Coolers on, radiation off 119
5.3.8 Region 6: Coolers on, radiation on 120
5.3.9 Second-order temperature dependence 124
5.3.10 Tentative conclusions from Test 2 134

6 Conclusions and future work **136**

A Derivation of Maxwell's Equations in an Infinite Dielectric Cylindrical Waveguide **138**
A.1 Maxwell's equations 138
A.2 Solutions to the differential equations 138
A.3 Waves in a waveguide 139
A.4 Wave equations for step-index fibre 141

List of Figures

2.1 Transverse plane projections of power distribution in cylindrical waveguides. 10

2.2 Transmission windows in optical fibres as a function of the wavelength of the propagating light. 17

3.1 A picture of the FM-1 Mode Scrambler. 26

3.2 A picture of the Arden Photonics Modal Controller. 28

3.3 Design Environmental Model A3721-Alpha 335-40H. 28

4.1 A schematic of the experimental setup. 31

4.2 Raw data for all four channels of the splitter. 32

4.3 Raw data for system without splitter. 33

4.4 Schematic of connector experimental setup. 34

4.5 Histogram of raw data for all four channels of the splitter; G_i and G_j. RMS values for Ch. 1: 0.05585, Ch. 2: 0.04777, Ch. 3: 0.07092, and Ch. 4: 0.1064. 36

4.6 Histogram of raw data for system without splitter; calculated using G_j. RMS values for one connector: 0.0008352 and two connectors: 0.001091. . 37

4.7 Scatter plots of splitter channels using reference. 38

4.8 Corrected data for all four channels of the splitter. 39

4.9 Histogram of corrected data for all four channels of the splitter; G_i'; RMS values Ch. 1: 0.05585, Ch. 2: 0.03274, Ch. 3: 0.05443, and Ch. 4: 0.08774. 40

4.10 Schematic of mode-scrambling experimental setup. 43

4.11 Mode scrambler: Output of splitter with the mode scrambler set to 7.0. . . 44

4.12 Mode scrambler: Histograms of the splitter outputs for the mode scrambling device. 45

4.13 Mode scrambler: Scatter plots of the data with linear correlation indicated. 46

4.14 Mode scrambler: Corrected output of splitter. 47

4.15 Mode scrambler: Corrected histograms of the splitter outputs 48

4.16 ModCon: Outputs from the splitter for the ModCon device. 50

4.17 ModCon: Histograms of the splitter outputs for the ModCon device. . . . 51

4.18 ModCon: Scatter plots comparing the output of the channels, with linear fit. 52

4.19 ModCon: Splitter outputs corrected for laser instability. 53

4.20 ModCon: Corrected histograms of the splitter outputs. 54

4.21 Attenuation of fibre in 2008 test: full run. 59

4.22 Temperature of fibre in 2008 test: full run. 60

4.23 Attenuation and temperature of the four multimode fibres under test over the 1st 6 hours of interest. 61

4.24 The relative power variation of one channel in multimode system with one connector. 66

4.25 The relative power variation of one channel in multimode system with two connectors. 66

4.26 The relative power variation of one channel in singlemode system with one connector. 66

4.27 The distribution in power of a singlemode system with one connector. . . 67

4.28 Temperature and attenuation profiles during single-mode and multimode coupler tests. 71

4.29 Schematic of how 1x4 couplers are constructed. 72

5.1 Schematic of cooler vessel. 81

5.2 Timeline of Test 1 with regions indicated. 83

5.3 Schematic of the test set-up at the SCK-CEN facility. 84

5.4 Test 1: The temperature of and attenuation of light in the Draka fibre over hours 0-51. 85

5.5 Test 1: The attenuation of light in and temperature of the Draka fibre over hours 0-17. 86

5.6 Test 1: Correlation of attenuation and temperature in the Draka fibre over hours 0-17. 87

5.7 Test 1: The attenuation of light in and temperature of the Draka fibre over hours 17-49. 88

5.8 Test 1: Correlation of attenuation and temperature of the Draka fibre over hours 17-49. 89

5.9 Test 1: The temperature of the Draka fibre over hours 49-51. 90

5.10 Test 1: Correlation of attenuation and temperature of the Draka fibre over hours 49-51. 91

5.11 Test 1: The temperature of the Draka fibre over hours 51-54. 92

5.12 Test 1: Correlation of attenuation and temperature of the Draka fibre over hours 51-54. 93

5.13 Test 1: The attenuation of light in and temperature of the Draka fibre over hours 53-66. 94

5.14 Test 1: Correlation of temperature and attenuation of the Draka fibre over hours 53-66. 95

5.15 Both references taken during Test 2 vs. time. 98

5.16 Schematic of vessel. 99

5.17 Full run of Infinicor SX+ fibre with regions of interest labelled. 100

5.18 Full run of Draka fibre with regions of interest labelled. 101

5.19 Zoomed-in section of Infinicor SX+ fibre with regions of interest labelled. . 102

5.20 Zoomed-in section of Draka fibre with regions of interest labelled. 103

5.21 Test 2: The attenuation of light in and temperature of the Infinicor SX+ fibre over hours 0 to 17. 105

5.22 Test 2: Correlation of attenuation and temperature in the Infinicor SX+ fibre over hours 0 to 17. . . . 106

5.23 Test 2: The attenuation of light in and temperature of the Draka fibre over hours 0 to 17. . . . 107

5.24 Test 2: Correlation of attenuation and temperature in the Draka fibre over hours 0 to 17. . . . 108

5.25 Test 2: The attenuation of light in and temperature of the Draka fibre over hours 17 to 42. . . . 110

5.26 Test 2: Correlation of attenuation and temperature in the Draka fibre over hours 17 to 42. . . . 111

5.27 Test 2: The attenuation of light in and temperature of the Infinicor SX+ fibre over hours 17 to 42. . . . 112

5.28 Test 2: Correlation of attenuation and temperature in the Infinicor SX+ fibre over hours 17 to 42. . . . 113

5.29 Test 2: The attenuation of light in and temperature of the Draka fibre over hours 42 to 46. . . . 114

5.30 Test 2: Correlation of attenuation and temperature in the Draka fibre over hours 42 to 46. . . . 115

5.31 Test 2: The attenuation of light in and temperature of the Infinicor SX+ fibre over hours 42 to 46. . . . 116

5.32 Test 2: Correlation of attenuation and temperature in the Infinicor SX+ fibre over hours 42 to 46. . . . 117

5.33 Test 2: The attenuation of light in and temperature of the Draka fibre over hours 46 to 70. . . . 120

5.34 Test 2: Correlation of attenuation and temperature in the Draka fibre over hours 46 to 70. . . . 121

5.35 Test 2: The attenuation of light in and temperature of the Infinicor SX+ fibre over hours 46 to 70. . . . 122

5.36 Test 2: Correlation of attenuation and temperature in the Infinicor SX+ fibre over hours 46 to 70. . . . 123

5.37 Test 2: The attenuation of light in and temperature of the Draka fibre over hours 5 to 6. . . . 125

5.38 Test 2: Correlation of attenuation and temperature in the Draka fibre over hours 5 to 6. 126

5.39 Test 2: The attenuation of light in and temperature of the Infinicor SX+ fibre over hours 5 to 6. 127

5.40 Test 2: Correlation of attenuation and temperature in the Infinicor SX+ fibre over hours 5 to 6. 128

5.41 Test 2: The attenuation of light in and temperature of the Draka fibre over hours 25 to 26. 129

5.42 Test 2: Correlation of attenuation and temperature in the Draka fibre over hours 25 to 26. 131

5.43 Test 2: The attenuation of light in and temperature of the Infinicor SX+ fibre over hours 25 to 26. 132

5.44 Test 2: Correlation of attenuation and temperature in the Infinicor SX+ fibre over hours 25 to 26. 133

A.1 Cylindrical coordinate system. 140

List of Tables

2.1 Typical fibre types and specifications. 13

4.1 RMS values for uncorrected and corrected data. 55

4.2 Pearson r^2 values for correlations among channels. 56

4.3 Temperature and radiation in the regions of interest for SMF-28 at SCK-CEN, 2008. 63

4.4 Stability of the individual regions (excluding transitions): Single-mode. 73

4.5 Stability of the individual regions (excluding transitions): Multimode. 74

4.6 Stability of the individual regions: Temperature. 75

4.7 Results from connector tests, optical grease tests, and temperature variation tests for multimode fibres: RMS of the attenuation. 76

4.8 Results from connector tests, mode scrambler tests, and modCon tests for multimode fibre: RMS of the attenuation. 77

4.9 RMS of the variation in output (in dB) for mode scrambler settings. 78

5.1 Radiation and temperature properties of the regions shown in Figure 5.2. 85

5.2 Radiation and temperature properties of the regions shown in Figures 5.17, 5.18, 5.19, and 5.20. 100

5.3 Temperature and RIA variations of fibres. 130

Chapter 1

Introduction

The Large Hadron Collider (LHC) at CERN came online in November 2009. The particle physics community worldwide awaited this switching-on of the world's most powerful particle accelerator with excitement, for it is predicted and hoped that many advances to the state of knowledge about particle physics will be made. Although the LHC has, as of this writing, only begun operation, research and development for its upgrade, the Super-LHC (SLHC) has already commenced [3]. Full development of the upgrade plans is not possible until the LHC has been in operation long enough both for its scientists to gain familiarity with the workings of the various detectors and components and for potential new discoveries about the fundamental nature of the universe to be made, as these factors will guide specific decisions about upgrade options. However, because development of new detector technology takes years, work has already begun on many components of the SLHC [22], [32].

The LHC is a circular particle accelerator located on the border of France and

Switzerland. With a circumference of 27 km, it will collide two beams of protons at a centre of mass energy of $\sqrt{s} = 14$ TeV. These beam collisions will occur at several different points around the circumference of the accelerator, inside of the particle detectors which have been constructed to measure various properties of the results of these collisions. There are two general-purpose detectors at the LHC: ATLAS (A Toroidal LHC ApparatuS) and CMS (Compact Muon Solenoid). The author is a member of the ATLAS collaboration. Both of these detectors and their affiliated collaborations of physicists aim to discover new physics. The 14 TeV centre of mass energy of the proton-proton collisions is signifiantly larger than the current $\sqrt{s} = 2$ TeV proton-antiproton collisions occurring at the Fermi National Accelerator Laboratory in the United States. Both ATLAS and CMS expect to process a predicted average of 25 interactions per proton-proton bunch crossing at a rate of 25 ns between crossings. This rate will result in a peak luminosity of 10^{34} $\text{cm}^{-2}\text{s}^{-1}$ [6].

After nominally 10 years of running at LHC levels, the SLHC aims to increase the luminosity by a factor of 10 to 10^{35} $\text{cm}^{-2}\text{s}^{-1}$. The time interval between bunch crossings will likely increase from 25 ns to 50 ns, and so from the 25 interactions per bunch crossing seen at the LHC, the SLHC detectors will need to process on order 400 interactions per bunch crossing. This upgrade will result in a 20 – 30% improvement for the mass reach of new physics, e.g. SUSY (Super Symmetry) and extra dimensions [3], [47], [8], [41]. The higher event rates will lead to better statistics and stronger signals in the data. However, the improvement in physics reach comes at a significant cost to detector performance as many of the components

will already be operating at their maximum capacities merely at the LHC levels [37], [33].

In particular, the inner detectors (IDs) of both ATLAS and CMS will need to be completely replaced as the existing IDs will have reached the end of their lifetimes in the high-radiation environment close to the beamline, and additionally, new detector-technology developments will be necessary to handle the increased event (proton-proton collision) rate. Specifically, the optoelectronic readout system which transfers the data collected by the inner detectors to the outside world for processing will need to be extremely radiation hard and have a high bandwidth capable of supporting the increase in data rate. In addition to being sufficiently radiation hard to withstand the high fluences of the inner detector, any optical fibres used in the readout system will track through various regions of the detector which will be maintained at both warm and cold temperatures ($-25\,^{\circ}\mathrm{C}$ to $30\,^{\circ}\mathrm{C}$) [32], [37].

These major concerns for the performance of the detectors in the LHC upgrade motivated a series of tests designed to parametrize the feasibility of components of optoelectronic systems for use in the SLHC detectors. In particular, lack of understanding of the interrelated effects of temperature and radiation on fibre performance indicated that there were questions which needed to be answered, and this report details the results of tests on optoelectronic fibre system performance in radiation and temperature-controlled environments.

Section 2 discusses the theory of light propagation in fibre and models for describing radiation-induced attenuation in fibres. Section 3 discusses the basic

constituents of a system of fibre optoelectronics and describes the experimental apparatuses used in the various tests. Sections 4 and 5 present first the results from laboratory tests carried out at the Universiy of Oxford on the stability of the components of the optoelectronic fibre system and then the results and implications of two cold radiation test runs conducted at the SCK-CEN facility[1] over the summer of 2009. Finally, Section 6 briefly concludes and summarizes the results as well as indicating future directions the research may take.

[1]The SCK-CEN facility, or Belgian Nuclear Research Centre, is one of the largest nuclear research facilities in Belgium. It provides resources for universities to conduct research at their nuclear reactors and laboratories.

Chapter 2

Theory

2.1 Light propagation in glass fibres

Optical glass fibres are generally made of silica (amorphous silicon dioxide SiO_2). The structure of glass consists of a randomly-alligned assortment of molecules, as opposed to the geometric, structurally-ordered, allignment of crystals [20], [31]. This lack of order contributes to light attenuation in optical glass fibres as discussed in Section 2.2.

The glass fibre core is surrounded by a layer of cladding which has a slightly smaller index of refraction than the fibre. The pure SiO_2 can be doped with an oxide to produce a second mixture with a slightly different index of refraction to be used as either the core or cladding in conjunction with the pure silicon dioxide. These optical fibres act as dielectric waveguides for the propagation of light launched into their cores. In thinking about the way in which light propagates down a fibre, it is useful to consider two approaches to describing light: the geometrical optics

approach and the electromagnetic theory of Maxwell's equations (also known as the wave optics) approach [31].

2.1.1 Geometrical optics

In the geometrical optics approach to understanding the physics of light, a ray perpendicular to the wave fronts emanating from the light source is drawn. The ray shows the direction in which the energy is flowing. Propagation of a beam of light down an optical wave guide (glass fibre) can, to first order, be understood with rays as well.

While the speed of light in vacuum is constant, $c = 3 \times 10^8$ m/s, when light travels through a medium its speed is modified according to n, the refractive index of the material. The velocity of light in a medium with refractive index n is given by $v = c/n$. For glass, n is approximately equal to 1.5 (e.g. $n(SiO_2) = 1.458$ for $\lambda = 850$ nm where λ is the wavelength of the light) [31].

When a ray of light encounters a boundary between two media of differing indices of refraction, the ray may be reflected internally in the first medium and it may continue, refracted (bent), in the second medium. The refraction can be understood by thinking about the wavefronts of light that the ray represents traveling at a different velocity in the new medium. The familiar Snell's Law, Equation 2.1, quantifies the relationship between the angle of incidence and the angles of reflection and refraction.

$$n_1 \times \sin\theta_1 = n_2 \times \sin\theta_2 \tag{2.1}$$

For angles of incidence larger than what is called the critical angle, Snell's Law appears to break down by demanding that $\sin\theta_2$ be greater than 1. Clearly this is not the case; rather, this indicates that the entirety of the light ray is reflected internally. It is this angle which it is necessary to achieve if waveguides are to successfully transmit a beam of light over any reasonable distance.

2.1.2 Maxwell's equations

The ray picture of optics breaks down when we consider that the boundary conditions of the waveguide limit the allowed solutions of Maxwell's equations to a discrete number of guided "modes" [11].

To understand the physics behind the modal distribution of the light waves propagating down the fibre, it is necessary to examine the solutions to Maxwell's equations, subject to the boundary conditions of a cylindrical waveguide.

One of the boundary conditions demands that the tangential and normal components of the electric and magnetic fields are respectively continuous at the boundary. This requirement leads to solutions to Maxwell's equations of the form where the fields in the cladding layer decay exponentially and the fields in the core layer oscillate. The exponentially decaying fields in the cladding layer exist because while total internal reflection constrains the oscillating waves to within the waveguide, the E and B fields must be continuous at the boundary. Thus, on the other side of the

boundary the wave must take the form of a nonvanishing, non-travelling wave.

These exponentially decaying fields can lead to evanescent power coupling which is a classical effect whereby under the right conditions, the evanescent field gives rise to propagating modes of light. This effect will be described in more detail in Section 3.1.4. These solutions are limited to a discrete number of what are termed modes. To understand the discretized nature of the modal distribution it is helpful to think about reflection of the plane wave at the surface between the core and cladding layers. The plane wave is a complex function and its phase changes when it reflects. Since the condition for wave propagation is that all points of a wave front have the same phase, only waves incident on the boundary with appropriate angles of incidence will propagate, leading to optical fibres supporting only a finite number of modes. Equations 2.2, 2.3, 2.4, 2.5, and 2.6 indicate the requirements for wave propagation in an infinite dielectric cylindrical waveguide of radius a, and their derivation is presented in Appendix A.

The wave equation for E_z in cylindrical co-ordinates subject to the boundary conditions of a step-index fibre becomes

$$\frac{\partial^2 E_z}{\partial \rho^2} + \frac{1}{\rho}\frac{\partial E_z}{\partial \rho} + \frac{1}{\rho^2}\frac{\partial^2 E_z}{\partial \phi^2} + q^2 E_z = 0. \tag{2.2}$$

Equation 2.2 is a differential equation whose solutions are Bessel functions. The same analysis holds for H_z.

Step index fibres have a core of radius a with a uniform refractive index and a cladding layer with a lower refractive index. For regions inside the core, the solu-

tions are finite as the radius r $\rightarrow$ 0. Outside of the core, the solutions $\rightarrow$ 0 as r $\rightarrow \infty$.

Thus for r $\leq$ a, the solutions are Bessel functions of the first kind of order ν. For these solutions we use the designator $J_\nu(ur)$ where $u^2 = k_1^2 - \beta^2; k_1 = \frac{2\pi n_1}{\lambda}$.

Inside of the core

$$E_z(r < a) = AJ_\nu(ur)\exp(j\nu\phi)\exp[j(\omega t - \beta z)] \tag{2.3}$$

$$H_z(r < a) = BJ_\nu(ur)\exp(j\nu\phi)\exp[j(\omega t - \beta z)]. \tag{2.4}$$

Outside of the core the solutions to the wave equation are modified Bessel functions of the second kind: $K_\nu(wr)$, where $w^2 = \beta^2 - k_2^2; k_2 = \frac{2\pi n_2}{\lambda}$.

Thus outside of the core

$$E_z(r > a) = CK_\nu(wr)\exp(j\nu\phi)\exp[j(wt - \beta z)] \tag{2.5}$$

$$H_z(r > a) = DK_\nu(wr)\exp(j\nu\phi)\exp[j(wt - \beta z)]. \tag{2.6}$$

The derivation of these equations are is presented in Appendix A.

Figure 2.1 provides a way of visualising some of the simpler modal distributions allowed by Maxwell's equations in an infinite dielectric cylindrical waveguide [1]. In this figure, m and l represent the number of zero crossings of the electric field intensity distributions in the azimuthal and radial directions, respectively. The cross-section of the core of the fibre is shown in the darker pigments while the cladding is shown in lighter pigments.

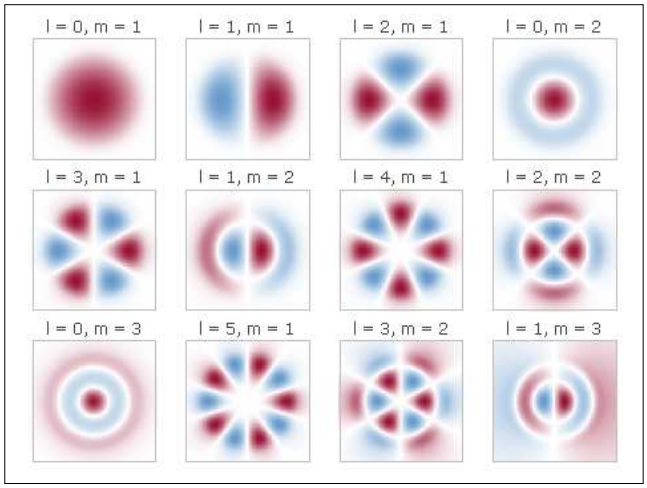

Figure 2.1: Transverse plane projections of power distribution in cylindrical waveguides.

The order of a mode corresponds to the number of nodes (zeros of the wave function in the plane transverse to the direction of propagation) and higher order modes correspond to rays incident at steeper angles. The higher order modes penetrate further into the cladding layer and hence contribute more to mode coupling effects. Mode coupling effects are the exchanges of optical power among the propagating modes of light [31], [11].

2.1.3 Single-mode and multimode fibres

Optical fibres fall into two broad categories based on how many modes of light they support. The most basic of optical fibres is the single-mode fibre. This fibre supports one transverse mode of light, the lowest order mode. These single-mode fibres have a core with a uniform index of refraction n_1 and a cladding layer with a different, also uniform, index of refraction n_2. So that single-mode fibres cannot

support multiple transverse modes of light, they tend to have a very narrow core, and in the idealised case, the beam of light launched into the fibre travels along the z-axis through the centre of the fibre as a single ray. An advantage of single-mode fibres is that the data can be transmitted at a very high bandwidth since the pulses of light experience little spreading in time (dispersion), as compared to multimode fibres which will be described below. However, because single-mode fibres only support one mode of light, the light-gathering capacity of single-mode fibres is low and they tend to need brighter, more expensive sources of light.

The second category of optical fibre is the multimode fibre. As the name suggests, these fibres support multiple transverse modes of light and will have a larger core radius than the single-mode fibres. Multimode fibres can be either step-index or graded-index fibres. Step-index fibres, like single mode fibres, have a core with a uniform index of refraction n_1 and a cladding layer with a different, also uniform, index of refraction n_2. In this case, the behaviour of the light launched into the multimode fibre obeys the ray-optics picture of light propagation. Each of the supported modes can be represented by a single ray incident to the core-cladding interface at a slightly different angle. The uniform index of refraction of the core means that the velocity of each ray is the same, $v = c/n$, but because some rays have steeper angles than others, those rays traverse a greater distance as they propagate down the fibre. The rays which have a greater total distance to travel will take longer to exit the fibre. This phenomenon manifests itself as a spreading of the pulse of light as it moves down the fibre. Broader pulse widths limit the bandwidth of the fibre. The spreading is proportional to the length of the fibre used.

The pulse spreading can be mitigated through the construction of graded-index multimode fibres. In graded-index fibres, the index of refraction of the core is no longer uniform but is a function of the radial distance from the z-axis of the fibre, $n_1 = n_1(r)$. By grading the material of the core so that rays incident at steeper angles (and travelling greater distances) move at a slightly faster velocity, the overall width of the pulse remains narrow.

The larger core radius of multimode fibres increases their light-gathering capacity. Thus, less-bright and less-expensive light sources can be used with multimode fibres. Table 2.1 provides detailed specifications on most standard fibre types[1]. The general categories of fibres under consideration for use by the CMS and ATLAS collaborations at the LHC include the multimode fibres of 50/125 microns (core/cladding radii) and single mode fibres of 8-9/125 microns [6].

The optoelectronic readout system in the ATLAS detector currently operates at a bandwidth of 40 Mbits/s (with the pixel detector operating at 80 Mbits/s) and the CMS detector control system also currently operates at 80 Mbits/s. When the LHC upgrades to the SLHC, the increase in pileup events which will follow from an upgrade in luminosity will require both readout systems to operate on order of Gbits/s. Tests are underway to determine whether the current systems can cope with the demands for an increase in bandwidth [6].

A complicating factor is the role that radiation plays in the performance of the fibres. Section 3 will discuss the particular demands the SLHC will place on the optoelectronic components of the ATLAS and CMS detectors and the specific fibres

[1]http://www.lanshack.com/fiber-optic-tutorial-fiber.aspx

tested will be presented.

Table 2.1: Typical fibre types and specifications.

Core/cladding	Attenuation	Bandwidth	Applications
Multimode Graded-Index	@850/1300 nm	@850/1300 nm	
50/125 μm	3/1 dB/km	500/500 MHz-km	GbE LANs
50/125 μm	3/1 dB/km	2000/500 MHz-km	850 nm VCSELs
62.5/125 μm	3/1 dB/km	160/500 MHz-km	Most common LAN fiber
100/140 μm	3/1 dB/km	150/300 MHz-km	Obsolete
Single-mode	@1310/1550 nm		
8-9/125 μm	0.4/0.25 dB/km	100 Terahertz	Long high speed LANs

2.2 Contributions to attenuation of light in optical fibres

At the most basic level, the purpose of the work presented here was to determine the acceptable amount of attenuation in the optical fibres to be used in the SLHC. Thus, understanding the mechanisms by which the light signal may be attenuated is important. The three different processes which contribute to signal attenuation will be presented here, accompanied by specifications on which are most influential when it comes to radiation and temperature effects on fibre performance. The theory behind optical attenuation due to temperature and radiation is not fully understood and so some of the following explanations are based on our best understanding of the physical phenomena via empirical studies.

2.2.1 Radiative loss

Radiative losses are attributed to bends in the fibre geometry. The order of magnitude of these sorts of losses tends to be less than that of either scattering or absorption-induced attenuation except for very drastic bends in the fibre, and so this mechanism should not contribute to our measures of attenuation as we were able to control the experimental setup.

2.2.2 Scattering

Two forms of light scattering which contribute to attenuation can take place in optical fibres. The first form of scattering is due to imperfections in the construction of the waveguide, such as trapped air or water molecules, but the manufacturing of high-quality fibres has evolved to the point where contributions to overall attenuation from structural defects are small compared to intrinsic scattering [20].

The second form of scattering, intrinsic scattering, is related to the fibre material itself. The dominant form of light scattering in optical fibres is Rayleigh scattering, which is the elastic scattering of photons off of particles which are much smaller than the wavelength of the photons. As noted in Section 2.1, glass is a random arrangement of molecules. Because its structure is not crystalline, any extended length of glass will have variations in molecular density across it. For doped glass, the distribution and concentration of the added dopant may also vary throughout the structure. Both of these variations occur on a scale which is small compared to the wavelength of the light. Rayleigh scattering off these density variations results in energy loss from the propagating light [31]. In non-irradiated fibre, intrinsic scattering tends to be the limiting factor on fibre performance for the light wavelengths of interest to this project. However, as will be discussed, radiation complicates the picture and causes non-trivial defects in the mechanical structure of the fibre. Then, these externally-induced defects can eventually reach a sufficient concentration that their effect on attenuation meets and supercedes the attenuation due to intrinsic scattering within the fibre.

2.2.3 Absorption

This third contribution to attenuation comes from atomic absorption of the photons. Atomic absorption can occur via both intrinsic and extrinsic mechanisms. Intrinsic absorption is a function of the energy levels of the constituent molecules of the glass and so is the limiting factor on fibre performance due to absorption. For glass, intrinsic absorption occurs at both the upper and lower energy bounds of the visible light spectrum. At higher energies of light, in the UV region, the electron band gap of the atom allows absorption. Photons of the right energy ($E = h \times \nu$ where ν is the frequency of the propagating light) can be absorbed by the atomic electrons in lower energy levels so that the electrons are then excited to higher levels. Although the excited electron can then drop back down to its initial energy state, re-emitting the photon, the photons will be emitted isotropically and thus not enhance the propagating light signal. Additionally, it is often the case that the reemitted photon is of a slightly lower energy than the absorbed photon because the absorbed photon can excite rotational modes of the SiO_2 molecule itself. At lower energies of light, in the near-IR region, the bond between the Si and O atoms can absorb photons, which results in atomic vibrations (excited molecular vibrational modes). The characteristic vibration frequency of the bonds between the constituent atoms of the glass molecules can absorb photons with energies in the near-IR region [5], [31].

Extrinsic absorption effects are caused both by compositional impurities introduced in the fibre manufacturing process and by molecular defects and density

variations of dopants and base substances in the fibre. During fibre production, metal and OH^- ions can be trapped in the glass. This creates new energy levels for electrons which can be excited by specific visible light frequencies. However, our light sources operate in the windows of low attenuation occurring between the fundamental absorption peaks of water (the low-attenuation transmission windows of optical fibres are shown in Figure 2.2[2] and range among $800 - 900$ nm, around 1300 nm, and around 1500 nm) and hence generic extrinsic absorption effects do not play a significant role in our measurements.

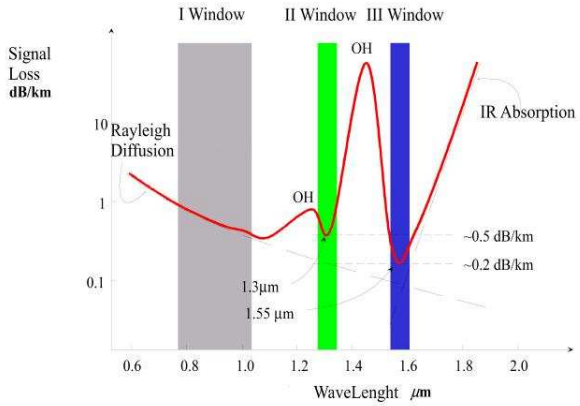

Figure 2.2: Transmission windows in optical fibres as a function of the wavelength of the propagating light.

Radiation-induced attenuation (RIA) via absorption

More relevant and interesting to this work is extrinsic absorption due to the fibre's atomic defects. Generally, these contributions to attenuation are much smaller than the contributions due to intrinsic absorption and scattering, but the introduc-

[2]http://macao.communications.museum

tion of radiation to the system drastically complicates these effects [5]. Radiation damages the structure of fibre on the atomic level. The effect this has on attenuation will be a function of the type of radiation the fibre experiences (ionizing vs. non-ionizing), the energy of the radiated particles, the dose rate, and the total dose [12], [21]. The temperature at which the fibre operates, as well as any time during which the fibre is removed from the radiation and allowed to anneal, also affect the RIA [30], [27]. It is for these reasons that it is difficult to predict the effect of radiation on silica fibre without performing experimental tests in which the fibre is irradiated up to the total dose it is expected to receive over its lifetime [45]. However, it is possible to apply what is known about radiation effects on optical components to understand the phenomena which are observed when the fibre is under test [17].

2.3 Radiation damage

Radiation damage comes in two forms: non-ionizing/bulk and ionization damage.

2.3.1 Bulk radiation damage

Bulk radiation damage occurs when massive particles like pions, protons, and neutrons bombard a material. The bulk, non-ionizing energy loss, occurs via atomic displacement. However, optical fibres tend to be much more sensitive to ionizing radiation than bulk radiation, and the author has only conducted experimental tests of fibre performance using gamma radiation [17]. Thus the majority of this report

will focus on ionizing effects [5].

2.3.2 Ionizing radiation damage

High energy photons interacting with matter can cause radiation damage. As the material being radiated is ionized, there can be both short-term and long-term effects. Potential short-term effects include the creation of temporary colour centres. Colour centres are regions of a normally transparent material that become damaged on the atomic level. These damaged regions are fill by electrons stripped off of atoms and molecules by the high energy radiation. These sites then absorb light, appearing coloured instead of transparent [40]. Potential long-term effects of radiation include the creation of permanent colour centres (via the same physical mechanism that produces temporary colour centres) and photoluminescence, whereby the molecules of the fibre absorb photons and then re-emit them a short time later [46].

2.3.3 Annealing

As will be elucidated in Section 5, experimental results indicate that there are forms of radiation damage which can be annealed (allayed) by either temperature changes or photo-bleaching, or a combination of both, depending on the species of fibre being radiated and the amount of radiation damage suffered [12].

Temperature-induced annealing

Although radiation-induced attenuation occurs because the molecular structure of the fibre becomes damaged, creating new energy levels which increase pho-

ton absorption, results presented in Section 4 and Section 5 indicate that partial annealing of these damages can occur when the temperature at which the system is operating is temporarily increased. The warmer temperature allows the molecules of the fibre to diffuse, thus mitigating the damage done by the radiation [39].

Photo-bleaching induced annealing

Much of the RIA occurs via photon absorption by electrons trapped in new molecular sites caused by the radiation damaging the molecular structure of the glass fibre. When the fibre is temporarily removed from the radiation, the light being transmitted through the fibre can have enough energy to knock these trapped electrons out of their sites which has the effect of decreasing the light attenuation [5]. However, unlike the temperature annealing, this recovery is only temporary and upon returning the fibre into the radiation, the still-existing trap sites become re-filled by electrons, thus returning the attenuation back to its previous, higher level. Evidence for these effects will be described in greater detail in Section 4 and Section 5.

Chapter 3

Experimental Setup

3.1 Basic components

The equipment being tested during measurements of fibre performance consisted of, at minimum, a light source which was coupled to the fibre under test, and a light sensor to detect and measure the light propagating through the fibre. Schematics of the specific devices and setups tested by the author will be presented in Section 4.

Optical fibre comes in two basic varieties, single mode and multimode. As the ATLAS collaboration has yet to make a final decision on choice of fibre type for the upgrade, tests of fibre performance were conducted on both single mode and multimode fibre types. In general, for optical systems, the light source used is a laser diode as they have short response times (< 1 ns), a narrow pulse, and can couple suitably bright light into optical fibres, even those with narrow cores. The light-detection device used to detect the light output is a photodiode. The use of

photodiodes allows a direct readout of the voltage measurement corresponding to the amplitude of the propagating light [48].

3.1.1 Single mode fibres

The composition and structural properties of the fibre determine which modes of light will propagate (see Section 2.1 for theory of light propagation and a more detailed explanation of fibre types). Single mode (SM) fibres have a very narrow core which supports only a single propagation mode. This results in a large bandwidth but lower light-gathering capacity for SM fibres.

The light source used in these tests was an edge emitting laser diode (EEL) operating at 1310 nm wavelength light [31].

3.1.2 Multimode fibres

Multimode (MM) fibres have a larger core radius allowing the support of multiple propagation modes. The larger radius means that MM fibres are easier to align with light sources, but modal dispersion of the light limits the bandwidth of the MM fibre. The larger core of the MM fibre allowed the use of vertical cavity surface emitting lasers (VCSELs) operating at 850 nm wavelength light [31].

The tests presented here address the performance of graded-index, multimode fibres only.

3.1.3 Versatile Link Common Project

As described in Sections 1 and 2, the LHC upgrade will place unprecedented demands on the performance of the optoelectronic readout system of the inner detectors of the ATLAS and CMS detectors. To address these common concerns and challenges, the Versatile Link Common Project [48] was formed as a collaborative effort between the ATLAS and CMS collaborations and CERN. The purpose of this collaboration is to design, test, and identify optoelectronic system components capable of operating at high speeds (10 gigabits/second) in high radiation environments and over a distance of at least 100 m, which is the nominal path-length fibres must traverse from the inner detectors to the processing rooms.

3.1.4 Additional components used

Connectors

Fibre connectors are used to join two fibre end-faces together with minimal coupling loss of light. The vast majority of optoelectronic systems require connecting components together, and the SLHC is no exception. Basic requirements of connectors include minimal loss of power at the connection point and stable performance under changing environmental conditions. A variety of commercially available connectors exist to account for different joint shapes and different fibre types. Small gaps between the coupled fibre end-faces inside of the coupler could allow interference from reflection inside of the cavity to develop in some of the propagating modes of light. This might have the effect of changing the total power propagated

throughout the entire system, and the optical power output could very sensitively depend on the size of the gap in the aperture. Thus, temperature dependence of the connector performance was a concern and extensive tests were run on the various connectors. Section 4.2 describes and presents the results from this series of tests.

Couplers/Splitters

Optical couplers are passive devices which serve to split an incoming light stream into multiple outgoing light streams. In these tests, 1x4 couplers for both single mode and multimode systems were used and tested under temperature variation. The coupler may not evenly split the incoming light among the four outgoing channels, but ideally, at the least the splitting ratio among the channels should remain constant.

In the multimode, fused-tapered couplers, the optical power splitting process occurs inside of the coupler via evanescent power coupling. "Evanescent" refers to the exponentially decaying, transverse modes of the incoming light. Inside of the coupler, the fibres are twisted together, melted, and tapered. This allows the evanescent waves to tunnel across the barrier of the incoming fibre and leak into the coupled fibres. This transverse mode then gives rise to propagating light in the adjacent fibres [35].

In the single-mode PLC couplers, the incoming light is split and guided along etched pathways in a silica planar waveguide. Planar lightwave circuits (PLC) are constructed in a multistep process. The base layer of the device is built via flame hydrolysis deposition whereby fine particles of glass are created in an oxyhydrogen

flame and deposited onto the host substrate. Reactive ion etching is used to draw the desired circuit pattern (e.g. a 1x4 splitter) [24], [36], [44], [25].

In our studies, the optical couplers behaved in unexpected ways under changing environmental conditions. The performance of both single mode and multimode couplers depended sensitively on changes in temperature, as will be described in Section 4.2.

3.2 Experimental apparatuses

3.2.1 Mode scramblers

Previous tests of optoelectronic system stability had resulted in an unexplained effect [10]. Tests involving the VCSEL light sources produced results in which the power output varied by up to 1 dB about its mean value throughout a 24 hour period. The variation, however, was not constant. For shorter periods of time (several hours) the output looked as if two signals of distinctly different power were being produced simultaneously, and then one of the two levels would dominate the output for the next several hours. This effect initially was attributed to internal mode hopping of the VCSEL.

It is known that semiconductor lasers may undergo mode hopping whereby the laser discontinuously switches between wavelengths and lasers may also experience transverse mode hopping [23]. The speckle pattern produced in the transverse plane by this mode hopping can vary in time and longitudinally, and produces noise if

such variation occurs at a photo-sensitive area with non-uniform responsivity (e.g. at a connector). This effect can be produced by temperature or other mechanical variation of the laser cavity, by optical feedback, and by changes in injection current to the laser. To test this hypothesis and to potentially mitigate the effects of the mode-hopping, two mode scrambling devices were tested.

Micrometre-style mode scrambler



Figure 3.1: A picture of the FM-1 Mode Scrambler.

This device from Newport Photonics and Instrumentation (Figure 3.1), the FM-1 Mode Scrambler, induces mode coupling among the light modes propagating in the fibre under test. It does this by pressing the bare fibre between two parallel plates made of an interlocking sawtooth-like fabrication. As the fibre passes among these teeth, it is forced into a series of microbends. This process has two desired results. The first is that it forces higher-order guided modes to couple to non-guided modes, an effect known as mode filtering. In multimode fibres, the intensity of the

light is more stable when the power is primarily distributed among the lower order modes. Mode filtering dissipates the power from the higher order modes so that only the more stable lower order modes remain. The second effect of the microbending is that lower-order modes couple to each other (known as mode scrambling or mode mixing), with a net result of a much more even distribution of power among the lower order modes [19].

These two processes then result in an approximately even distribution of power among the lower-order modes, independent of the performance of the light source.

ModCon (modal conditioner) mode scrambler

The second mode scrambling device we tested is known as the ModCon Modal Controller (Figure 3.2) and is proprietary technology of Arden Photonics Ltd. According to the documentation of Arden Photonics, the ModCon is a passive, fibre device which decouples the modal distribution of the light source from the device under test. In other words, it, too, should eliminate the observed mode hopping which was attributed to the lasers.

3.2.2 Temperature-controlled environments

Environmental chamber

A temperature and climatic test system from Design Environmental was used to provide external control of temperature and humidity. The environmental chamber (see Figure 3.3) is capable of varying the temperature inside of the test space



Figure 3.2: A picture of the Arden Photonics Modal Controller.

between −40 °C and 180 °C, as well as varying the humidity between 0% and 100%. A LabVIEW^{TM} program was written which was capable of controlling the environmental chamber and cycling the contents of the test space through a range of temperatures and humidities.



Figure 3.3: Design Environmental Model A3721-Alpha 335-40H.

Cooler vessel

This is a very brief introduction to the motivation and design of a cooler vessel and the topic will be expanded upon in Sections 5.1, 5.2, and 5.3. Maintaining a suitably cold yet radiation-hard environment in which the fibres could be contained while being radiated was a complicated task. A first design was used initially and then improvements and modifications were made which resulted in an even more efficient cooler vessel. Both iterations of the design consisted of a cylindrical metal container in which spools of fibre fit snugly. Four Peltier coolers were placed around the internal walls of the metal vessel, and these coolers were attached to copper fins which jutted out of the vessel. The purpose of these fins was to enhance the ability of the Peltier coolers to transfer heat from the internal environment containing the fibres under test to the outside environment consisting of a large tank of shielding water, in which was submerged the radioactive source and the cooler vessel.

Chapter 4

Results of laboratory tests

4.1 Instabilities in the multimode system

Tests run during the summer of 2008 in Oxford, and reproduced by the author, showed a surprisingly poor level of stability in the multimode system [4], [10]. Before the system was taken to the SCK-CEN facility in Belgium to be irradiated (see Section 5.1), tests of the system stability were run. A schematic of the test setup is shown in Figure 4.1. The coupler was used to split the light from a single VCSEL into 4 channels. Three of the channels would be used to feed light into the devices under test (e.g., mode scramblers) while the fourth channel would be kept as reference, thus allowing the elimination of power variation due to VCSEL instability, which was assumed to be the most likely source of noise in the system.

Photodiodes are used to detect the light from the fibre. These photodiodes are reverse biased and in series with a 3.3 kΩ precision resistor, which has a 0.1 % tolerance. The resistor has one end connected to the ground and the other to the

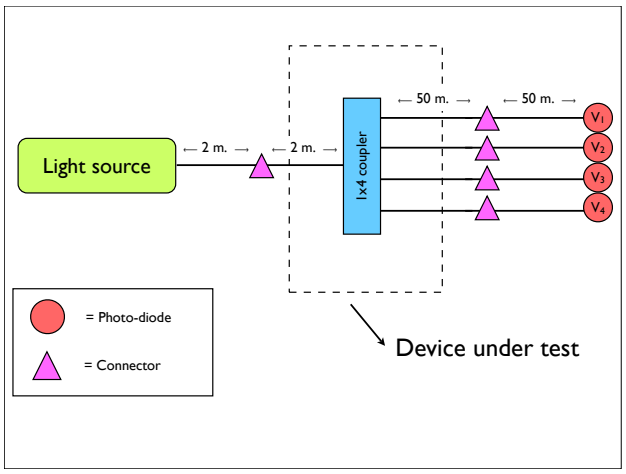

Figure 4.1: A schematic of the experimental setup.

photodiode. Current flows through the photodiode when light is incident upon it, and this current produces a voltage across the resistor. The photodiodes produce 0.5 amps/watt of light power.

The voltage across the resistor is sensed by an integrating amplifier that has a range from 2.1 V to -2.1 V, and the integration time is digitally set through the VME (virtual machine environment) interface. The voltage is digitised with a 12-bit analog-to-digital converter where the 12-bit word (read out as a 16-bit word across the VME backplane) is proportional to the output voltage of the amplifier [26].

Surprising results were obtained from this experimental set-up. Figure 4.2 shows representative voltage outputs from the four splitter channels produced by this setup. The voltage outputs are a measure of the optical power emerging from the given channel. For comparison, Figure 4.3 shows voltage outputs from an experimental set-up in which the splitter has been removed so that the light source is

directly coupled to the photodiodes by the optical fibre. Set-ups with one and two additional connectors were both tested to determine whether the connectors played a significant role in creating background noise. Figure 4.4 is the corresponding schematic of this simpler experimental set-up.

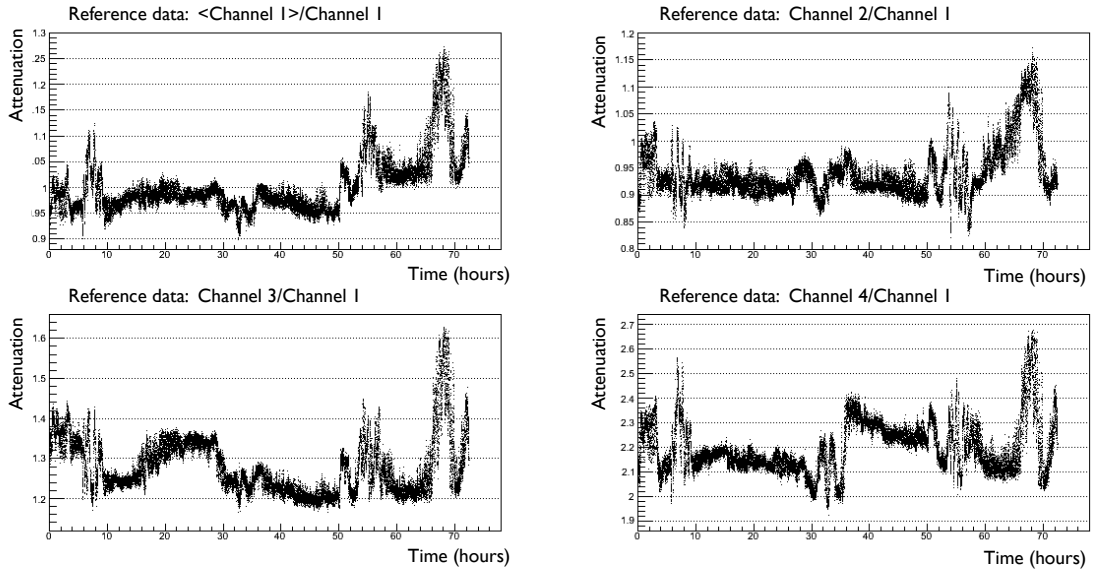

Figure 4.2: Raw data for all four channels of the splitter.

For ease of comparison among data collection runs in this section, the quantitative measure of stability of a given channel will be the RMS of the corresponding histogram. The opto-electronics working group uses a decibel calculation to measure power variation following the calculations given in Equations 4.4 and 4.5. Conse-

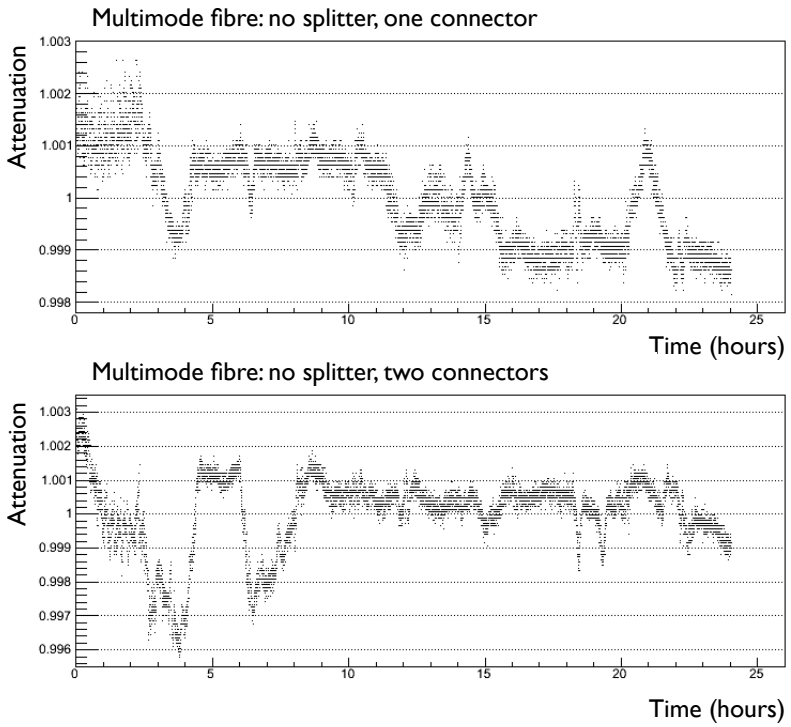

Figure 4.3: Raw data for system without splitter.

quently, the usual measure of system stability is the RMS of the histogrammed data from the decibel calculations. However, in this section, the power variation will be measured directly, using Equations 4.1 and 4.2.

Equation 4.1 gives the variation of Channel i normalised to the power measured by the reference channel. Equation 4.2 gives the variation of Channel i normalised to its average value over the entire course of the run. G_i is used to indicate the variation of one of the test channels relative to the reference channel, and G_j is used to indicate the variation of the reference channel about its own average value. V_i is

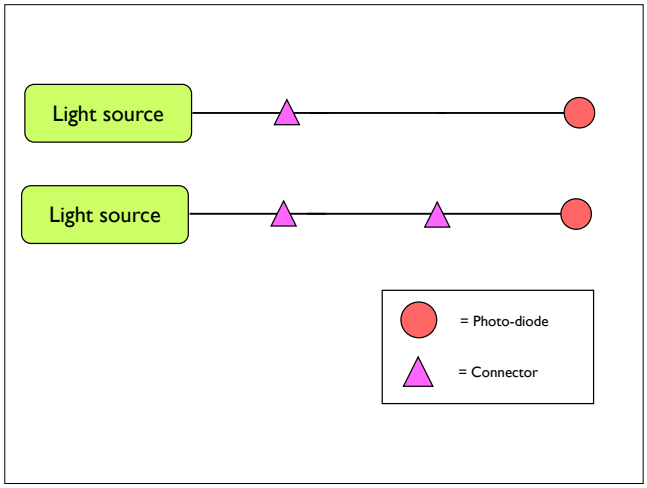

Figure 4.4: Schematic of connector experimental setup.

the voltage of channel i, P_i is the pedestal value of channel i, V_{ref} is the voltage of the reference channel, P_{ref} is the pedestal value of the reference channel and $\overline{V_i - P_i}$ is the expectation value of the corrected signal of channel i.

The pedestal values were determined for each run of data collection by taking 5 minutes of dark data (with the light sources off) before and after each run. This dark data was then averaged to produce a pedestal value.

$$G_i = \frac{\mathrm{V_i} - \mathrm{P_i}}{\mathrm{V_{ref}} - \mathrm{P_{ref}}} \tag{4.1}$$

$$G_j = \frac{\mathrm{V_i} - \mathrm{P_i}}{\overline{\mathrm{V_i} - \mathrm{P_i}}} \tag{4.2}$$

To measure the overall stability, the RMS produced by histogramming G_i or G_j is used. The decision to use the RMS of G_i or G_j in this section rather than the RMS of F_i or F_j calculated in Equations 4.4 and 4.5 was made because linear

correlations within the channels required a correction to be made to the data. The linear correction will be described in Section 4.1.1. This linear correction inside the argument of the logarithm calculation changed the behavior of the function and made it difficult to make comparisons among the different experimental set-ups. Consequently, for comparison's sake, the RMS of G_i or G_j will be used until overall behavior is established at which point this text will use the RMS of F_i or F_j. The transition from Equations 4.1 and 4.2 to Equations 4.4 and 4.5 will be indicated in Section 4.1.5.

The histograms of the data presented in Figures 4.2 and 4.3 are are given below, in Figures 4.5 and 4.6. The RMS values of these and other relevant experimental set-ups will be collected in Table 4.1.

4.1.1 Linear correlations in the data

As explained previously, the splitter was included in the experimental set-up because it was believed that laser instability would introduce the greatest variation into the system and so if it could be controlled for, overall system stability would be improved. A comparison of the RMS values of the data coming from the splitter channels with RMS values coming from the system without a splitter indicates that the goal of overall increased system stability was not achieved.

However scatter plots comparing Channels 2, 3, and 4 respectively to Channel 1 (the reference channel) indicate that there is some positive correlation within each pair, presumably a result of the shared light source varying identically in each

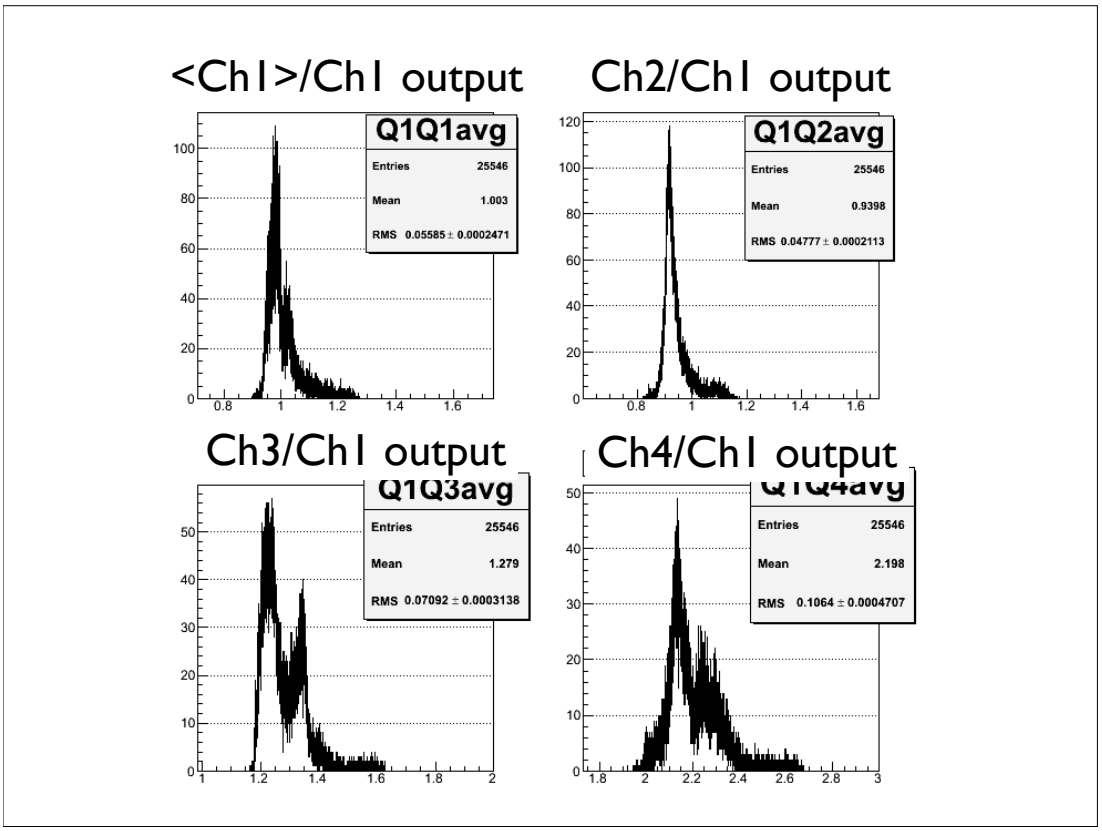

Figure 4.5: Histogram of raw data for all four channels of the splitter; G_i and G_j. RMS values for Ch. 1: 0.05585, Ch. 2: 0.04777, Ch. 3: 0.07092, and Ch. 4: 0.1064.

channel. The scatter plots, with best fit lines, are shown in Figure 4.7.

Additionally, Pearson's correlation coefficient r was calculated for each scatter plot and the r^2 value of each pair is included in Table 4.2.

To remove this shared noise source from the data, Equation 4.1 was modified to calculate the variation of each channel about the best fit line, giving Equation 4.3:

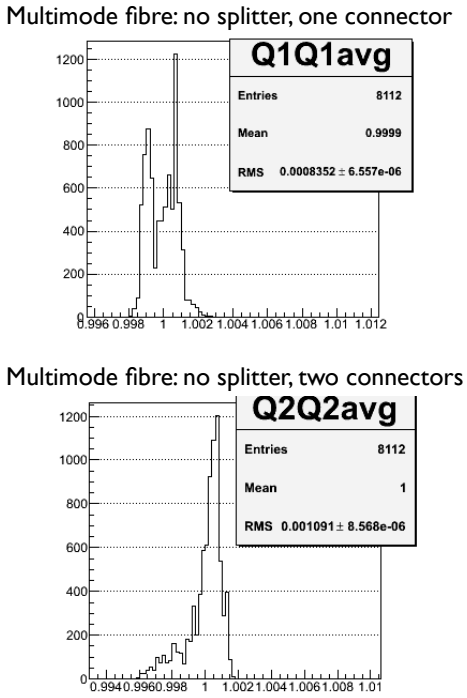

Figure 4.6: Histogram of raw data for system without splitter; calculated using G_j. RMS values for one connector: 0.0008352 and two connectors: 0.001091.

$$G_i' = \frac{\mathrm{V_i} - \mathrm{P_i} - (b + m \times (\mathrm{V_{ref}} - \mathrm{P_{ref}}))}{\mathrm{V_{ref}} - \mathrm{P_{ref}}} \tag{4.3}$$

where b and m are the y-intercept and slope, respectively, of the best-fit line to the data shown in the scatter plots.

Figures 4.8 and 4.9 display the results of this correction. As the RMS value of the corrected data indicates, correcting for this linear correlation does provide some improvement to system stability but does not approach the level of stability

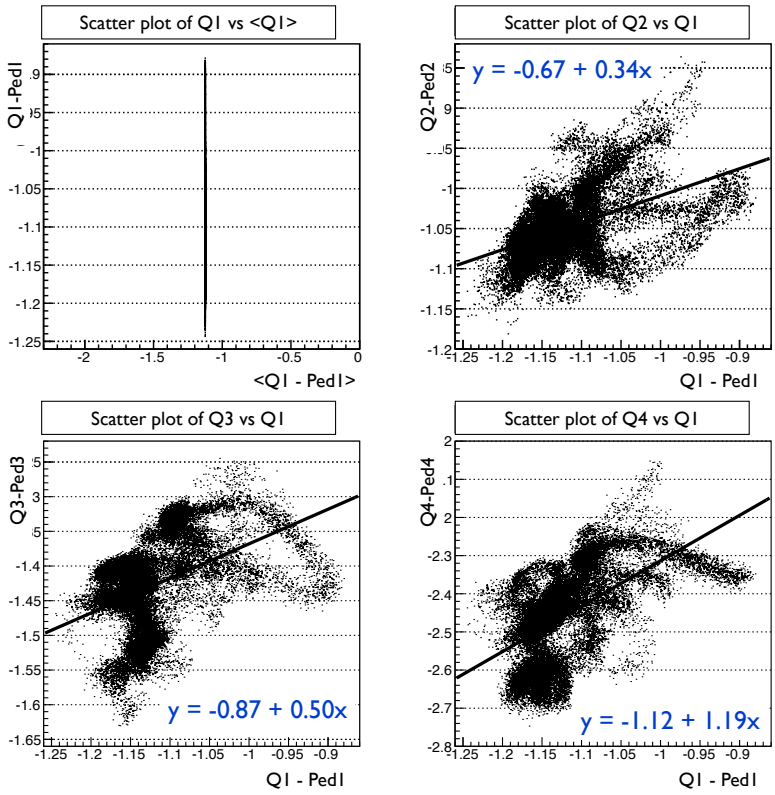

Figure 4.7: Scatter plots of splitter channels using reference.

produced by an experimental set-up without the use of the splitter. We investigate why in the next section.

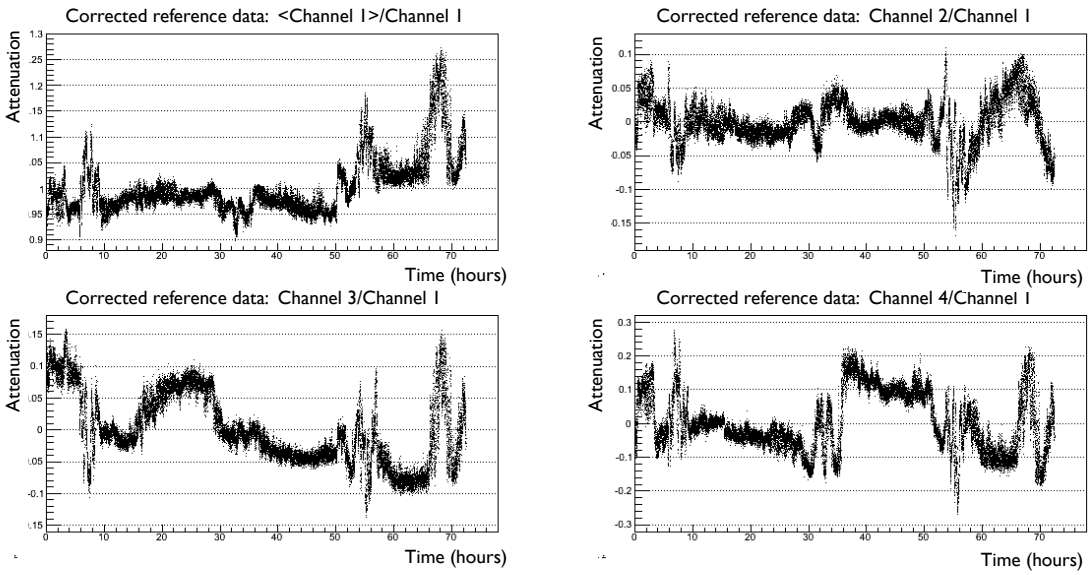

Figure 4.8: Corrected data for all four channels of the splitter.

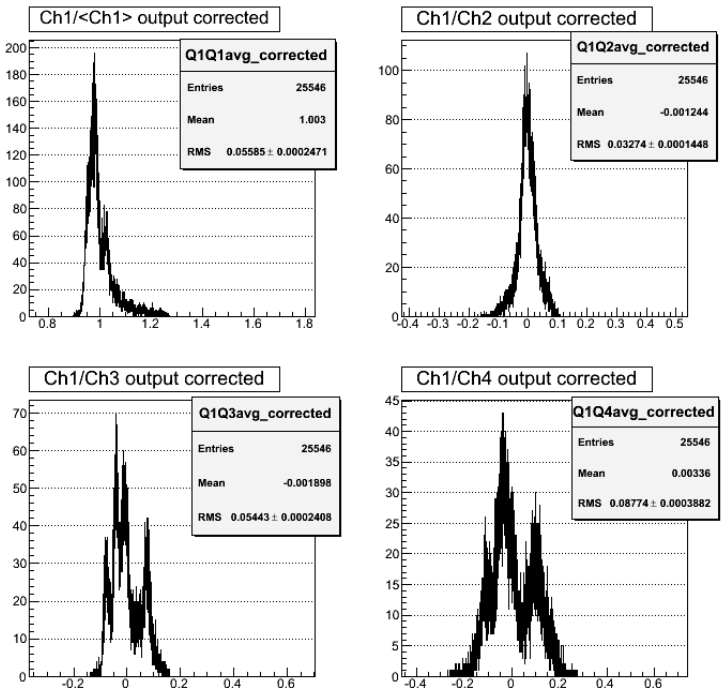

Figure 4.9: Histogram of corrected data for all four channels of the splitter; G_i'; RMS values Ch. 1: 0.05585, Ch. 2: 0.03274, Ch. 3: 0.05443, and Ch. 4: 0.08774.

4.1.2 Laser mode hopping

According to the literature, a reasonable hypothesis to explain the instability seen in the data presented in Figure 4.2 was intensity variations and mode-hopping in the laser light source [23]. Mode hopping is the effect whereby the optical power filling one mode suddenly fills a different mode. The observed effect is differing levels of light intensity, because different transverse modes have different intensity profiles due to non-isotropic material distribution in the laser [38]. Generally, in multimode lasers, the power oscillates continuously among the modes, and if mode hopping does occur, there is a gradual transition from one preferred mode to another. It is known that changes in the injection current to the laser and the temperature of a semiconductor laser can lead to mode hopping of the light output by the laser. Similarly, mechanical changes to the laser cavity and optical feedback from the fibre back into the laser can also lead to mode hopping [23]. If the cause of the instabilities is laser mode hopping, then mode scramblers should mitigate the undesired effect because mode scramblers create modal distributions with are independent of the modal distribution produced by the laser. As described in more detail in Section 3.2, mode scramblers work by coupling guided modes to each other so that power can be redistributed evenly among them, and by coupling higher-order modes to radiation modes so that those higher-order modes provide no contribution to the final measured intensity of light. Theoretically, this would result in an constant distribution of power in every mode, allowing a stable operation of a coupler device. The splitting ratio of the coupler (the fraction of light guided into each channel) may

vary with the modal distribution of the light, but if the incoming modal distribution does not vary in time, then the splitting ratio should also remain constant in time.

An extensive series of tests of two types of mode scramblers were performed. Results presented below indicate that the initial hypothesis of laser mode hopping causing the instability is incorrect, or at least incomplete.

4.1.3 Mode scrambler tests

The first mode scrambling device tested was the Newport mode scrambler. Figure 4.10 is a schematic of the test set-up used in the laboratory. For a more

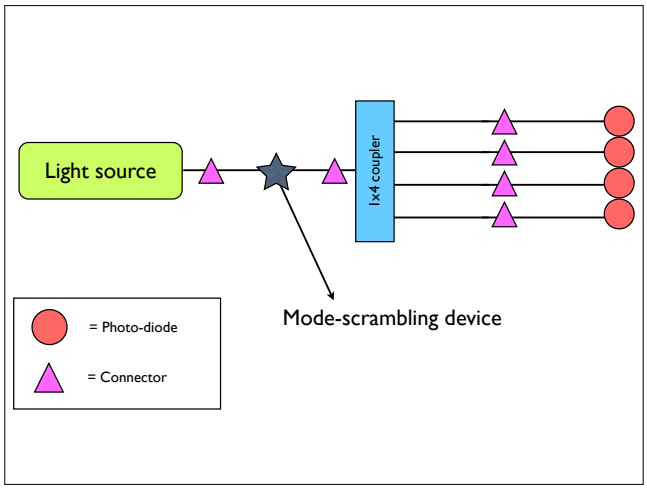

Figure 4.10: Schematic of mode-scrambling experimental setup.

detailed explanation of the function of this device, see Section 3.2. Figure 3.1 shows that the user can turn the dial (the "thumbscrew") to the desired tightness, changing the distance between the teethed plates. Data was collected in half-unit increment turns (with each half-increment corresponding to a 12.5 μm motion of the jaws), beginning with the setting at which a slight decrease in light intensity was observed and ending when close to no light made it to the end of the fibre. This covered a range of approximately 8 half-increments. Figure 4.11 and 4.12 are typical plots of the output while the mode scrambler was in use.

A comparison of the RMS variation among data with the use of the mode

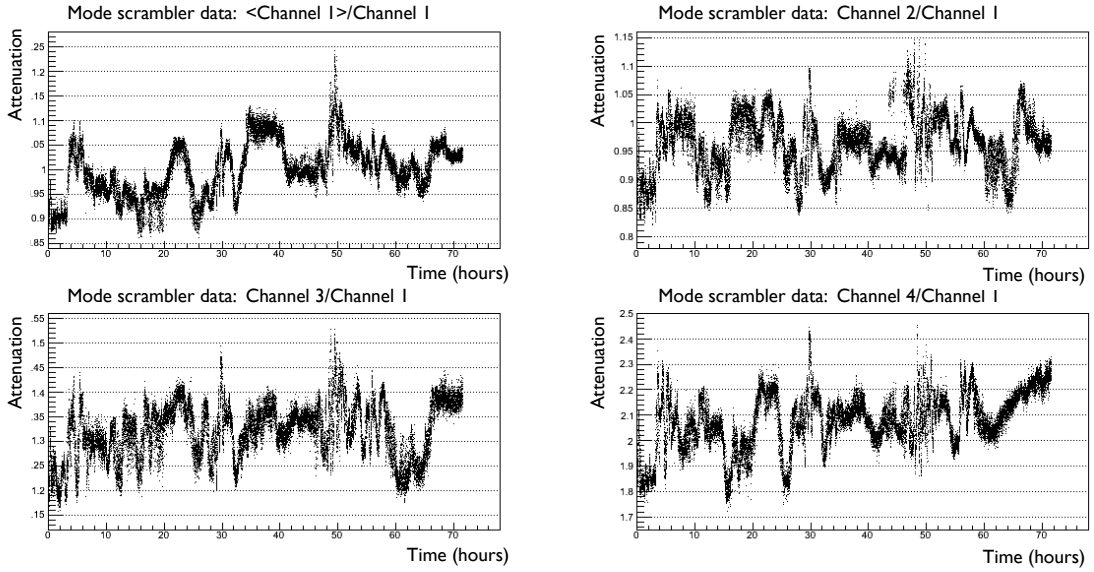

Figure 4.11: Mode scrambler: Output of splitter with the mode scrambler set to 7.0.

scrambling device and the reference data indicate that no improvement in stability is obtained. Typical RMS values of the reference data range from 0.04777 to 0.1064 and typical RMS values of the mode scrambler data range from 0.04734 to 0.1074; see Table 4.1. As in the scatter plots comparing the channels used for the reference tests, the scatter plots of the fibre outputs with use of the mode scrambling device indicate some linear correlation between channels (see Figure 4.13). Again, the data can be corrected to remove this linear correlation to determine if the instability of the system without the laser variations is more or less stable than that of the system

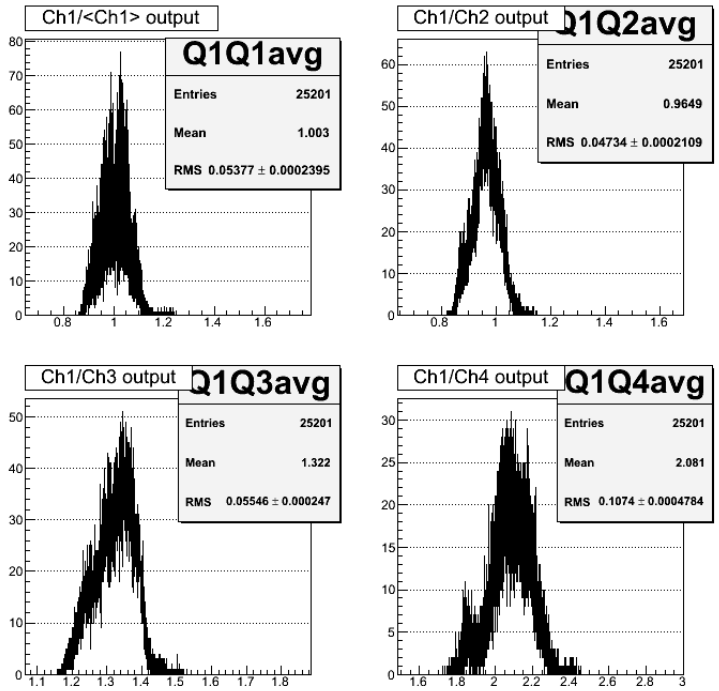

Figure 4.12: Mode scrambler: Histograms of the splitter outputs for the mode scrambling device.

without the mode scrambling device. Figures 4.14 and 4.15 show the corrected data, and the RMS variation indicates that non-laser-driven variation of the system is as unstable with the use of the mode scrambler as it was without any device. Typical RMS values of the corrected reference data range from 0.03274 to 0.08774 and typical RMS values of the corrected mode scrambler data range from 0.04152 to 0.07906; see Table 4.1.

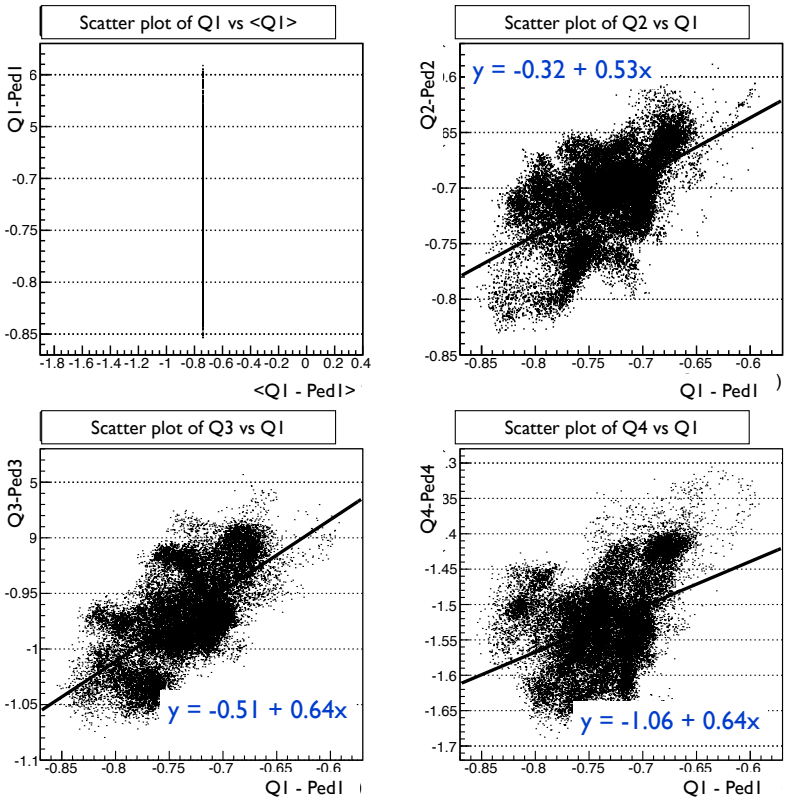

Figure 4.13: Mode scrambler: Scatter plots of the data with linear correlation indicated.

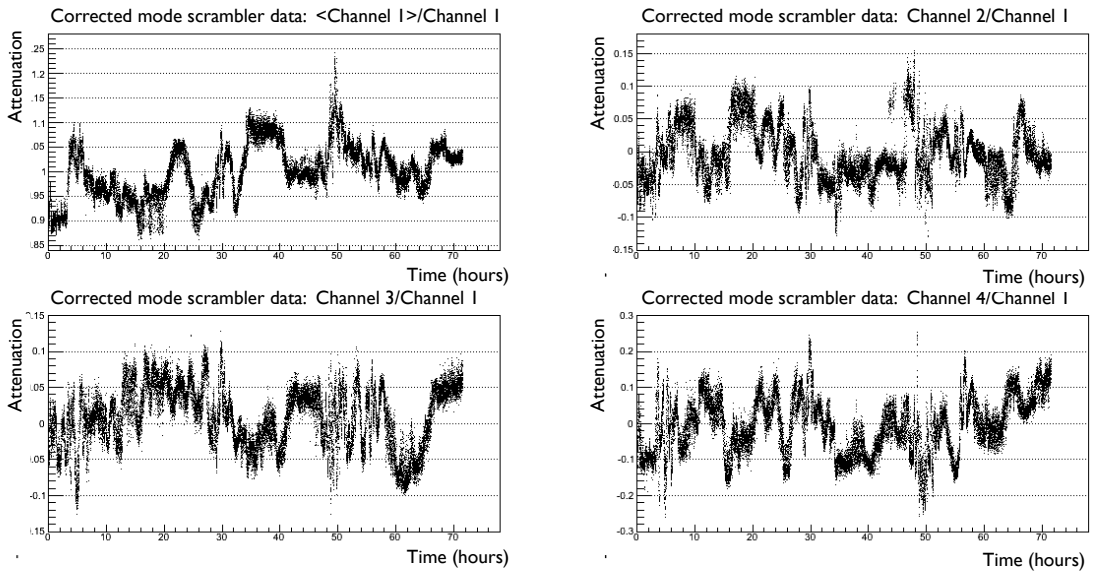

Figure 4.14: Mode scrambler: Corrected output of splitter.

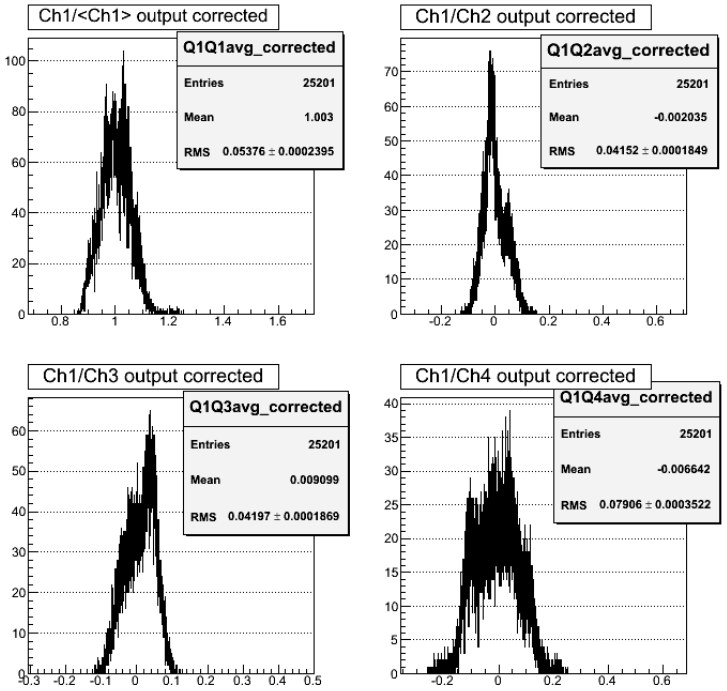

Figure 4.15: Mode scrambler: Corrected histograms of the splitter outputs .

4.1.4 ModCon tests

The second mode scrambling device used was the ModCon from Arden Photonics. While the mechanism by which it scrambles modes was enclosed in a black box and is proprietary technology of the firm, documentation indicates that it also employs a passive mode scrambling and mode filtering processes to stabilize the measured output of light from a laser. The ModCon (Figure 3.2) was inserted into the system by connecting the light source to the 'Input' side and connecting the fibre under test to the 'Output' side. The same test setup (Figure 4.10) was used. Again, results indicated no improvement in system stability, as seen in Figures 4.16 and 4.17, where RMS values are similar to data taken without the use of a mode scrambling device. Typical RMS values of the reference data range from 0.04777 to 0.1064 and typical RMS values of the ModCon data range from 0.04283 to 0.1287; see Table 4.1. Figure 4.18 are the scatter plots comparing the output channels, and as in previous tests, these plots indicate some linear correlation between the channels. The correlation is used to correct the data and remove the laser variation from calculations of system stability. Figures 4.19 and 4.20 show the corrected data, and the RMS values indicate that laser-excluded system with the ModCon is as unstable as the reference (without mode scramber) system. Typical RMS values of the corrected reference data range from 0.03274 to 0.08774 and typical RMS values of the corrected ModCon data range from 0.0334 to 0.09587; see Table 4.1.

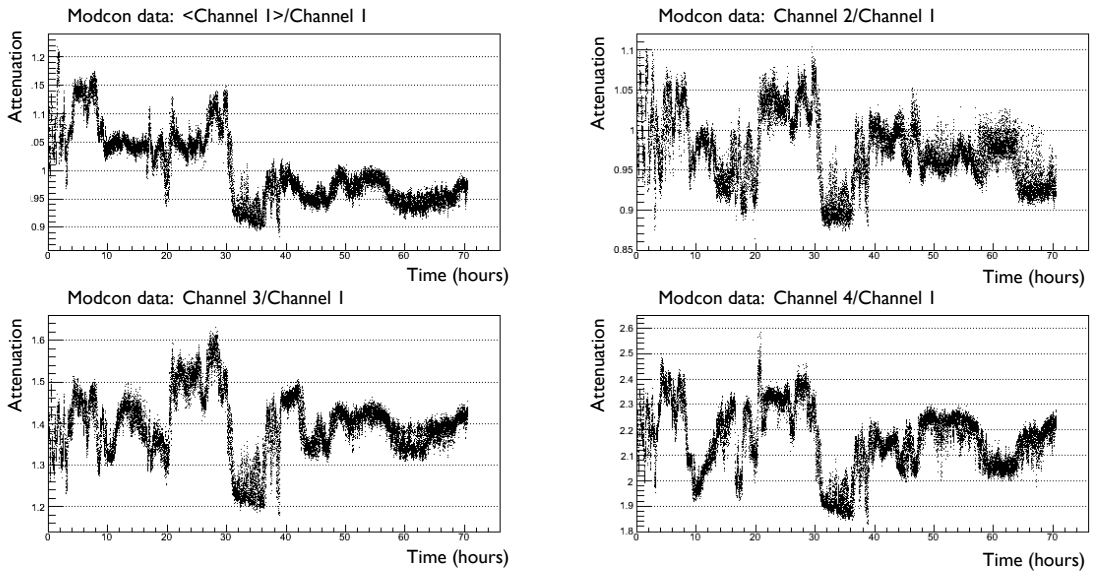

Figure 4.16: ModCon: Outputs from the splitter for the ModCon device.

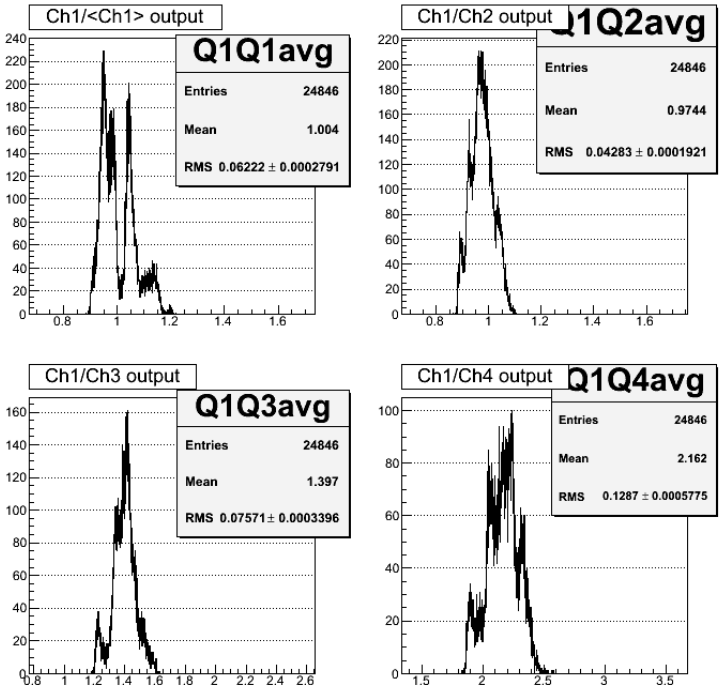

Figure 4.17: ModCon: Histograms of the splitter outputs for the ModCon device.

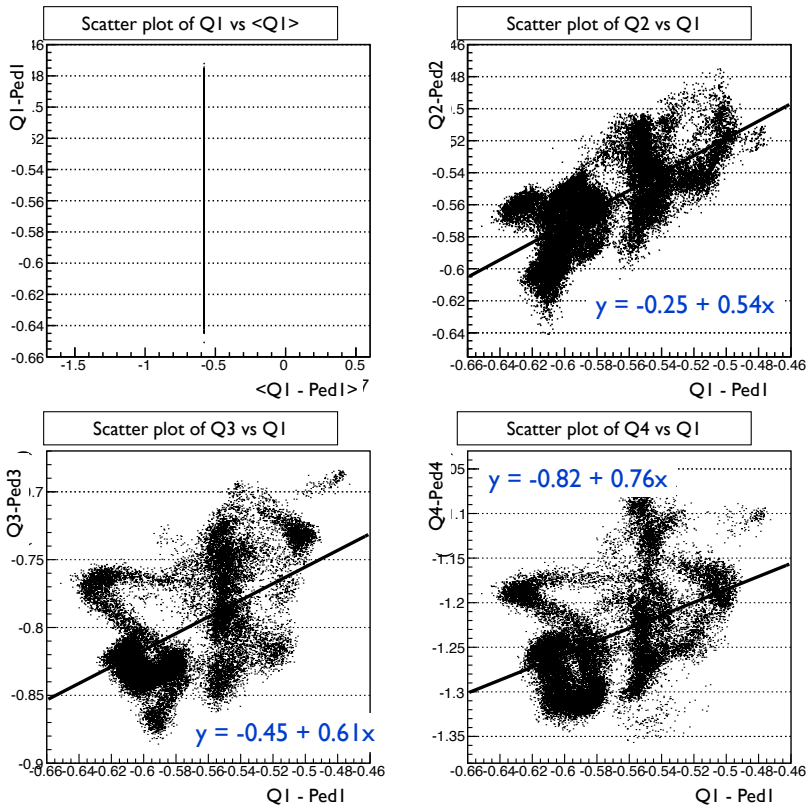

Figure 4.18: ModCon: Scatter plots comparing the output of the channels, with linear fit.

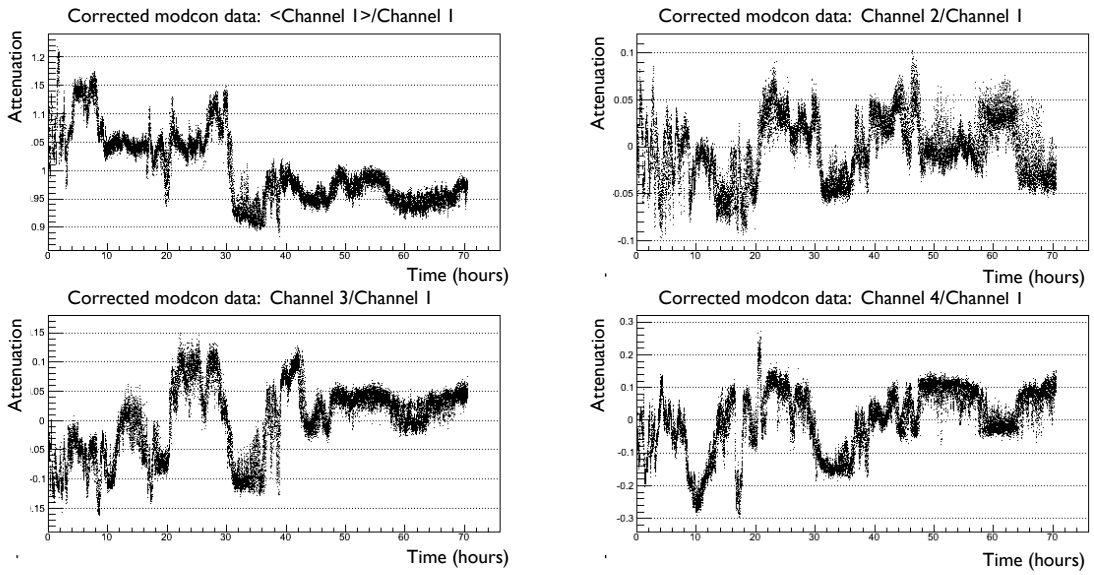

Figure 4.19: ModCon: Splitter outputs corrected for laser instability.

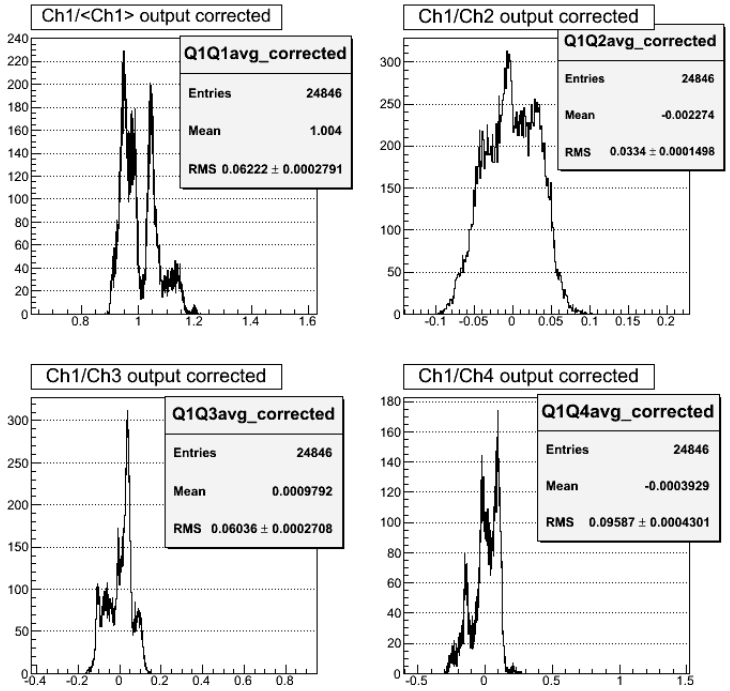

Figure 4.20: ModCon: Corrected histograms of the splitter outputs.

4.1.5 Uncorrected and corrected data

Table 4.1 will present all RMS values of uncorrected and corrected data. Table 4.2 will present the Pearson r^2 values for each scatter plot. This number provides some indication of the goodness of fit of a line to the data by quantifying what proportion of the variation in the data is accounted for by the correlation [42].

Table 4.1: RMS values for uncorrected and corrected data.

Set-up and device used	Uncorrected or corrected	Channels	Mean	RMS
No splitter	1 connector		1	0.0008352
No splitter	2 connectors		1	0.001091
Reference	Uncorrected	<1>:1	1	0.05585
Reference	Uncorrected	2:1	0.9398	0.04777
Reference	Uncorrected	3:1	1.279	0.07092
Reference	Uncorrected	4:1	2.198	0.1064
Reference	Corrected	<1>:1	1	0.05585
Reference	Corrected	2:1	0	0.03274
Reference	Corrected	3:1	0	0.05443
Reference	Corrected	4:1	0	0.08774
Mode scrambler	Uncorrected	<1>:1	1	0.05377
Mode scrambler	Uncorrected	2:1	0.9649	0.04734
Mode scrambler	Uncorrected	3:1	1.322	0.05546
Mode scrambler	Uncorrected	4:1	2.081	0.1074
Mode scrambler	Corrected	<1>:1	1	0.05376
Mode scrambler	Corrected	2:1	0	0.04152
Mode scrambler	Corrected	3:1	0	0.04197
Mode scrambler	Corrected	4:1	0	0.07906
ModCon	Uncorrected	<1>:1	1	0.06222
ModCon	Uncorrected	2:1	0.9744	0.04283
ModCon	Uncorrected	3:1	1.397	0.07571
ModCon	Uncorrected	4:1	2.162	0.1287
ModCon	Corrected	<1>:1	1	0.06222
ModCon	Corrected	2:1	0	0.0334
ModCon	Corrected	3:1	0	0.06036
ModCon	Corrected	4:1	0	0.09587

Table 4.2: Pearson r^2 values for correlations among channels.

Device used	Channels compared	r^2 value
Reference	Ch. 1 and Ch. 2	0.223573
Reference	Ch. 1 and Ch. 3	0.179745
Reference	Ch. 1 and Ch. 4	0.322983
Mode scrambler	Ch. 1 and Ch. 2	0.298552
Mode scrambler	Ch. 1 and Ch. 3	0.402939
Mode scrambler	Ch. 1 and Ch. 4	0.143466
ModCon	Ch. 1 and Ch. 2	0.481365
ModCon	Ch. 1 and Ch. 3	0.282534
ModCon	Ch. 1 and Ch. 4	0.178297

The data presented in Tables 4.1 and 4.2 indicate that some of the variation seen in the power output is due to variation in the laser light source (e.g., an r^2 value ≈ 0.3 can be interpreted as indicating that 30% of the variation is accounted for by the linear fit, which in this example corresponds to light source variation). However, a comparison of RMS values for corrected and uncorrected data within each set-up indicates that accounting for this shared variation does not improve system stability to the level achieved without the use of any device.

To allow for comparison with data presented in the rest of this chapter, Table 4.8 contains the RMS values for all previously presented data following the standard calculation of power output, given in Equations 4.4 and 4.5:

$$F_i = -10 \times \log_{10} \frac{\mathrm{V_i} - \mathrm{P_i}}{\mathrm{V_{ref}} - \mathrm{P_{ref}}} \tag{4.4}$$

$$F_j = -10 \times \log_{10} \frac{\mathrm{V_i} - \mathrm{P_i}}{\overline{\mathrm{V_i} - \mathrm{P_i}}}. \tag{4.5}$$

Equation 4.4 gives the variation in decibels of the light signal about a reference channel and Equation 4.5 gives the variation in decibels of the light signal about its own mean value. F_i is used to indicate the variation of one of the test channels relative to the reference channel, and F_j is used to indicate the variation of the reference channel about its own average value. V_i is the raw voltage of channel i, P_i is the pedestal value of channel i, V_{ref} is the raw voltage of the reference channel, P_{ref} is the pedestal value of the reference channel and $\overline{V_i - P_i}$ is the expectation value of the corrected signal of channel i.

The pedestal values were determined for each run of data collection by taking 5 minutes of dark data (with the light sources off) before and after each run. This dark data was then averaged to produce a pedestal value.

Additionally, to allow comparison among the mode scrambler settings, Table 4.9 provides the RMS (in dB) of the channels' variations about their means and variations relative to the reference channel, for both fibres undergoing mode scrambling and fibres without the mode scrambling device in use.

4.2 Temperature-induced instabilities

4.2.1 Previous results

One particularly surprising result of the previous Oxford experimental run in the summer of 2008 was the observed correlation between radiation-induced attenuation (RIA) and temperature [4]. Figures 4.21 and 4.22 show the RIA of SMF-28 single mode fibre at a dose rate of 22.5 kGy(Si)/hr[1] as well as the corresponding temperature of the vessel, and Figure 4.23 shows the light attenuation and temperature during the first 6 hours of a similar run with the multimode fibres. All figures come from [4].

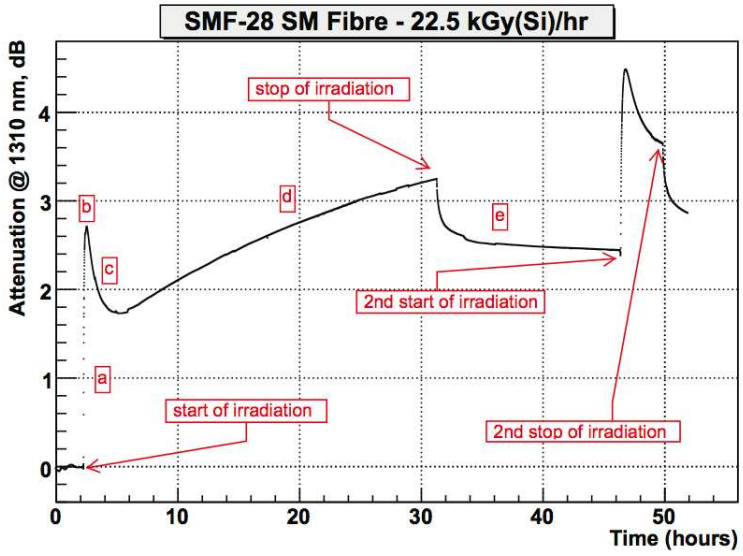

Figure 4.21: Attenuation of fibre in 2008 test: full run.

Table 4.3 will summarise the radiation and temperature in each of the regions

[1]The gray (Gy) is the SI unit of absorbed energy from ionizing radiation and 1 Gy = 1 joule per kilogram of indicated matter (e.g. Silicon).

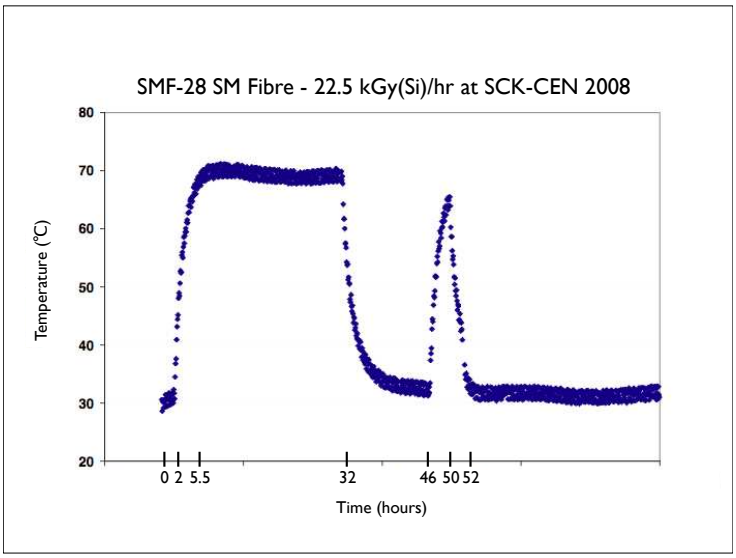

Figure 4.22: Temperature of fibre in 2008 test: full run.

of interest which are described below. In Figures 4.21 and 4.22, the temperature starts at 30 °C (approximately room temperature of the laboratory) upon immersion of the vessel into the radiation environment. The radiation source consists of cylindrical rods of ^{60}Co which produce a nearly-isotropic source of radiation [4]. Then, as it is lowered into the radiation environment, the temperature begins to increase. As the vessel is radiated, the temperature continues to increase for 5.5 hours when it then plateaus around 70 °C. The vessel continues to be radiated at a constant dose rate but the temperature remains stabilised for the remainder of the time that the vessel is in the radiation environment. Then, the vessel is removed for a period of time (approximately 12 hours) and re-immersed into the radiation environment. Upon removal, the temperature of the vessel drops to its original value of 30 °C and upon re-immersion, it repeats the rise in temperature up to 70 °C. The temperature

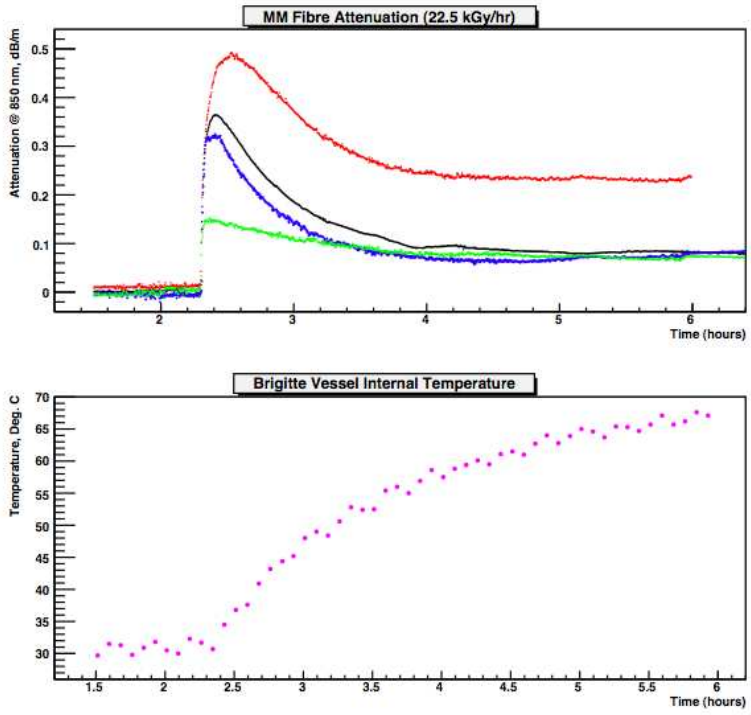

Figure 4.23: Attenuation and temperature of the four multimode fibres under test over the 1st 6 hours of interest.

variation of the vessel is caused by the thermal effects of the high-energy photons used as radiation interacting with the metal spools used to support the fibres under test [4]. The spools are made of aluminium and the gamma ray photons from the ^{60}Co source Compton scatter off of the material of the metal. The scatterings transfer energy in the form of heat to the vessel which is then manifest as a rise in temperature.

The RIA also follows an interesting trajectory. Immediately upon the immersion of the fibres into the radiation environment, the attenuation spikes to a local maximum (hour 2 in Figure 4.21.). The fibre then partially recovers and the at-

tenuation drops over the next few hours (hours 2-5.5) and finally proceeds to rise slowly and monotonically (from hour 5.5) until the vessel is removed from the radiation environment (at hour 32). While out of the radiation (hours 32-46), the fibre undergoes a limited recovery but it is a false annealing as upon re-immersion (at hour 46), the attenuation repeats the initial spike in attenuation (hour 47) and then drops back down to the level at which it would have been had it not been removed from the radiation environment (seen over hours 47-50). Thus the initial spike in attenuation upon immersion in radiation with subsequent partial recovery is a reproducible effect.

It is known that radiation-induced attenuation is dependent upon temperature [30], [39]. Previous research indicates that attenuation of light in fibre is less for warmer temperatures due to temperature-induced annealing. Section 2.3 provides an explanation of this phenomenon.

This explanation for the observed effects is supported by the observation that the apparent annealing of the fibre when it is removed from the radiation environment is a temporary effect which is completely negated immediately after the fibre is re-immersed in the radiation. This indicates that the observed monotonic attenuation is due to permanent damage to the fibre.

Table 4.3: Temperature and radiation in the regions of interest for SMF-28 at SCK-CEN, 2008.

Time range (*hours*)	*Radiation rate* ($kGy(Si)/hr$)	*Temperature behaviour* (°C)	*Radiation − induced attenuation of light*
0-2	0	constant 30	no attenuation
2	22.5	begins to rise	rises and peaks
2-5.5	22.5	continues to rise	slight recovery
5.5-32	22.5	stabilises at 70	monotonic rise
32-46	0	falls back to 30	slight recovery and stabilisation
46-47	22.5	rises again	rises and peaks
47-50	22.5	continues to rise	slight recovery
50-52	0	falls back to 30	slight recovery

4.2.2 Temperature-variant regions of the SLHC

The interplay between temperature and radiation-induced attenuation is interesting in its own right, and it is also an important component to understanding how the SLHC environment might affect the performance of the optical fibres. The fibres which make up the inner detector read-out system of the SLHC will potentially track through regions operating at a range of temperatures, from 30 °C to −25 °C [32]. As the previous radiation tests indicate, understanding the behaviour of the fibres in various radiation environments is highly dependent upon understanding their behaviour as a function of temperature, as well. Thus, a variety of tests have been performed in the process of building an understanding of the behaviour of optical fibre systems as a function of temperature and radiation.

4.2.3 Temperature-dependent behaviour of fibre systems

Ultimately, one of the goals of this project is to understand how various temperature environments affect the radiation-induced attenuation of the optical fibres to be used in the SLHC. However, before complicating the data by varying both radiation and temperature, attempts were made to understand how temperature alone might affect the performance of these optical fibre systems. By using an environmental test chamber (see Section 3.2), the author was able to cycle through a range of temperatures and measure the changes in light propagating through the systems. Tests were begun on a simple optical fibre system consisting of a light source, two fibre lengths joined by one connector, and a photo-diode, and the system under test

was gradually made more and more complex. All results are presented collectively in Tables 4.7 and 4.8.

Fibre connectors

Figure 4.4 schematically shows how we measured the effect that increasing the number of connectors in the system has on the optical power output. Increasing from one connector to two connectors has a minimal effect on the stability of the light output, as can be seen in Figures 4.24 and 4.25. Figure 4.24 has an RMS of 0.003732 dB and Figure 4.25 has an RMS of 0.004741 dB. Over time, it became clear that these RMS values are small.

The components of the singlemode system limited the number of the same type of connector it was possible to insert into the setup, but Figures 4.26 and 4.27 shows that a simple (i.e. without a coupler) singlemode system can maintain stability as well, with an RMS of 0.02286 dB.

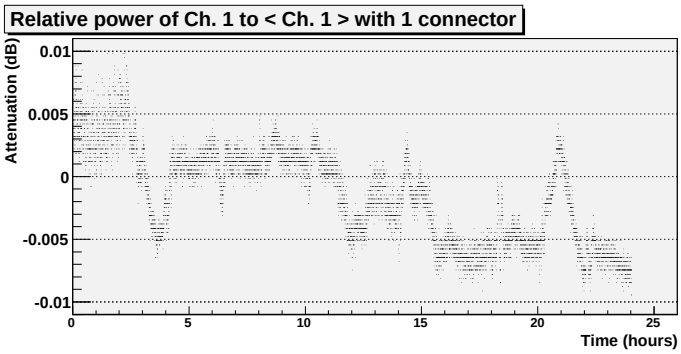

Figure 4.24: The relative power variation of one channel in multimode system with one connector.

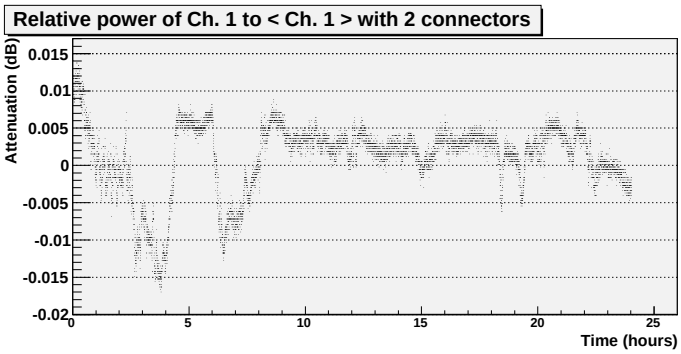

Figure 4.25: The relative power variation of one channel in multimode system with two connectors.

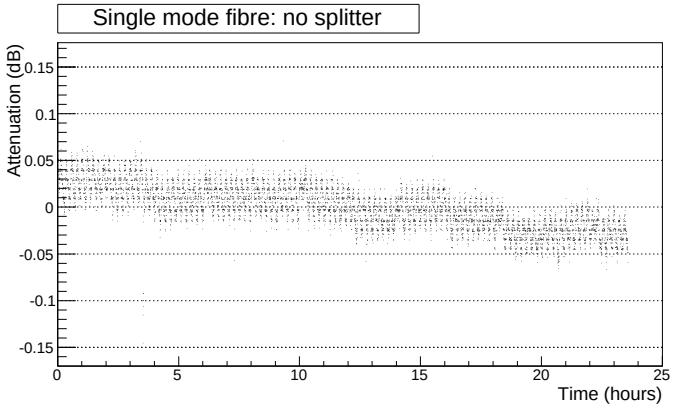

Figure 4.26: The relative power variation of one channel in singlemode system with one connector.

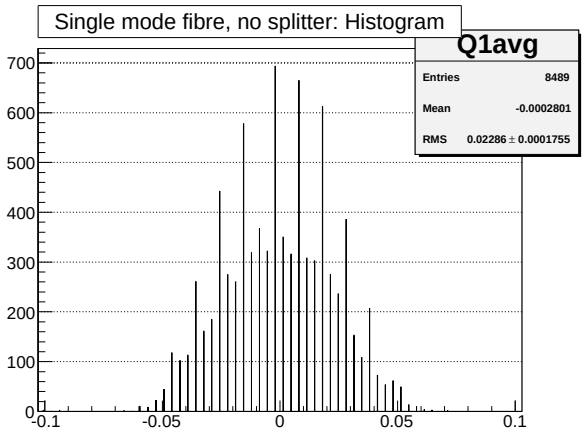

Figure 4.27: The distribution in power of a singlemode system with one connector.

Optical grease

These tests were also repeated with index-matching optical grease applied to any points of transition in the system. Optical grease is designed to couple the modal distribution of the light leaving one fibre to the surface of the connecting fibre. It does this by matching the index of the glass fibre through which the light is propagating so that the glass-air interface at points of contact of two fibre ends are removed. It also reduces the effects of non-flatness between the two faces of the coupled fbres. Thus, it was thought that should the connectors have been creating minor instabilities, the optical grease would diminish this effect. Tests with optical grease show a similar measure of stability to tests without optical grease. Data from the tests of performance with the use of optical grease are presented in Tables 4.7 and 4.8 and indicate that the RMS values for trials with and without optical grease are similar. To see that performance levels are similar, the RMS values for the optical grease tests are compared to the data shown in Table 4.5, in which each region's data was taken for a constant temperature over the period of that region.

This series of tests indicates that the connectors perform well in a variety of environments and do not contribute in a significant amount to any observed instabilities in the optical power output of the system [7], [50].

Couplers

Once it was established that the number of connectors in the system did not significantly increase the instability of the system, an optical coupler was introduced.

As described in Section 3.2, optical couplers should create a constant splitting ratio of the incoming light among the outgoing channels by stably dividing all propagating modes of light. However, interestingly, in these stability tests, the couplers under test did not provide a distribution of power among the outputs that was constant in time. This effect can be seen in Figure 4.2 where the ratio of the outputs of two of the channels varies in time. This effect was first observed in test runs without the use of the environmental chamber, but it should be noted that the room in which these tests were run was not a well-controlled environment. The ambient temperature of the room nominally remained at 23 °C but occasional observations indicated that this could vary by ± 3 °C.

To test the effect of temperature on the performance of the fibre system, an environmental chamber was used. The light sources and light detectors remained outside of the chamber while connectors and couplers were inside of the chamber. The light sources and detectors were connected to the devices in the chamber by means of fibres running from the lab bench into the environmental chamber.

Once tests were begun with the environmental test chamber cycling through a range of temperatures, an interesting relationship between temperature and optical power output was observed. Figure 4.28 is a plot of the output of one of the coupler channels and the temperature profile for this run, for both single and multimode fibre systems. The power coupling to a particular channel depends on the temperature of the environment in which it rests. Because similar tests were run with the same number of total connectors in the system but without the coupler, we can conclude that the observed instabilities of the test system are driven by the temperature-

dependent performance of the coupler itself.

It is also interesting to note that taking a ratio of two coupler outputs does not result in a significantly greater level of stability for the system (see the comparisons presented in Tables 4.7 and 4.8 – the first column gives the RMS of the variation of an individual channel about its mean and the second column gives the RMS of one channel normalised to another channel). In fact, the system without any coupler at all maintains a greater degree of stability despite original concerns over variations in the output of the light source. This indicated that future radiation tests either be conducted either without the use of couplers or with temperature-stabilised couplers so as to be able to much more accurately measure variations in optical output caused by radiation.

Figure 4.28 demonstrates that the performance of both the single-mode and multimode systems depends on temperature. To compare this temperature-dependent performance with the stability of the system when it is maintained at constant temperature, Tables 4.4, 4.5, and 4.6 calculate the average value and RMS for each of the 6 distinct time periods during which the system was maintained at a constant temperature inside of the environmental chamber. In these tests the temperature is read out by the environmental chamber. The splitter used in these tests is a 1x4 coupler, which is constructed by attaching two 1x2 couplers to each of the output channels of an initial 1x2 coupler, as shown in Figure 4.29. Because of this method of construction, the ratios of channels 4:1 and 2:1 were both included to demonstrate that we do not see increased stability in the ratio of the two channels deriving from the same channel of the initial 1x2 coupler.

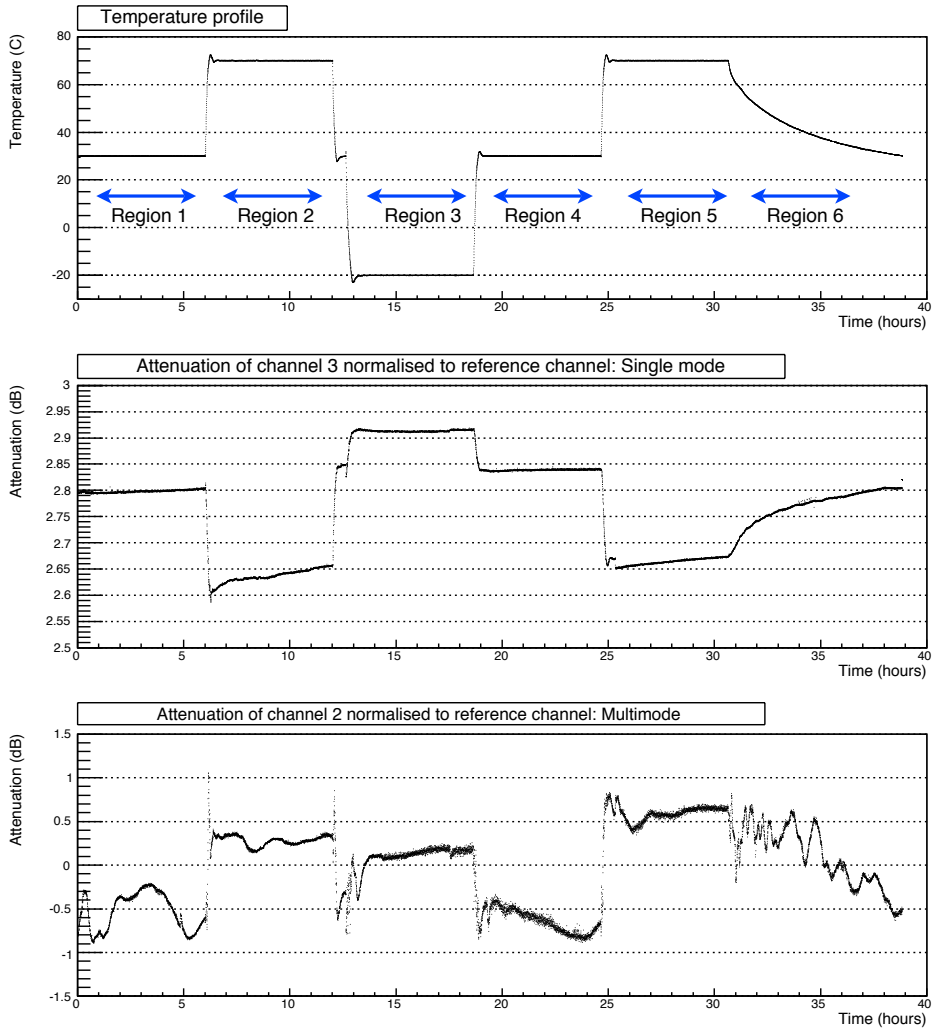

Figure 4.28: Temperature and attenuation profiles during single-mode and multimode coupler tests.

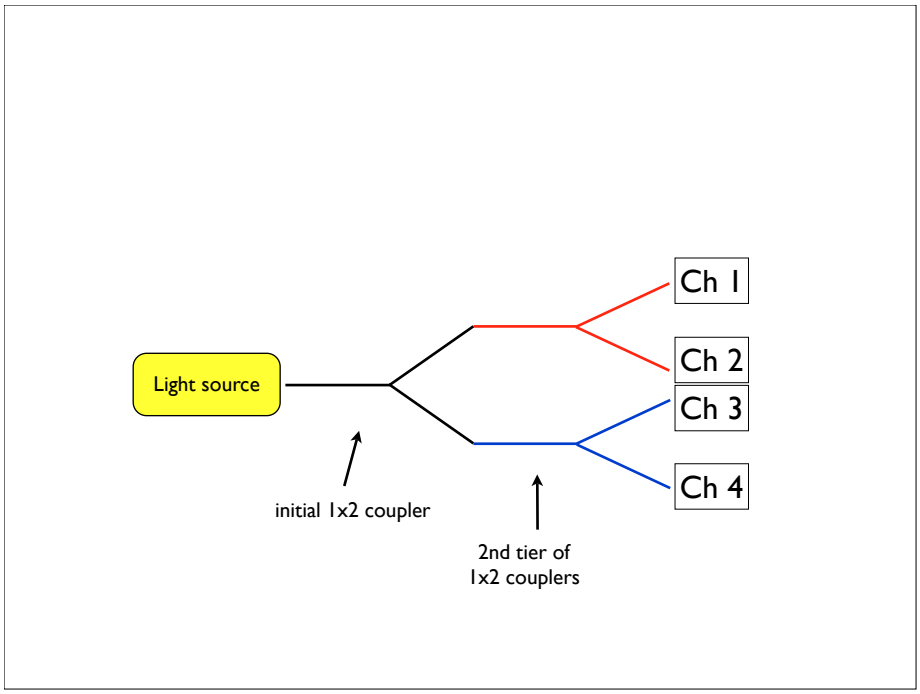

Figure 4.29: Schematic of how 1x4 couplers are constructed.

Table 4.4: Stability of the individual regions (excluding transitions): Single-mode.

	$Ch.1/\overline{Ch.1}$	$Ch.2/Ch.1$	$Ch.3/Ch.1$	$Ch.4/Ch.1$
Hours 0-6				
Region 1 mean	-0.04923	0.107	2.798	1.726
Region 1 RMS	0.01019	0.01012	0.002507	0.00224
Hours 7-12				
Region 2 mean	0.1262	0.2784	2.639	1.565
Region 2 RMS	0.004482	0.01952	0.0233	0.02442
Hours 13-18				
Region 3 mean	-0.1154	0.04007	2.912	1.828
Region 3 RMS	0.002189	0.006014	0.01004	0.01233
Hours 19-24				
Region 4 mean	-0.01618	0.1368	2.841	1.758
Region 4 RMS	0.008654	0.01716	0.009837	0.00923
Hours 25-30				
Region 5 mean	0.1491	0.3007	2.668	1.593
Region 5 RMS	0.004108	0.01969	0.02357	0.02293
Hours 31-36[2]				
Region 6 mean	-0.0643	0.0999	2.77	1.68
Region 6 RMS	0.05248	0.06336	0.03165	0.02558

[2]Not a temperature-stable region; included for completeness.

Table 4.5: Stability of the individual regions (excluding transitions): Multimode.

	$Ch.1/\overline{Ch.1}$	$Ch.2/Ch.1$	$Ch.3/Ch.1$	$Ch.4/Ch.1$
Region 1 mean	0.04362	-0.5271	-0.9039	-4.494
Region 1 RMS	0.1628	0.2122	0.2403	0.1335
Region 2 mean	0.2360	0.2689	-1.129	-3.508
Region 2 RMS	0.08895	0.145	0.1106	0.1675
Region 3 mean	0.1413	0.08206	-0.717	-3.782
Region 3 RMS	0.06583	0.153	0.08004	0.1098
Region 4 mean	-0.1820	-0.6251	-1.058	-4.817
Region 4 RMS	0.0671	0.1559	0.1154	0.2032
Region 5 mean	-0.3112	0.5777	-0.8674	-3.762
Region 5 RMS	0.08182	0.1662	0.1396	0.163
Region 6 mean^2	0.1059	0.09869	-0.8662	-3.817
Region 6 RMS	0.1256	0.3401	0.1486	0.3755

Table 4.6: Stability of the individual regions: Temperature.

	Temperature
Region 1 mean	29.99
Region 1 RMS	0.04701
Region 2 mean	70.04
Region 2 RMS	0.03989
Region 3 mean	-20.06
Region 3 RMS	0.1003
Region 4 mean	30
Region 4 RMS	4E-05
Region 5 mean	70.04
Region 5 RMS	0.06956
Region 6 mean^2	41.12
Region 6 RMS	9.339

Table 4.7: Results from connector tests, optical grease tests, and temperature variation tests for multimode fibres: RMS of the attenuation.

	RMS of dB variation of individual channel	RMS of dB variation of normalized channels
1 connector, no coupler	0.003732	n/a
2 connectors, no coupler	0.004741	n/a
optical grease, coupler, Ch. 1	0.1212	n/a
optical grease, coupler, Ch. 2	0.08558	0.1458
optical grease, coupler, Ch. 3	0.1034	n/a
optical grease, coupler, Ch. 4	0.07329	0.0192
temp. variation entire run, coupler, Ch. 1	0.2271	n/a
temp. variation entire run, coupler, Ch. 2	0.1769	0.1459
temp. variation entire run, coupler, Ch. 3	0.4459	0.3534
temp. variation entire run, coupler, Ch. 4	0.2318	0.1831

Table 4.8: Results from connector tests, mode scrambler tests, and modCon tests for multimode fibre: RMS of the attenuation.

	RMS of dB variation of individual channel	RMS of dB variation of normalized channels
1 connector, no coupler	0.003732	n/a
2 connectors, no coupler	0.004741	n/a
2 connectors, coupler, Ch. 1	0.2308	n/a
2 connectors, coupler, Ch. 2	n/a	0.212
2 connectors, coupler, Ch. 3	n/a	0.2333
2 connectors, coupler, Ch. 4	n/a	0.2059
2 connectors, mode scrambler, Ch. 1	0.2331	n/a
2 connectors, mode scrambler, Ch. 2	n/a	0.2139
2 connectors, mode scrambler, Ch. 3	n/a	0.1834
2 connectors, mode scrambler, Ch. 4	n/a	0.227
2 connectors, modCon, Ch. 1	0.2646	n/a
2 connectors, modCon, Ch. 2	n/a	0.1908
2 connectors, modCon, Ch. 3	n/a	0.2372
2 connectors, modCon, Ch. 4	n/a	0.2612

Table 4.9: RMS of the variation in output (in dB) for mode scrambler settings.

Scrambler setting	$Ch.1/\overline{Ch.1}$ (*with MS*)	$Ch.2/Ch.1$ (*with MS*)	$Ch.1/\overline{Ch.1}$ (*without MS*)	$Ch.2/Ch.1$ (*without MS*)
6.5	0.1267	0.1439	0.03524	0.05764
7.0	0.2331	0.2139	0.1079	0.07382
7.5	0.2091	0.2199	0.06762	0.07092
8.0	0.2838	0.266	0.07439	0.09362
8.5	0.3652	0.1503	0.1821	0.08473
9.0	0.3118	0.08535	0.0653	0.04051
9.5	0.5929	0.2027	0.1258	0.05894
10.0[1]	2.067	0.3379	0.07414	0.1255

[1]It is believed that the fibre was broken at the 10.0 setting of the device.

Chapter 5

Radiation tests

5.1 Motivation

While it has been established that determining the performance of optical fibres and their components operating at cold temperatures in a high radiation environment is a vital part of R&D for the SLHC upgrade, running radiation tests on fibres while maintaining a suitably cold environment ($-20\,^{\circ}\mathrm{C}$ – $-25\,^{\circ}\mathrm{C}$) is a technically challenging procedure. Very few similar tests in comparably high radiation dose environments have been conducted in the past, and thus a new method and procedure had to be developed for these tests. Two sets of tests were conducted over the summer of 2009 at the SCK-CEN radiation facility near Mol, Belgium. The preparation and results of each test will be presented below.

Experimental setup at SCK-CEN

The SCK-CEN Belgian Nuclear Research Centre is a non-academic nuclear research facility with a campus located near Mol, Belgium[1]. Of particular interest to the Oxford research group are their two ^{60}Co gamma ray radiation sources available for research and experimental work. The higher dose source is called Brigitte and provides a maximum possible dose rate of 22.5 kGy(Si)/hour. The lower dose source is called Rita and provided a maximum dose rate of 1 kGy(Si)/hour although for the results presented here, a dose rate of 0.51 kGy(Si)/hour was measured. Only the lower dose source was used for the cold tests discussed in this work because it was unclear if the Peltier coolers would survive in the low dose source, let alone in the higher radiation environment. The Rita source consists of cylindrical rods arranged in a circle, submerged in a tank where it is shielded by 8 metres of water. Any devices to be tested just be fit inside of a water-tight, slightly buoyant container which is lowered into the water tank.

Designing a vessel to hold the fibres under test that could maintain the desired cold temperature under radiation involved taking into account several convoluting factors. The coolers which were used to cool the vessel containing the fibres needed to be suitably radiation hard so as to maintain their operating capacity even after 24-48 hours of exposure in the low-dose environment. They also needed to be powerful enough to maintain the cold temperature of the vessel despite the energy being deposited in the walls of the vessel by the radiation gamma-rays Compton scattering

[1]http://www.sckcen.be/en/About-SCK-CEN

in the metal.

The chosen vessel design is shown in Figure 5.1. Upgrades and improvements carried out in the second run will be discussed later. The vessel's exterior walls were constructed of Aluminium and four Peltier coolers were affixed at equal spacing around the internal circumference.

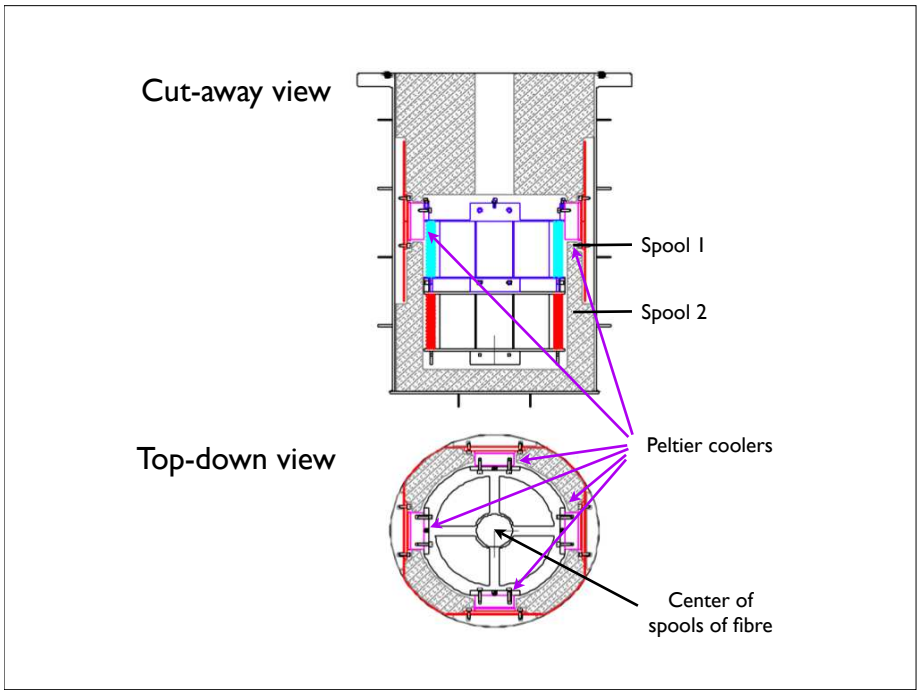

Figure 5.1: Schematic of cooler vessel.

Peltier coolers are thermoelectric heat pumps which use a current to transfer heat against the temperature gradient across a junction of two dissimilar elements [18]. An applied voltage creates a current as it forces the electrons to flow from the cold, high-density region toward the lower-density region. As the electrons move into a region of lower density, they expand and heat, much like a gas.

Copper fins leading from the back of the coolers to the outside of the vessel were designed to transfer the heat out of the container and into the shielding water. The inside of the cooler vessel was just large enough that the fibre spool could slide into it. Styrofoam insulation was used to fill as much of the empty space as possible.

5.2 Test 1

5.2.1 Fibres under test

Due to mechanical limitations, only the multimode Draka optical fibre was tested during Test 1 in June, 2009. 50 metres of this fibre were wound about a metal spool in a single layer. The spool was contained within the cooler vessel and was connected to the outside world via patch cables through which the light from the VCSEL was transmitted to the fibre under test and then back out to the photo-diode detector. Two additional reference measurements were also taken, one consisting of a short (2 metre) length of the Draka fibre, and one consisting of two of the patch cables connected by a fibre connector. The temperature was monitored via PT100 resistance thermometers. PT100 resistance thermometers are small strips of platinum which have stable temperature performance near $0°C = 100\Omega$. The entire test lasted approximately 65 hours in the low-dose facility. Four configurations involving having the coolers on or off and having the vessel in or out of the radiation environment were iterated through. Figure 5.2 is a timeline depicting the various configurations with the different regions indicated. Each region of interest will be

discussed in detail below. Transitions between the configurations were also of interest and will be discussed. Table 5.1 lists the radiation and temperature properties of each region. The attenuation is defined and calculated as in Equation 4.4 with the reference fibre consisting of two connected patch cables of the same length as the patch cables attached to the Draka fibre under test. Figure 5.3 is a schematic of the test set-up at the radiation facilities.

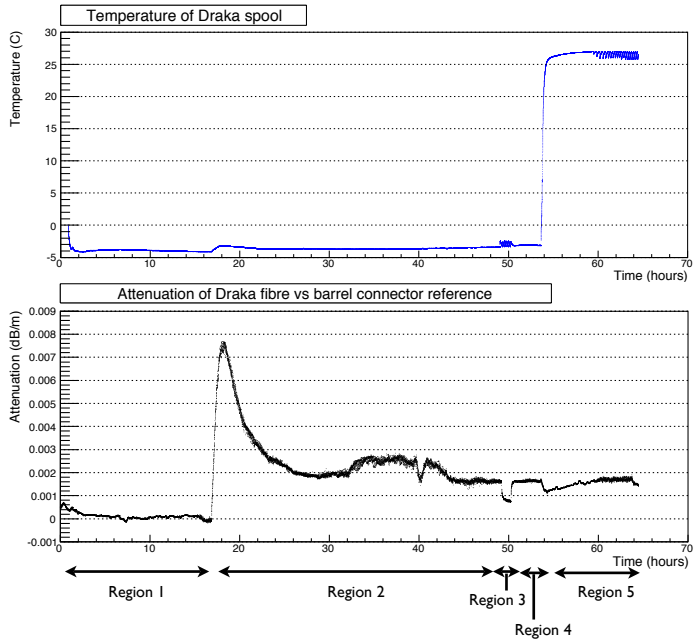

Figure 5.2: Timeline of Test 1 with regions indicated.

For reference and for scale, while Figure 5.2 shows the data for the entire run, Figure 5.4 presents the results for hours 0-51 during which most of the interesting behaviour occurred.

Results are presented with power output in units of dB/m so that predictions

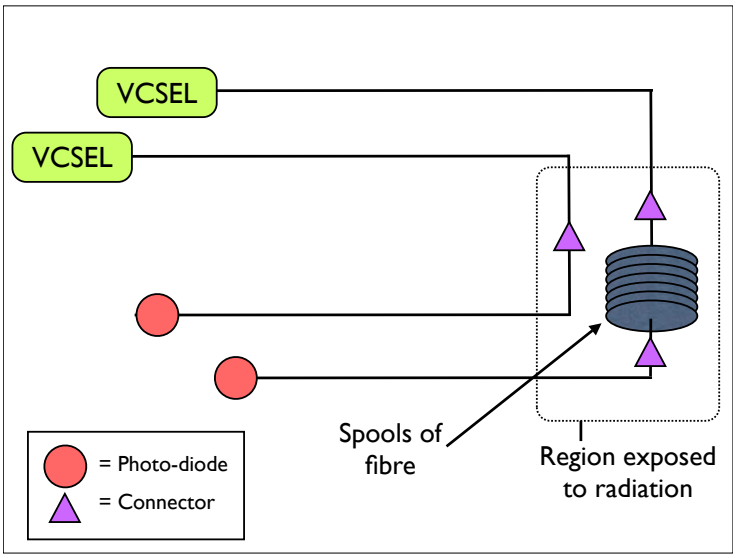

Figure 5.3: Schematic of the test set-up at the SCK-CEN facility.

can be made about attenuation for arbitrary lengths of fibre. All of the fibres under test were 50 m in length.

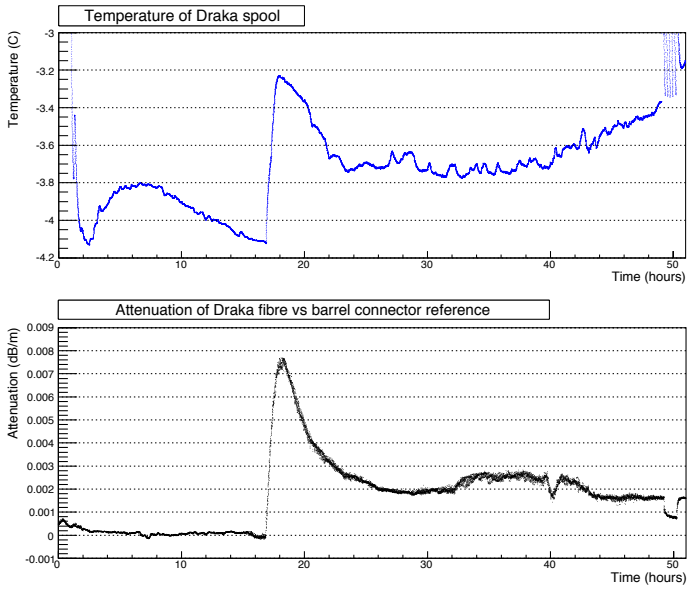

Figure 5.4: Test 1: The temperature of and attenuation of light in the Draka fibre over hours 0-51.

Table 5.1: Radiation and temperature properties of the regions shown in Figure 5.2.

Region	Hours	Radiation	Coolers
1	0-16.5	off	on
2	16.5-49	on	on
3	49-51	off	on
4	51-53.6	on	on
5	53.6-end	on	off

5.2.2 Region 1: Coolers on, radiation off

Figures 5.5 and 5.6 show the attenuation and temperature of the system during the first 16.5 hours of testing, when the vessel was submerged but remained out of the radiation. This first 16.5 hours of data is considered to be the zero attenuation state of the light and so all data is shifted along the y-axis so that the initial state is approximately 0 dB/m attenuation. The temperature begins to increase around hour 16.5 when the vessel is moved into the radiation.

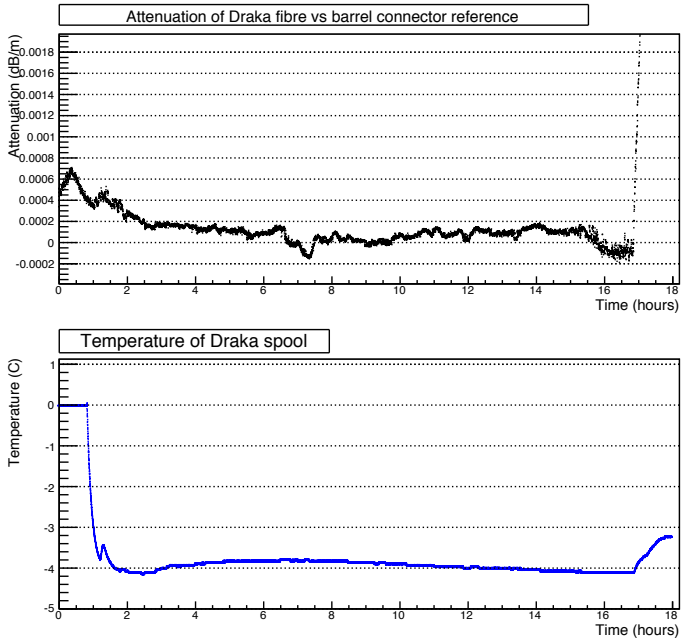

Figure 5.5: Test 1: The attenuation of light in and temperature of the Draka fibre over hours 0-17.

The coolers operated at maximum capacity during this period and maintained a temperature of approximately $-4\,^{\circ}\mathrm{C}$. The light output through the Draka fibre

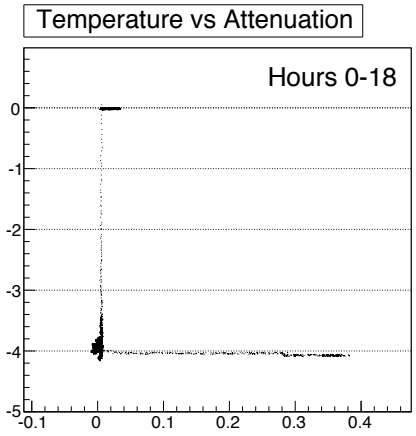

Figure 5.6: Test 1: Correlation of attenuation and temperature in the Draka fibre over hours 0-17.

remained stable over this period of time. At approximately hour 16.5, the vessel was lowered into the radiation environment. An immediate rise in temperature was observed and the attenuation of the light spiked upwards. The rise in temperature occurred because, as the coolers were already operating at maximum capacity while out of the radiation, they were unable to maintain their minimum temperature once the vessel was immersed in the radiation.

5.2.3 Region 2: Coolers on, radiation on

From hours 17 - 49 the vessel remained in the radiation environment (Figures 5.7 and 5.8). Immediately upon submersion into the radiation, the temperature rose, as noted above. However, after reaching a maximum temperature of $-3.22\,^{\circ}\mathrm{C}$, the temperature restabilised slightly lower at $-3.65\,^{\circ}\mathrm{C}$. Concurrently, the attenuation of the light reached its global maximum, peaking around hour 18 with an absolute attenuation of 0.4 dB. The attenuation then partially recovered and hovered around 0.1 dB for the remainder of this region of the timeline. It is interesting to note that from hours 35-45, the temperature rises and the attenuation falls.

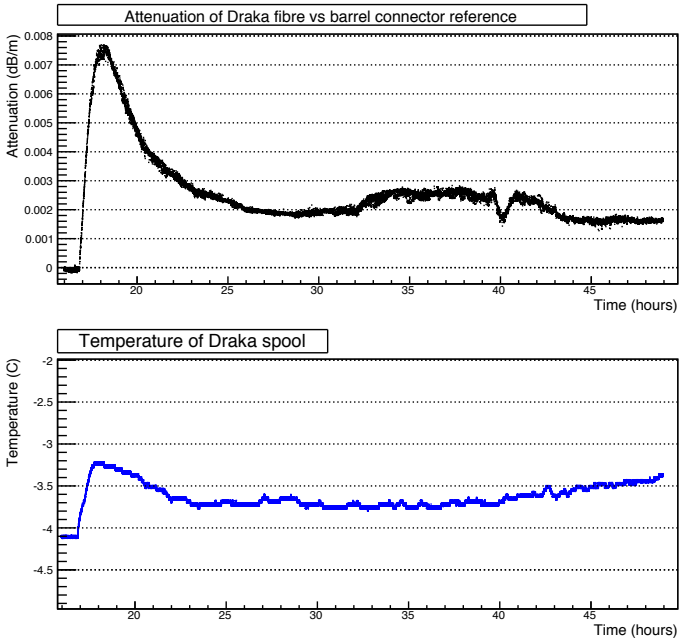

Figure 5.7: Test 1: The attenuation of light in and temperature of the Draka fibre over hours 17-49.

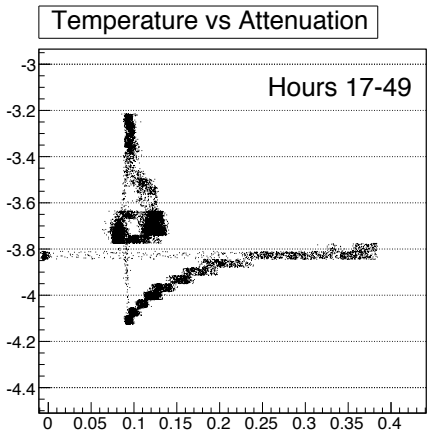

Figure 5.8: Test 1: Correlation of attenuation and temperature of the Draka fibre over hours 17-49.

5.2.4 Region 3: Coolers on, radiation off

From hours 49 - 51 (Figures 5.9 and 5.10), the vessel is programmed to maintain its current in-radiation minimum temperature of $-3.3\,^{\circ}\mathrm{C}$ but is then lifted out of the radiation environment. Over this two hour period, the temperature fluctuates periodically because the coolers must switch on and off to maintain the set temperature. The attenuation drops slightly over this period.

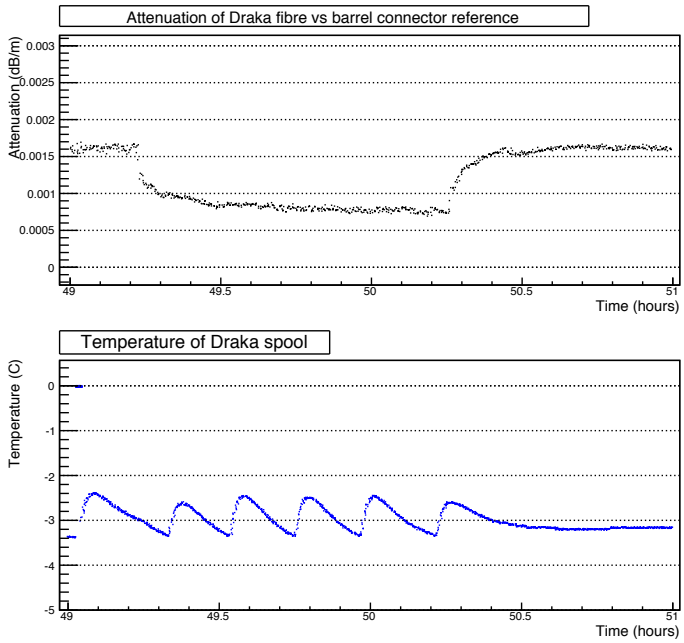

Figure 5.9: Test 1: The temperature of the Draka fibre over hours 49-51.

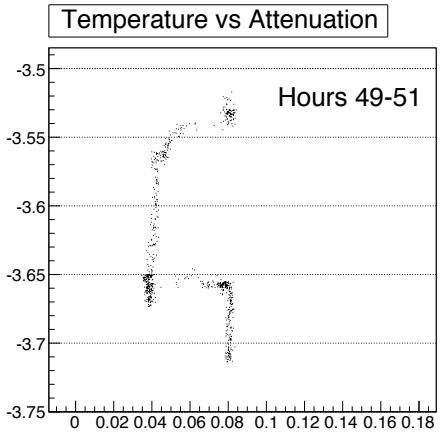

Figure 5.10: Test 1: Correlation of attenuation and temperature of the Draka fibre over hours 49-51.

5.2.5 Region 4: Coolers on, radiation on

At hour 51, the vessel is subsequently lowered back into the radiation environment. The attenuation returns to its previous higher level from hours 51 to 54 (see Figures 5.11 and 5.12).

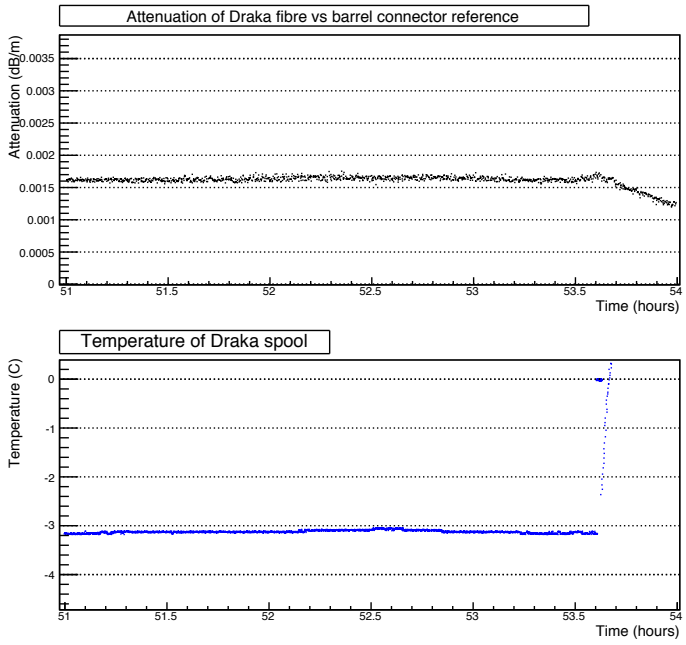

Figure 5.11: Test 1: The temperature of the Draka fibre over hours 51-54.

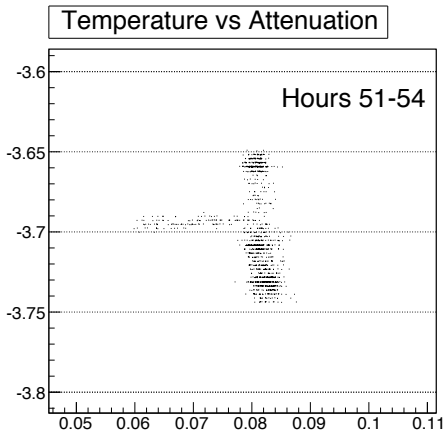

Figure 5.12: Test 1: Correlation of attenuation and temperature of the Draka fibre over hours 51-54.

5.2.6 Region 5: Coolers off, radiation on

At hour 53.6, the coolers are switched off and the vessel rapidly warms up to the temperature of the surrounding water (approximately 27 °C). As shown in Figures 5.13 and 5.14, the attenuation of the light drops as the temperature rises, but then as the temperature begins to re-stabilise, the attenuation begins to rise again. The temperature oscillates over the final six hours because once the temperature stabilised, the coolers were programmed to maintain that temperature for the remainder of the run even as the temperature of the room continued to increase.

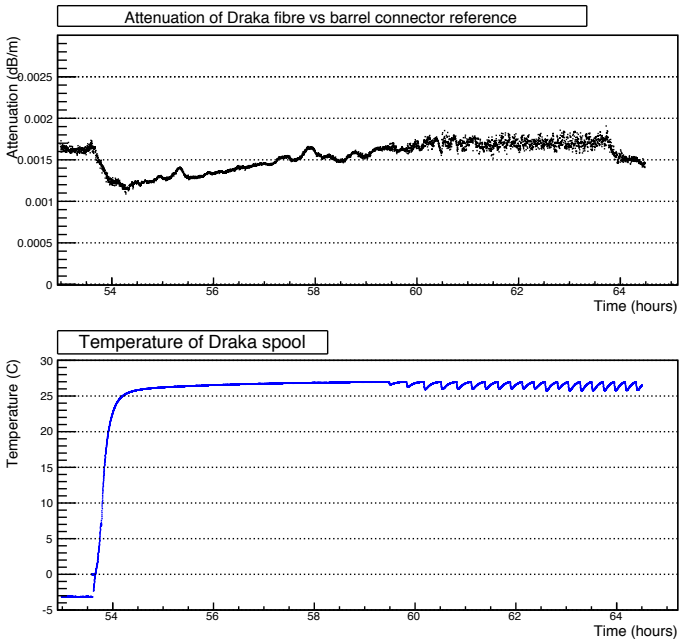

Figure 5.13: Test 1: The attenuation of light in and temperature of the Draka fibre over hours 53-66.

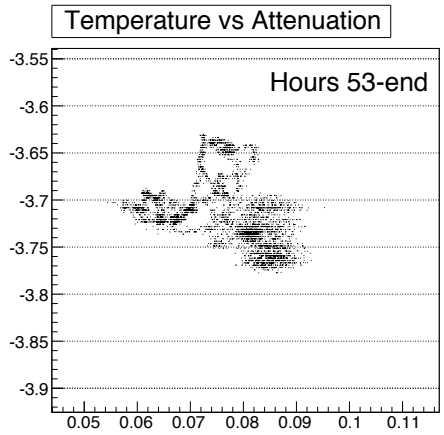

Figure 5.14: Test 1: Correlation of temperature and attenuation of the Draka fibre over hours 53-66.

5.2.7 Conclusions

The results of these tests made it difficult to separate temperature-induced effects from radiation damage-induced effects on the attenuation of the light through the fibre since in many cases, the level of radiation and the temperature of the spool varied in parallel. Additionally, the coolers operating at maximum capacity were only able to obtain temperatures on order of $-4\,^{\circ}\mathrm{C}$, which, while interesting, were not close enough to the desired goal of $-25\,^{\circ}\mathrm{C}$ to be able to make definitive statements about the interplay of radiation and SLHC-level cold environments. Thus it was determined that it would be ideal to run a second set of tests following the same model but making improvements on the design and execution of the experiment.

5.3 Test 2

5.3.1 Upgrades to the cooler vessel

Test 2 was conducted at the same facility at SCK-CEN in August, 2009. Test 1 had indicated that the cooler vessel needed to be modified if it was to obtain the desired temperature of $-25\,^{\circ}\mathrm{C}$. Thus, the original single-layer Peltier coolers were replaced with double-layered Peltier coolers. The original coolers could, under ideal conditions, maintain a temperature difference across their surfaces of $\Delta T = 30\,^{\circ}\mathrm{C}$. The new coolers could maintain a $\Delta T = 60\,^{\circ}\mathrm{C}$. Additionally, the aluminium walls of the original cooler vessel were replaced by an all-copper construction to increase the thermal conductivity between the coolers and the outside environment, and the number and depth of the fins increased so that the surface area in contact with the water increased.

5.3.2 Fibres under test

Two multimode optical fibres which are potential candidates for the SLHC upgrade were tested: the Infinicor SX+[2] and the Draka[3] fibre. 50 metres of each was wound around a metal spool. Additionally, a short (2 m) length of the Infinicor SX+ fibre was contained within the vessel, as was a barrel connector linking two of the patch cables. Thus, either the short Infinicor SX+ or the patch cable data could be used as a reference to eliminate the (generally minimal) effect of radiation on the

[2] www.fiberoptics4sale.com/pdf/Corning-Infinicor-SX+-Spec-Sheet.pdf

[3] http://www.drakafiber.com/

patch cables leading into the vessel for the attenuation of the long fibres under test. Figure 5.15 shows the behaviour of each of the references over the entire run. The patch cable data was chosen as the reference for the final data analysis and for the figures presented here due to its greater stability in the radiation.

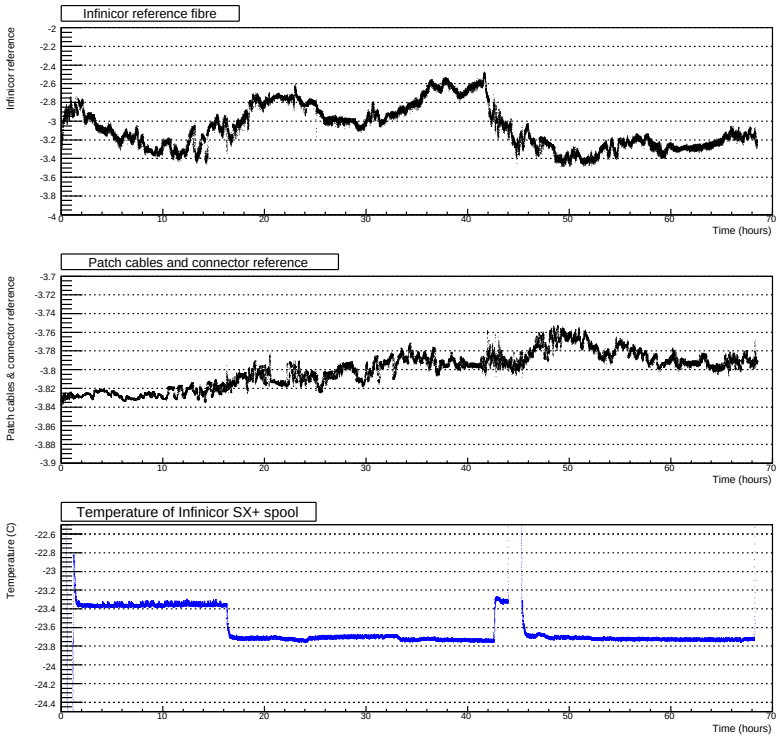

Figure 5.15: Both references taken during Test 2 vs. time.

Two temperature sensors (PT 100 resistance thermometers) were included in the set-up. One of the sensors was attached to the upper spool (see Figure 5.16), wound with the Draka fibre, and the second was attached to the lower spool, wound with the Infinicor SX+ fibre, both just a single layer thick. This meant that the temperature of the individual spools of fibre could be monitored independently. The temperature of the coolers was controlled externally from a remote location

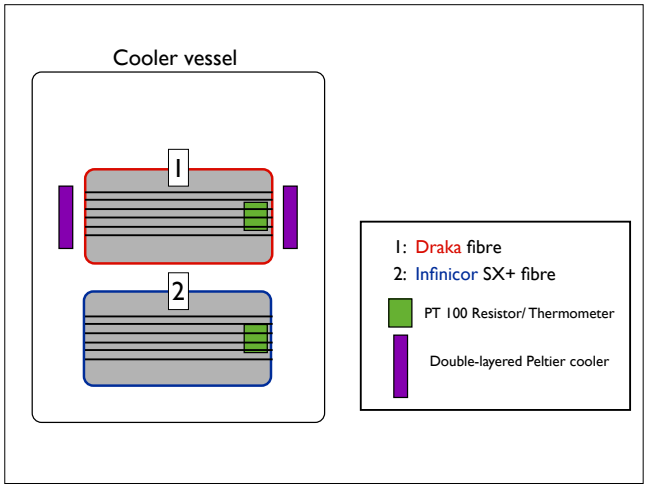

Figure 5.16: Schematic of vessel.

using a LabVIEW^{TM} program which was capable of turning on and off the 4 coolers independently. The temperature of the upper spool (the Draka fibre) was chosen as the representative temperature of the vessel for the purpose of controlling which coolers were switched on and off in the attempt to maintain the goal temperature. Test runs completed at Oxford had indicated that it was feasible for the vessel to maintain a temperature of $-20\,^{\circ}\mathrm{C}$ – $-25\,^{\circ}\mathrm{C}$. While the effect of radiation on both the performance of the coolers and the achievable range of temperatures was unknown, the heating effects were simulated in the laboratory by using Ohmic heating.

The second test was run for approximately 68.5 hours. Figures 5.17, 5.18, 5.19, and 5.20 are labelled with the regions of interest for this run. As in Section 5.2, each region will be discussed. Table 5.2 provides the details for each region.

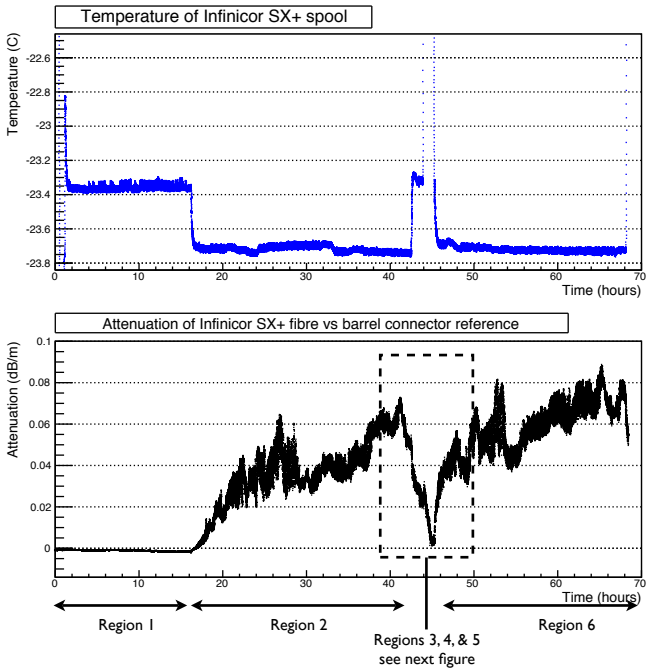

Figure 5.17: Full run of Infinicor SX+ fibre with regions of interest labelled.

Table 5.2: Radiation and temperature properties of the regions shown in Figures 5.17, 5.18, 5.19, and 5.20.

Region	Hours	Radiation	Coolers
1	0-16	off	on
2	16-42	on	on
3	42-44	off	on
4	44-44.75	off	off
5	44.75-45.25	off	on
6	46-end	on	on

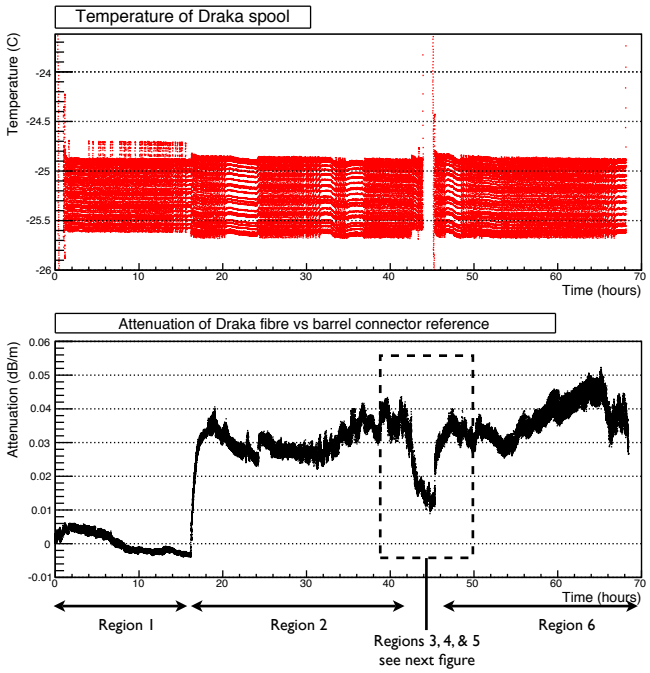

Figure 5.18: Full run of Draka fibre with regions of interest labelled.

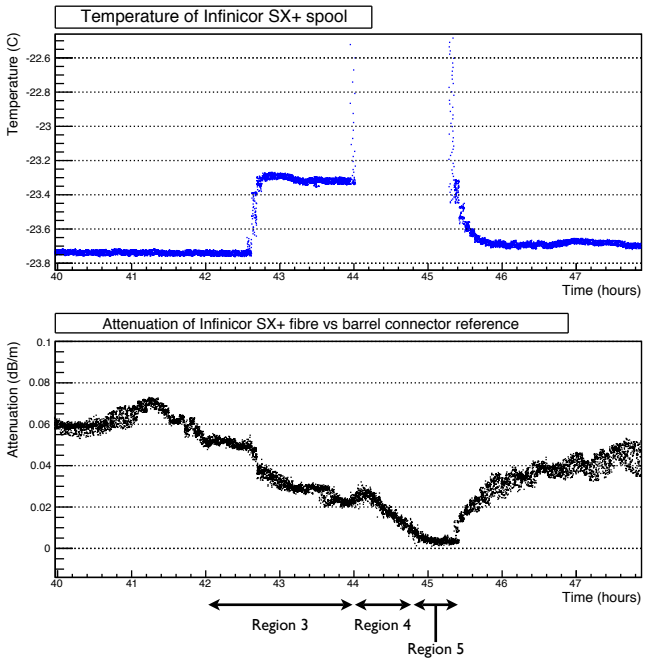

Figure 5.19: Zoomed-in section of Infinicor SX+ fibre with regions of interest labelled.

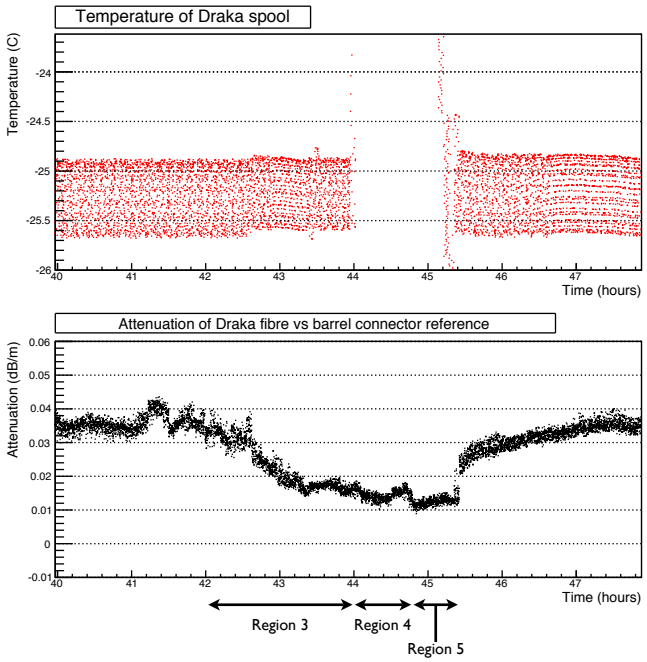

Figure 5.20: Zoomed-in section of Draka fibre with regions of interest labelled.

5.3.3 Region 1: Coolers on, radiation off

The first 16 hours of this test run were conducted with the Peltier coolers on but with the vessel remaining outside of the radiation environment. This served to establish a baseline light level for the fibres operating at sufficiently cold temperatures. The coolers were able to stabilise the vessel at around $-23\,^{\circ}\mathrm{C}$ to $-25\,^{\circ}\mathrm{C}$. Two thermometers were in the vessel, one on each fibre spool. The Draka spool was closest to the Peltier coolers and the thermometer on the Draka spool was arbitrarily chosen as the one which would control when the Peltier coolers switched on and off. This resulted in a greater variability in temperature for this spool, relative to the Infinicor spool. Because the Infinicor spool was below the Draka spool, it never got as cold as the Draka spool but it maintained a much more stable temperature throughout the run. The temperature profiles of both spools can be seen in Figures 5.17 and 5.18.

After running continuously for approximately 16 hours, the vessel, with the coolers remaining on, was lowered into the radiation environment. Figures 5.21, 5.23, 5.22, and 5.22 show the data taken during Region 1.

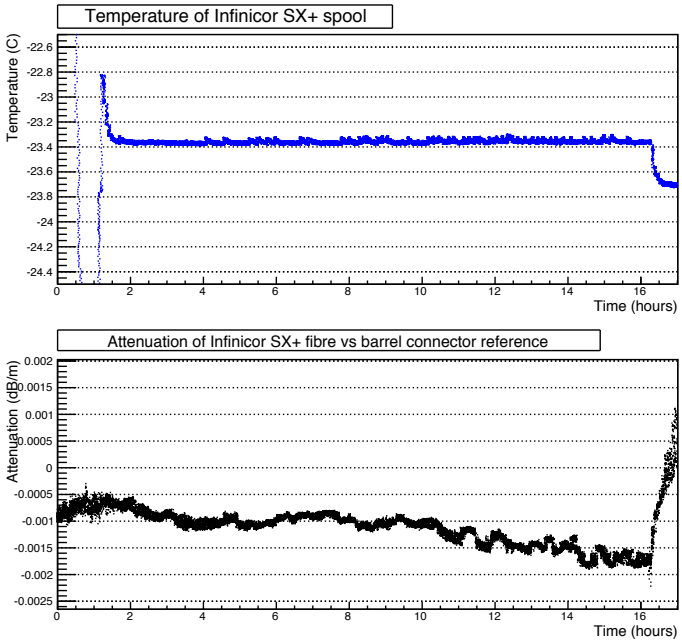

Figure 5.21: Test 2: The attenuation of light in and temperature of the Infinicor SX+ fibre over hours 0 to 17.

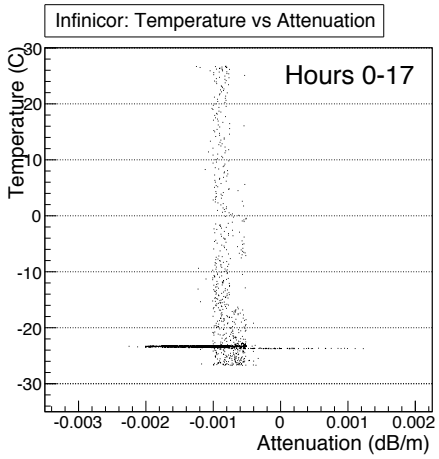

Figure 5.22: Test 2: Correlation of attenuation and temperature in the Infinicor SX+ fibre over hours 0 to 17.

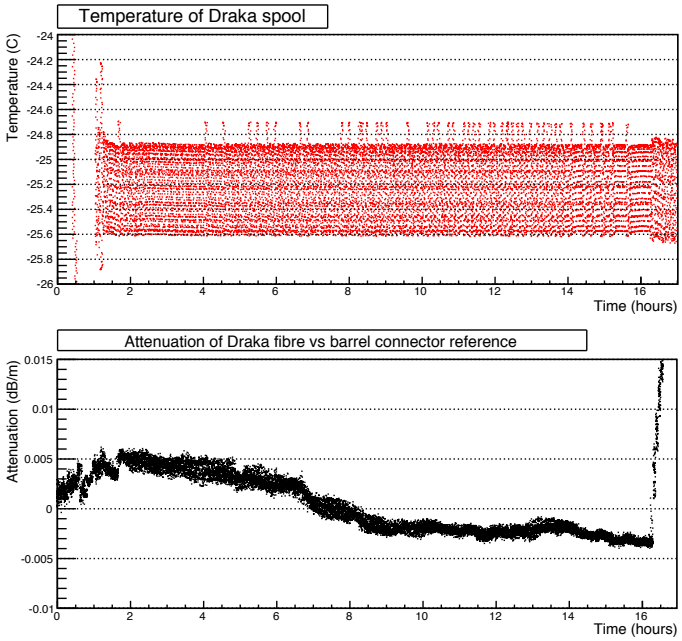

Figure 5.23: Test 2: The attenuation of light in and temperature of the Draka fibre over hours 0 to 17.

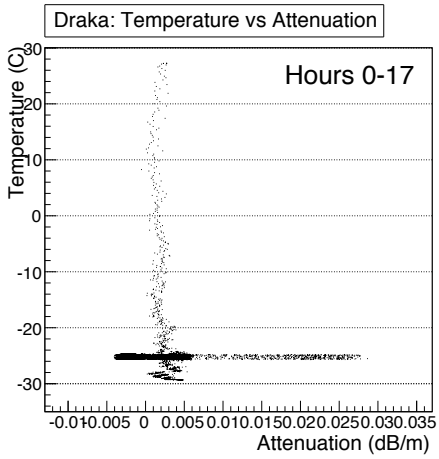

Figure 5.24: Test 2: Correlation of attenuation and temperature in the Draka fibre over hours 0 to 17.

5.3.4 Region 2: Coolers on, radiation on

Immediately after the cold vessel was lowered into the radiation environment, the attenuation of both the Draka and the Infinicor SX+ fibre increase, as expected. Interestingly, however, neither fibre demonstrates the drastic spike accompanied by a subsequent recovery, as seen during previous runs. This observation is the first observable difference that operating at cold temperatures can make on the radiation hardness of multimode fibres. The damage mechanism observed previously remains, but the recovery mechanism does not.

The Draka fibre jumps in attenuation more than the Infinicor SX+ fibre does, but then on the global timescale of the entire run, the Draka fibre maintains a much closer to constant level of light whereas the Infinicor SX+ fibre is significantly more affected by radiation damage, as seen in its gradual increase in radiation-induced attenuation. Over the period ranging from hours 16-42, the Draka fibre, Figures 5.25 and 5.26, maintains a relative attenuation of 0.03 dB/m.

The attenuation of the Infinicor SX+ fibre, on the other hand, Figures 5.27 and 5.28, slopes upward gradually from 0 dB/m to 0.06 dB/m.

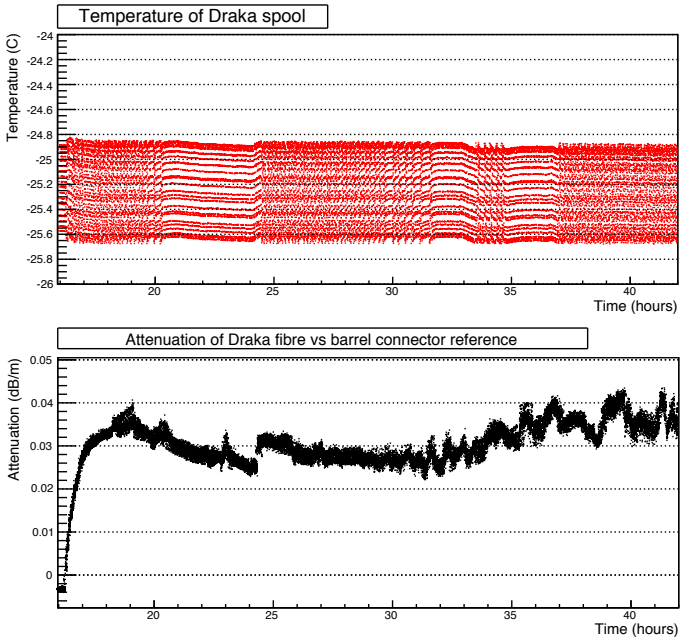

Figure 5.25: Test 2: The attenuation of light in and temperature of the Draka fibre over hours 17 to 42.

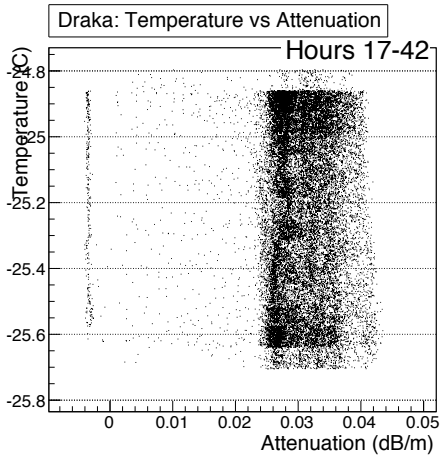

Figure 5.26: Test 2: Correlation of attenuation and temperature in the Draka fibre over hours 17 to 42.

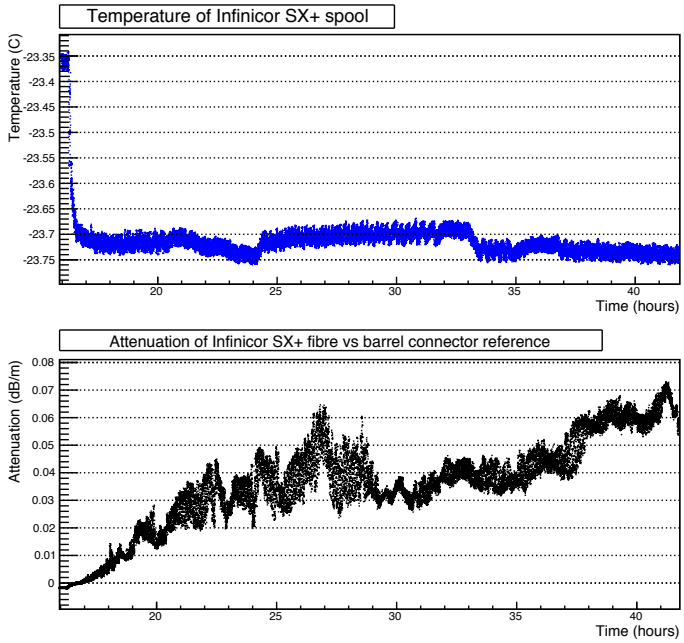

Figure 5.27: Test 2: The attenuation of light in and temperature of the Infinicor SX+ fibre over hours 17 to 42.

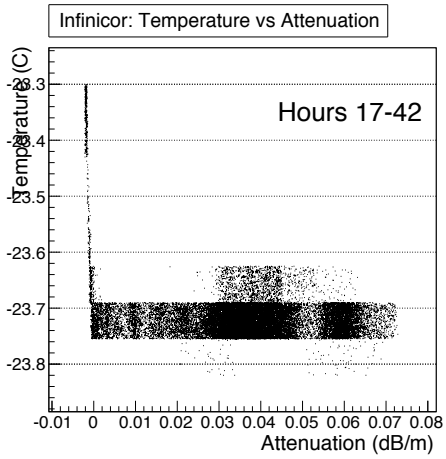

Figure 5.28: Test 2: Correlation of attenuation and temperature in the Infinicor SX+ fibre over hours 17 to 42.

5.3.5 Region 3: Coolers on, radiation off

The next series of changes were implemented to isolate the effects of radiation, temperature, and photobleaching on the performance of the two fibres. At approximately hour 42, the coolers are left running but the vessel is lifted out of the radiation environment. The Draka fibre, Figures 5.29 and 5.30, experiences a slow partial recovery, with the attenuation dropping 0.018 dB/m.

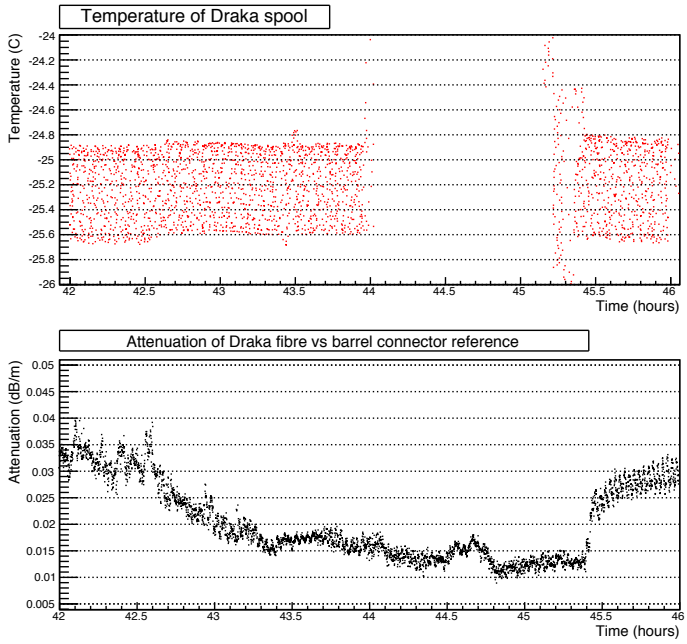

Figure 5.29: Test 2: The attenuation of light in and temperature of the Draka fibre over hours 42 to 46.

The Infinicor SX+ fibre, Figures 5.31 and 5.32, demonstrates a similar gradual partial recovery with a 0.04 dB/m change in attenuation. The Infinicor SX+ fibre recovers more than the Draka fibre.

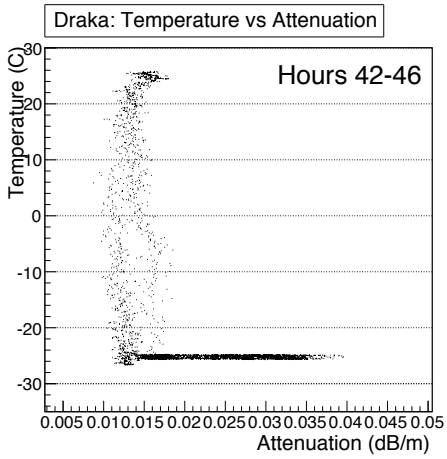

Figure 5.30: Test 2: Correlation of attenuation and temperature in the Draka fibre over hours 42 to 46.

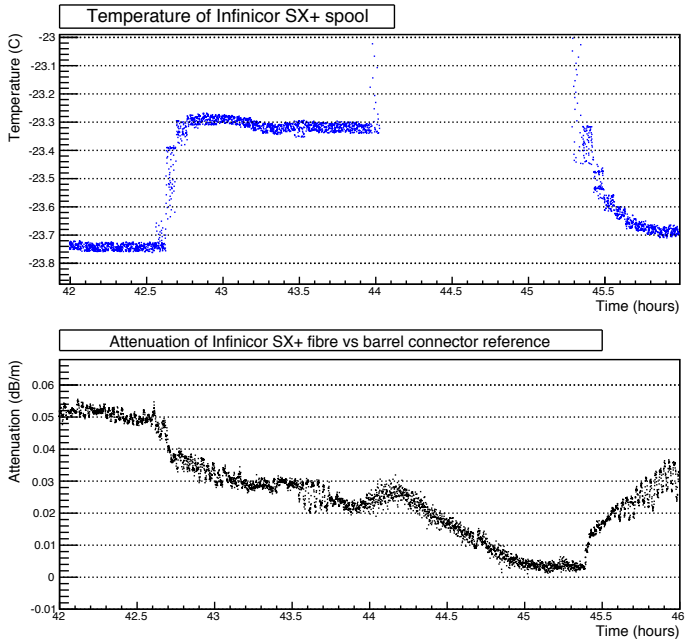

Figure 5.31: Test 2: The attenuation of light in and temperature of the Infinicor SX+ fibre over hours 42 to 46.

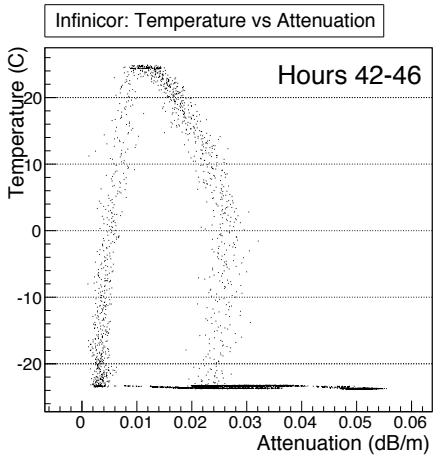

Figure 5.32: Test 2: Correlation of attenuation and temperature in the Infinicor SX+ fibre over hours 42 to 46.

As the only variable changed during this segment was the removal of irradiation, a working hypothesis for both of these gradual partial recoveries of the two fibres is that they can be attributed to removal of electrons from the STH, self-trapped holes (defects in the structure of the fibre). Radiation increases the attenuation of the light propagating through the fibre via two mechanisms. It gives electrons the energy to move into pre-existing defects created during the manufacturing process of the fibre, and these electrons are able to absorb propagating photons. Radiation also creates new defects in the glass structure, thus increasing the density of STH, which can continue to be filled by mobile electrons and which then increasingly absorb visible light.

Removing the fibres from the radiation but maintaining the cold temperature of the vessel means that the observed recovery can be attributed to what is known as the photo-bleaching effect. Photo-bleaching occurs when the light signal is allowed to knock some of the trapped electrons out of their holes and the holes are not immediately refilled. The constant cold temperature also means that this portion of the recovery cannot be attributed to temperature change induced effects, but as will be noted below, temperature does prove to be an influential variable as well.

5.3.6 Region 4: Coolers off, radiation off

From hour 44-44.75, the vessel remained out of the radiation and the coolers were turned off as well, allowing the vessel to warm up to the temperature of the shielding tank of water (approximately 30 °C). Here, the performances of the two

fibres again diverge. The attenuation of the Draka fibre neither increases nor decreases but rather the light maintains a stable output (Figures 5.29 and 5.30). Thus, the increased temperature does not anneal any of the damage done to the Draka fibre. The attenuation of the Infinicor SX+ fibre, however, does change with the increase in temperature of the vessel (Figures 5.31 and 5.32). As the vessel warms up, the Infinicor SX+ attenuation decreases at a faster rate than it had improved when just the radiation was removed. This observation, combined with the results from Region 6, indicates that in the Infinicor SX+ fibre, warmer temperatures anneal some of the damage due to radiation. This observation is consistent with the literature [40], which indicates that increasing the temperature of the fibre may allow the structure of the fibre to rearrange itself on a molecular level and thus mitigate some of the damage caused by radiation. The annealing can be considered true annealing because once the attenuation begins to rise again, it is a gradual increase and not the drastic spike experienced in the previous tests.

5.3.7 Region 5: Coolers on, radiation off

During region 5, from hours 44.75 to 45.25, the vessel remained out of the radiation environment but the coolers were turned back on and set to run at the previous level (approximately $-25\,^{\circ}\mathrm{C}$). During this period, neither the Draka fibre nor the Infinicor SX+ fibre experienced any significant changes in attenuation (Figures 5.29, 5.30, 5.31, and 5.32). This stability is consistent with previous trends of annealing.

5.3.8 Region 6: Coolers on, radiation on

Finally, for the last segment of the run, the coolers were left running and the vessel was re-lowered back into the radiation at hour 46. More unexpected effects were observed, and the Draka and Infinicor SX+ fibre again reacted differently.

The attenuation of the Draka fibre returned to its previous level of 0.03 dB/m (Figures 5.33 and 5.34).

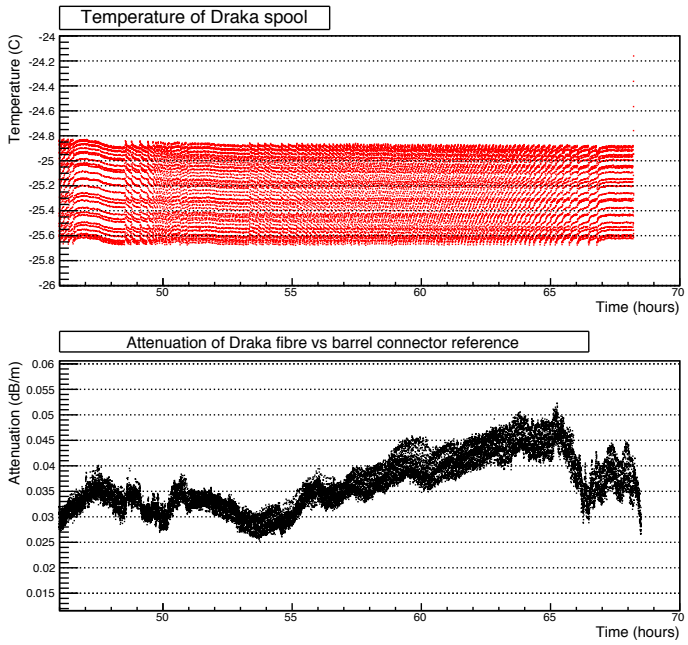

Figure 5.33: Test 2: The attenuation of light in and temperature of the Draka fibre over hours 46 to 70.

This behaviour supports the effects observed throughout region 4 whereby the Draka fibre does not undergo any temperature-induced annealing (see Sections 2.3.3 and 4.2.1 for descriptions of this effect). Because its attenuation returns to precisely

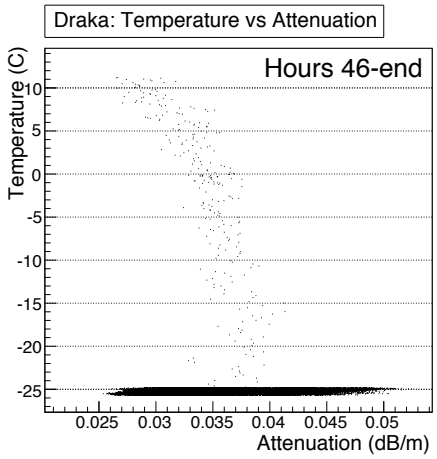

Figure 5.34: Test 2: Correlation of attenuation and temperature in the Draka fibre over hours 46 to 70.

the previous level from before being removed from the radiation and from before being warmed up, it appears that the initial damage sustained by the fibre (at hour 16) remained but did not worsen even after many hours of radiation. The Infinicor SX+ fibre continued to follow the model developed in the literature. Upon reimmersion in the radiation environment, it experienced an immediate rise in attenuation (Figures 5.35 and 5.36).

The level of attenuation, however, did not return immediately to its previous high as the Draka fibre did. Instead, the attenuation followed gradual rise which was remarkably similar to the attenuation rise of the fibre during the initial period of radiation (Region 2). Thus we can conclude that for the Infinicor SX+ fibre, increasing the temperature allowed the fibre to partially anneal. The initial fast rise in attenuation within Region 6 can probably be attributed to a re-filling of the still-

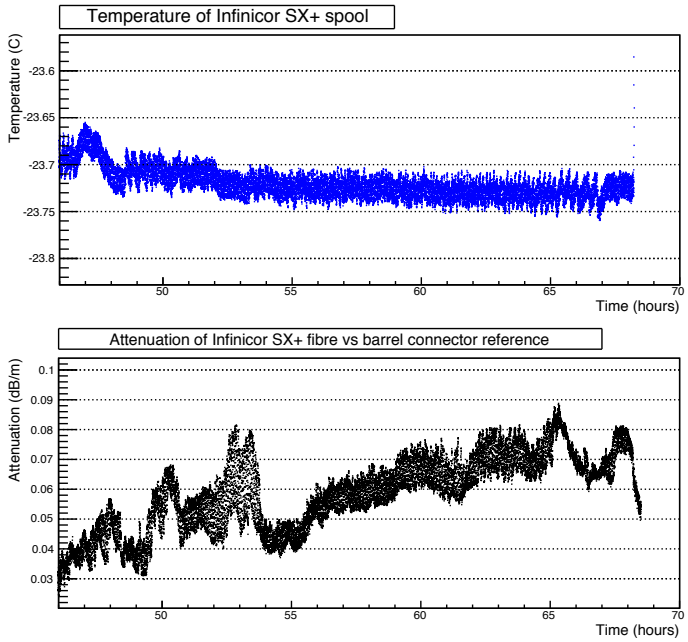

Figure 5.35: Test 2: The attenuation of light in and temperature of the Infinicor SX+ fibre over hours 46 to 70.

existing (un-repaired) STH, and then the subsequent slower increase in attenuation can be attributed to continued damage from the radiation.

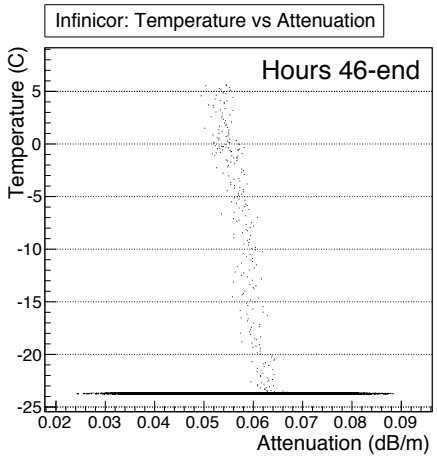

Figure 5.36: Test 2: Correlation of attenuation and temperature in the Infinicor SX+ fibre over hours 46 to 70.

5.3.9 Second-order temperature dependence

The purpose of these series of tests was to determine whether either the Draka or the Infinicor SX+ fibre, or both, would be suitably radiation hard for use in the SLHC upgrade. This section examines the effect on radiation-induced attenuation of very small changes in temperature. The results presented in this section are not conclusive when it comes to answering the question about feasibility of these fibres for use in the SLHC but nonetheless, they are an interesting physics phenomena which was observed at the cold radiation tests.

The vessel containing the fibres was cooled by four Peltier coolers equally spaced about its interior circumference. These coolers were such that they have two modes of operation: on and off. An upgrade made between the first and second test runs was to allow each individual Peltier cooler to be switched on and off independently, but each Peltier operated in step-function form. This meant that when a temperature for the vessel was chosen and set by the LabVIEW ^{TM} program, what actually occurred, as measured by the PT 100 resistance thermometers, was that the coolers would run until the vessel temperature dropped below the set value, at which point one cooler at a time would switch off so that the vessel could warm up. As soon as the vessel had warmed up enough for its temperature to rise above the set temperature, the cooler(s) which had switched off would switch on again and the process would be repeated. In practice, a minimum of 3 coolers ran at all times so no more than one cooler was ever off at a time. As shown below, this resulted in the temperature profile, on short time scales, following an approximately

sinusoidally periodic form.

What becomes interesting about this is to compare to the temperature plots what the attenuation plots were doing concurrently, both before and during the fibres' time in the radiation environment. Figures 5.37, 5.38, 5.39, and 5.40 are, respectively, the attenuation and temperature profiles for the Draka and Infinicor SX+ fibres, as well as the correlation plots of attenuation vs. temperature from hour 5 to hour 6, which was before the vessel was irradiated.

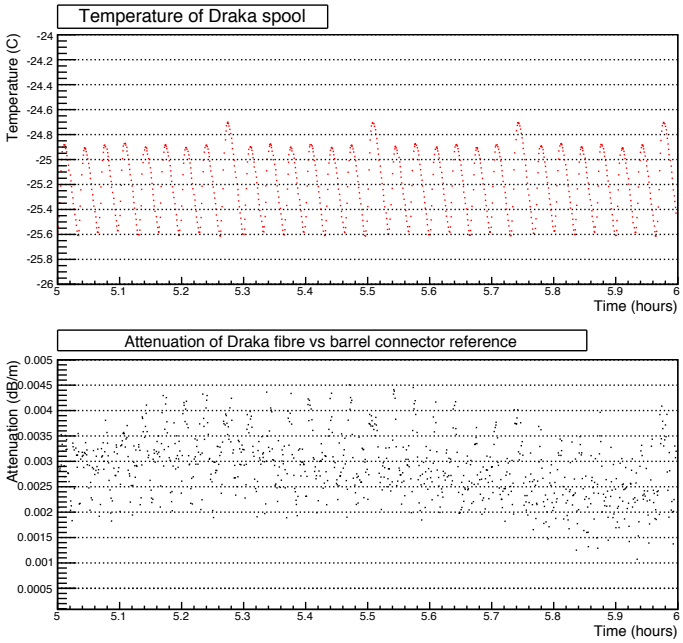

Figure 5.37: Test 2: The attenuation of light in and temperature of the Draka fibre over hours 5 to 6.

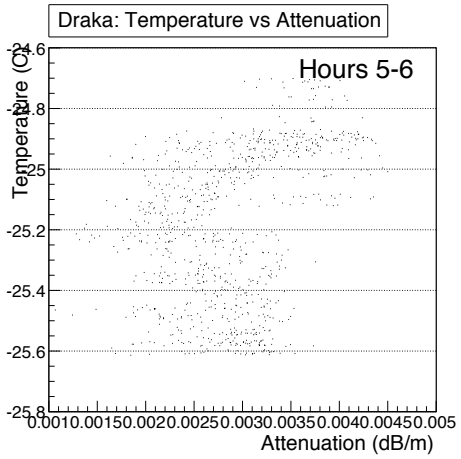

Figure 5.38: Test 2: Correlation of attenuation and temperature in the Draka fibre over hours 5 to 6.

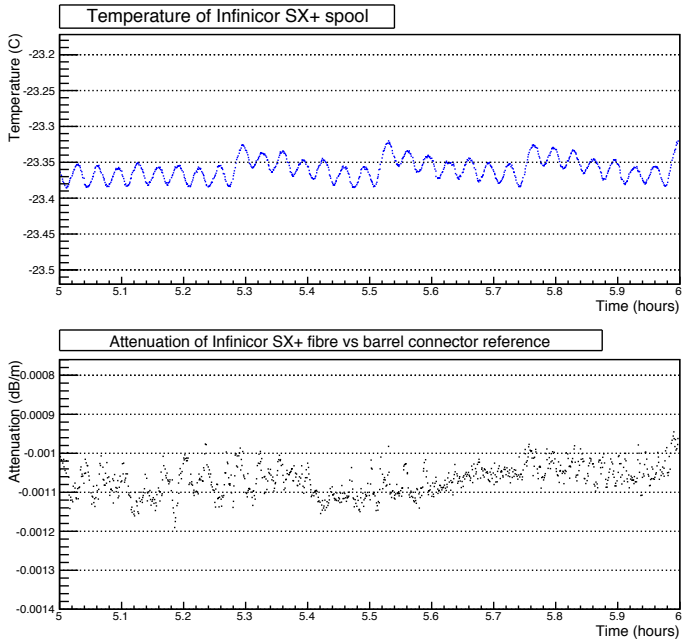

Figure 5.39: Test 2: The attenuation of light in and temperature of the Infinicor SX+ fibre over hours 5 to 6.

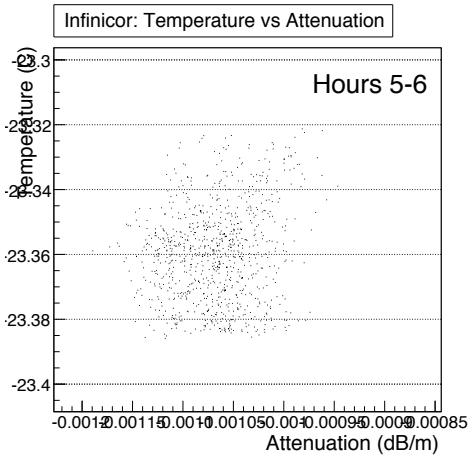

Figure 5.40: Test 2: Correlation of attenuation and temperature in the Infinicor SX+ fibre over hours 5 to 6.

Then, Figures 5.41, 5.42, 5.43, and 5.44 show the same four plots except during hours 25 to 26 when the fibres were being irradiated.

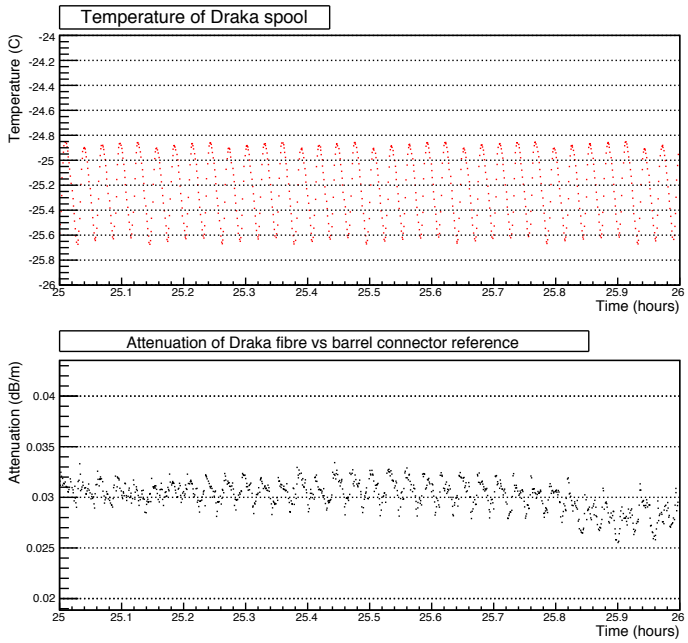

Figure 5.41: Test 2: The attenuation of light in and temperature of the Draka fibre over hours 25 to 26.

It is interesting that the light attenuation clearly depends on temperature, particularly sensitively when the fibre is undergoing radiation, and more in the radiated Infinicor fibre than the Draka fibre.

Table 5.3 presents the RMS variation of the optical power and temperature of each of the relevant regions for this section.

Table 5.3: Temperature and RIA variations of fibres.

	Draka fibre vs barrel reference	Infinicor fibre vs barrel reference
Total run		
dB variation	0 to 0.052	0 to 0.09
dB RMS	0.01496	0.02582
Temperature variation	-25.7 to -24.7	-23.75 to -23.3
Temperature RMS	n/a	n/a
Fit to correlation plot (slope)	-31.1 +/- 7.1	-25.0 +/- 3.8
Hours 5-6		
dB mean	0.002448	-0.0009934
dB RMS	0.0008073	8.383e-05
Temperature mean	-25.2	-23.36
Temperature RMS	0.2483	0.01454
Fit to correlation plot (slope)	140.8 +/-2.9	60.0 +/- 0.2
Hours 25-26		
dB mean	0.03017	0.03566
dB RMS	0.00142	0.006331
Temperature mean	-25.22	-23.71
Temperature RMS	0.2611	0.01074
Fit to correlation plot (slope)	65.3 +/- 1.4	1.0 +/- 0.0

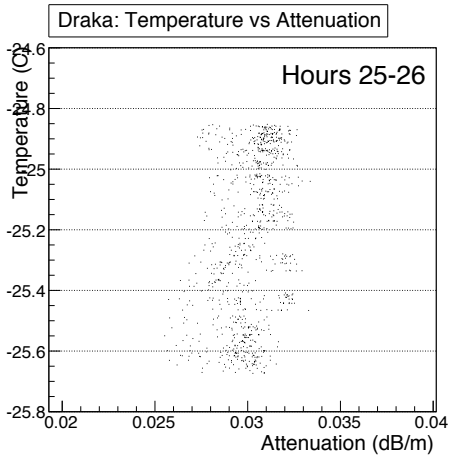

Figure 5.42: Test 2: Correlation of attenuation and temperature in the Draka fibre over hours 25 to 26.

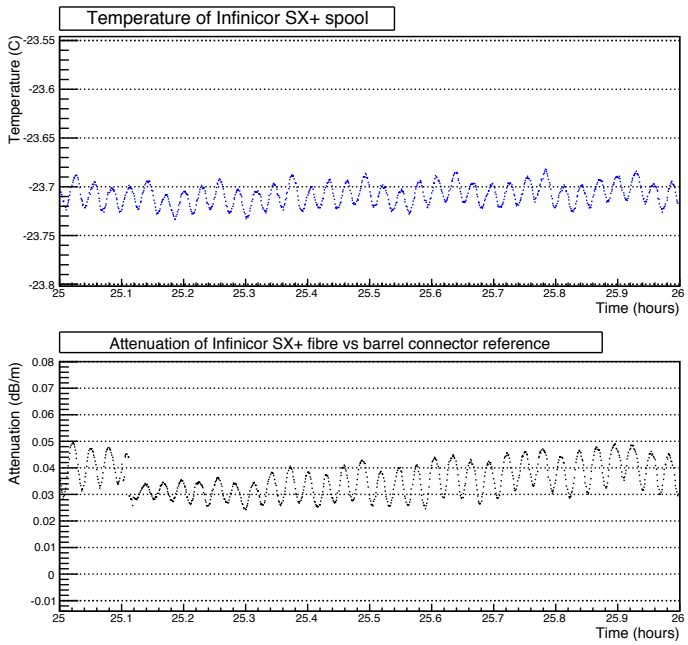

Figure 5.43: Test 2: The attenuation of light in and temperature of the Infinicor SX+ fibre over hours 25 to 26.

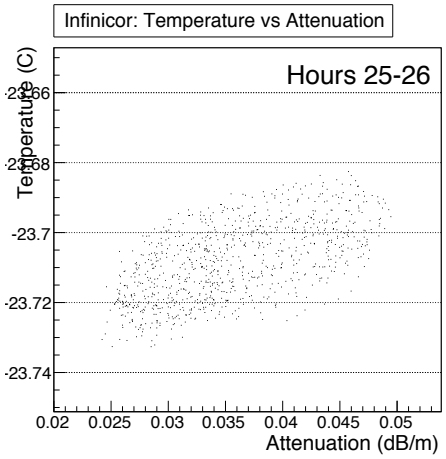

Figure 5.44: Test 2: Correlation of attenuation and temperature in the Infinicor SX+ fibre over hours 25 to 26.

5.3.10 Tentative conclusions from Test 2

During test two, the fibres were immersed in the radiation and their temperature stabilised at the desired level, so tentative conclusions can be made about their potential for use in the inner detector of the SLHC. The second run lasted for 68.5 hours in a radiation environment producing 0.51 kGy(Si)/hour of damage. The total radiation dose experienced by both fibres was 41.785 kGy(Si). Without any safety factors applied, the upgraded inner detector of ATLAS will experience a total dose of 250 kGy(Si) over its lifetime at the SLHC. Thus, these trials at SCK-CEN can be used to eliminate unsuitable fibres but further tests are still needed, in higher dose-rate facilities, in order to more conclusively understand how the fibres will respond over their lifetime in the high radiation environment of the inner detector of the SLHC.

The results from the tests presented here are promising. The Draka fibre performs better over the long term and after the 41.785 kGy(Si) dose of radiation demonstrated an attenuation of 0.05 dB/m. At an estimated length of 100 m, fibres to be used in the SLHC would then sustain a total attenuation of 5 dB after 41.785 kGy(Si) of radiation. 5 dB is larger than the desired suitable performance, which is 1 dB of loss over the lifetime of the fibres, but dose rate may affect total attenuation in such a way that these higher dose rate tests over-estimate the damage done to the fibres at this total dose. Additionally, if the trend for the Draka fibre performance demonstrated here, with one initial large jump in attenuation but then a subsequent flat behaviour even with increasing dose, continues to hold for future tests, it may

be suitable for use in the SLHC.

The Infinicor SX+ fibre does not perform as well as the Draka fibre. Not only does its attenuation increase approximately monotonically with increasing dose (over time in the radiation environment), but its absolute attenuation at the end of the run is higher than that of the Draka fibre, approaching 0.09 dB/m.

Chapter 6

Conclusions and future work

The SLHC programme intends on increasing the integrated luminosity of the LHC by an order of magnitude, from 300 fb^{-1} to 3000 fb^{-1}. Studies on predicted radiation doses for the inner detectors of the CMS and ATLAS experiments at the SLHC are underway, but a reasonable assumption to make is that radiation dose will scale with luminosity [4].

The location within the ATLAS inner detector (at 30 cm from the beam line) that is expected to experience the highest doses of radiation will sustain a total dose of 250 kGy(Si). Future estimates and tests will multiply this number by a safety factor as well. Additionally, it is expected that regions of the inner detector will vary in temperature, from $-25\,^{\circ}C$ to $30\,^{\circ}C$ [32], [37].

While much work remains to be done before the SLHC is achieved, the results of the tests presented here indicate that its reality is, at the least, still conceivable. The purpose of this particular project was twofold: first, to minimise the instabilities in fibre optoelectronic systems so as to maximise data transmission at the SLHC, and

second, to perform preliminary tests of fibre performance at cold temperatures in radiation environments. Results from the first part, presented in Chapter 4, indicate that the ATLAS and CMS collaborations should take into account the temperature sensitivity of various components of their fibre-optic systems, particularly that of the couplers used to moderate the light signal. Results from the second part, presented in Chapter 5, are cautiously optimistic as to whether suitably temperature- and radiation-hard fibres exist. An approximate upper limit on light loss is currently considered to be 1 dB total loss, which may or may not be an acceptable level of loss, depending on other choices made about light sources, fibre path lengths, dose rate, total dose and other parameters.

Since previous work has indicated that radiation dose rate also affects fibre performance, more tests are necessary before any conclusive statements can be made about these two particular multimode fibres, the Draka and the Infinicor SX+. These results also indicate that it is very difficult, if not impossible, to theoretically predict the behaviour of optoelectronic fibres at cold temperatures in radiation environments. Their performances vary dramatically with fibre type and sensitively with temperature. Their performance is as expected qualitatively from the literature with both total radiation dose and radiation dose rate. Thus, it is vital that future R&D for detector physics take into account the necessity of experimentally testing the components before they are used.

Appendix A

Derivation of Maxwell's Equations in an Infinite Dielectric Cylindrical Waveguide

A.1 Maxwell's equations

In a linear, isotropic, dielectric material, Maxwell's equations can be written as follows:

$$\overrightarrow{\nabla} \times \overrightarrow{E} = -\frac{\partial \overrightarrow{B}}{\partial t} \tag{A.1}$$

$$\overrightarrow{\nabla} \times \overrightarrow{H} = \frac{\partial \overrightarrow{D}}{\partial t} \tag{A.2}$$

$$\overrightarrow{\nabla} \cdot \overrightarrow{D} = 0 \tag{A.3}$$

$$\overrightarrow{\nabla} \cdot \overrightarrow{B} = 0 \tag{A.4}$$

where $\overrightarrow{D} = \epsilon \overrightarrow{E}$ and $\overrightarrow{B} = \mu \overrightarrow{H}$. ϵ is the permittivity of the dielectric material and μ is the permeability.

A.2 Solutions to the differential equations

To find generic solutions to these differential equations we want to decouple the equations. To do this, we will use the vector identity

$$\overrightarrow{\nabla} \times (\overrightarrow{\nabla} \times \overrightarrow{A}) = \overrightarrow{\nabla}(\overrightarrow{\nabla} \cdot \overrightarrow{A}) - \nabla^2 A. \tag{A.5}$$

The curl of Equation A.1 yields

$$\begin{aligned}
\overrightarrow{\nabla} \times (\overrightarrow{\nabla} \times \overrightarrow{E}) &= -\frac{\partial}{\partial t}(\overrightarrow{\nabla} \times \overrightarrow{B}) \\
\overrightarrow{\nabla}(\overrightarrow{\nabla} \cdot \overrightarrow{E}) - \nabla^2 E &= -\frac{\partial}{\partial t}(\overrightarrow{\nabla} \times \mu\overrightarrow{H}) \\
&= -\mu\frac{\partial}{\partial t}(\overrightarrow{\nabla} \times \overrightarrow{H}) \\
&= -\mu\frac{\partial^2 D}{\partial t^2} \\
&= -\mu\epsilon\frac{\partial^2 E}{\partial t^2}.
\end{aligned}$$

Then, since $\overrightarrow{\nabla} \times \overrightarrow{E} = 0$ from Equation A.3, we know that

$$\nabla^2 E = \mu\epsilon\frac{\partial^2 E}{\partial t^2}. \tag{A.6}$$

A similar application of the curl operator to Equation A.2 yields

$$\nabla^2 H = \mu\epsilon\frac{\partial^2 H}{\partial t^2}. \tag{A.7}$$

Equations A.6 and A.7 are both of the form of standard wave equations, where the second spacial derivative of a function is proportional to the second temporal derivative. Therefore, we know that solutions to these equations can be written in the form of sums of sines and cosines.

A.3 Waves in a waveguide

We now proceed to analyse the propagation of waves in an infinite cylindrical waveguide. Figure A.1 shows the coordinate system of $\{\rho, \phi, z\}$.

In the cylindrical coordinate system, $\overrightarrow{E}$ and $\overrightarrow{H}$ have the forms

$$\overrightarrow{E} = \overrightarrow{E_0}(\rho, \phi)\exp[j(\omega t - \beta z)] \tag{A.8}$$

$$\overrightarrow{H} = \overrightarrow{H_0}(\rho, \phi)\exp[j(\omega t - \beta z)] \tag{A.9}$$

where β is the z component of the propagation vector, determined by the boundary conditions. This will be demonstrated shortly, but first, to establish that $\overrightarrow{E}$ and $\overrightarrow{H}$ take the forms given in Equations A.8 and A.9, we substitute these solutions into the cylindrical coordinate version of Maxwell's equations.

Equation A.1 yields

$$\frac{1}{\rho}(\frac{\partial E_z}{\partial \phi} + j\rho\beta E_\phi) = -j\omega\mu H_\rho, \tag{A.10}$$

$$j\beta E_\rho + \frac{\partial E_z}{\partial \rho} = j\omega\mu H_\phi, \tag{A.11}$$

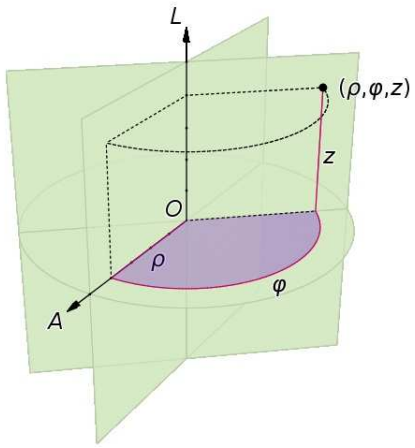

Figure A.1: Cylindrical coordinate system.

and

$$\frac{1}{\rho}[\frac{\partial}{\partial\rho}(\rho E_\phi) - \frac{\partial E_\rho}{\partial\phi}] = -j\mu\omega H_z. \tag{A.12}$$

Equation A.2 yields

$$\frac{1}{\rho}(\frac{\partial H_z}{\partial\phi} + j\rho\beta H_\phi) = -j\omega\mu E_\rho, \tag{A.13}$$

$$j\beta H_\rho + \frac{\partial H_z}{\partial\rho} = j\omega\mu E_\phi, \tag{A.14}$$

and

$$\frac{1}{\rho}[\frac{\partial}{\partial\rho}(\rho H_\phi) - \frac{\partial H_\rho}{\partial\phi}] = -j\mu\omega E_z. \tag{A.15}$$

By eliminating variables, these equations can be rewritten such that, when E_z and H_z are known, all of the transverse components $(E_\rho, E_\phi, H_\rho, H_\phi)$ can be determined.

This yields:

$$E_\rho = -\frac{j}{q^2}(\beta\frac{\partial E_z}{\partial\rho} + \frac{\mu\omega}{\rho}\frac{\partial H_z}{\partial\phi}) \tag{A.16}$$

$$E_\phi = -\frac{j}{q^2}(\frac{\beta}{\rho}\frac{\partial E_z}{\partial\phi} - \mu\omega\frac{\partial H_z}{\partial\rho}) \tag{A.17}$$

$$H_\rho = -\frac{j}{q^2}(\beta\frac{\partial H_z}{\partial\rho} - \frac{\omega\epsilon}{\rho}\frac{\partial E_z}{\partial\phi}) \tag{A.18}$$

$$H_\phi = -\frac{j}{q^2}(\frac{\beta}{\rho}\frac{\partial H_z}{\partial\phi} + \omega\epsilon\frac{\partial E_z}{\partial\rho}) \tag{A.19}$$

where $q^2 \equiv \omega^2\epsilon\mu - \beta^2 = k^2 - \beta^2$.

Substituting Equations A.18 and A.19 into Equation A.15 yields

$$\frac{\partial^2 E_z}{\partial \rho^2} + \frac{1}{\rho}\frac{\partial E_z}{\partial \rho} + \frac{1}{\rho^2}\frac{\partial^2 E_z}{\partial \phi^2} + q^2 E_z = 0, \tag{A.20}$$

and substituting Equations A.16 and A.17 into Equation A.12 yields

$$\frac{\partial^2 H_z}{\partial \rho^2} + \frac{1}{\rho}\frac{\partial H_z}{\partial \rho} + \frac{1}{\rho^2}\frac{\partial^2 H_z}{\partial \phi^2} + q^2 H_z = 0. \tag{A.21}$$

These are forms of the wave equation in cylindrical coordinates, as desired.

Although these equations appeared to be uncoupled – functions of either E_z or H_z – both equations respect boundary conditions, and when boundary conditions allow E and H to remain uncoupled, then we can get mode solutions in which either $E_z = 0$ or $H_z = 0$. These are known as, respectively, transverse electric (TE) and transverse magnetic (TM) modes. We get hybrid modes when E_z and H_z are non-zero. Hollow metallic waveguides support TE and TM modes of propagation while dielectric fibres and optical waveguides support additional hybrid modes.

A.4 Wave equations for step-index fibre

To solve these wave equations we use separation of variables. We 'guess' a solution of the form

$$E_z = AF_1(\rho)F_2(\phi)F_3(z)F_4(t).$$

We already know that $F_3(z)F_4(t) = exp[j(\omega t - \beta z)]$. We also know that a circular waveguide demands that $F_2(\phi) = exp(j\nu\phi)$ with $\nu \in \mathbb{Z}$ since advancing ϕ by 2π should return the same value[1]. Thus the wave equation becomes

$$\frac{\partial^2 F_1}{\partial \rho^2} + \frac{1}{\rho}\frac{\partial F_1}{\partial \rho} + (q^2 - \frac{\nu^2}{\rho^2})F_1 = 0. \tag{A.22}$$

This is a differential equation whose solutions are Bessel functions. The same analysis holds for H_z. Step index fibres have a core of radius a with a uniform refractive index and a cladding layer with a lower refractive index. For regions inside the core, the solutions are finite as the radius r $\to$ 0. Outside of the core, the solutions $\to$ 0 as r $\to \infty$.

Thus for r $\leq$ a, the solutions are Bessel functions of the first kind of order ν. For these solutions we use the designator $J_\nu(ur)$ where $u^2 = k_1^2 - \beta^2; k_1 = \frac{2\pi n_1}{\lambda}$.

Inside of the core

$$E_z(r < a) = AJ_\nu(ur)\exp(j\nu\phi)\exp[j(\omega t - \beta z)]$$
$$H_z(r < a) = BJ_\nu(ur)\exp(j\nu\phi)\exp[j(\omega t - \beta z)].$$

[1]This result is a consequence of Euler's identity: $e^{i\pi} = -1 \implies e^{2i\pi} = 1 \implies e^{2i\pi n} = 1$ for $n \in \mathbb{Z}$.

Outside of the core the solutions to the wave equation are modified Bessel functions of the second kind: $K_\nu(wr)$, where $w^2 = \beta^2 - k_2^2; k_2 = \frac{2\pi n_2}{\lambda}$.

Thus outside of the core

$$E_z(r > a) = CK_\nu(wr)\exp(j\nu\phi)\exp[j(wt - \beta z)]$$
$$H_z(r > a) = DK_\nu(wr)\exp(j\nu\phi)\exp[j(wt - \beta z)].$$

From the definitions of the modified Bessel functions, we know that $K_\nu(wr) \to e^{-wr}$ as $wr \to \infty$. Therefore $w > 0$ since we know that $K_\nu \to 0$. Thus we know that $\beta \geq k_2$.

This gives us a cut-off condition for β.

Inside of the core, u is real if F_1 is to be real, so $k_1 \geq \beta$.

Thus, the β of bound solutions is:

$$n_2 k = k_2 \leq \beta \leq k_1 = n_1 k,$$

where $k = \frac{2\pi}{\lambda}$.

Now we have cut-off conditions for β but actual solutions come from the boundary conditions. These boundary conditions are as follows:

1. The tangential components E_ϕ and E_z have the same value at $r = a$.
2. The tangential components H_ϕ and H_z have the same value at $r = a$.

We'll start with $\overrightarrow{E}$.

We know that

$$E_{z1} - E_{z2} = AJ_\nu(ua) - CK_\nu(wa) = 0. \tag{A.23}$$

The ϕ component is found from Equation A.17:
Inside of the core, $q^2 = u^2 = k_1^2 - \beta^2$
where $k_1 = \frac{2\pi n_1}{\lambda} = w\sqrt{\epsilon_1\mu}$.
Outside of the core, $w^2 = \beta^2 - k_2^2$
where $k_2 = \frac{2\pi n_2}{\lambda} = w\sqrt{\epsilon_2\mu}$.
We use the Bessel function solutions into A.17 to get

$$\begin{aligned} E_{\phi 1}(r = a) - E_{\phi 2}(r = a) = &-\frac{j}{u^2}[A\frac{j\nu\beta}{a}J_\nu(ua) - B\omega\mu u J'_\nu(ua)] \\ &- \frac{j}{w^2}[C\frac{j\nu\beta}{a}K_\nu(wa) - D\omega\mu w K'_\nu(wa)] \quad = 0. \end{aligned} \tag{A.24}$$

Similarly for $\overrightarrow{H}$ at $r = a$:

$$H_{z1} - H_{z2} = BJ_\nu(ua) - DK_\nu(wa) = 0. \tag{A.25}$$

And

$$H_{\phi 1}(r=a) - H_{\phi 2}(r=a) = -\frac{j}{u^2}[B\frac{j\nu\beta}{a}J_\nu(ua) + A\omega\epsilon_1 u J'_\nu(ua)] \\ - \frac{j}{w^2}[D\frac{j\nu\beta}{a}K_\nu(wa) + C\omega\epsilon_2 w K'_\nu(wa)] \quad = 0. \quad \text{(A.26)}$$

Equations A.23, A.24, A.25, and A.26 are 4 equations with 4 unknown coefficients. Thus a solution exists if and only if the determinant of the 4 coefficients equals 0.
Evaluation of the determinant yields an eigenvalue equation for β:

$$(J_\nu + K_\nu)(k_1^2 J_\nu + k_2^2 K_\nu) = (\frac{\beta\nu}{a})^2(\frac{1}{u^2} + \frac{1}{w^2})^2 \quad \text{(A.27)}$$

where $J_\nu = \frac{J'_\nu(ua)}{uJ_\nu(ua)}$ and $K_\nu = \frac{K'_\nu(wa)}{wK_\nu(wa)}$.

The solution to Equation A.27 yields only discrete values within the given range allowed, thus confirming that only finite modes are allowed to propagate within step-index fibres with the above specifications.

Bibliography

[1] *Mode hopping*, Encyclopedia of Laser Physics and Technology.

[2] A.G.Hallam, D.A.Robinson, and I.Bennison, *Mode Control for Emerging Link Performance Standards*, IET Optoelectronics (2009), 1–8.

[3] G Aquelos and et al, *Impact of energy and luminosity upgrades at LHC on the physics programme of ATLAS*, Journal of Physics G: Nuclear and Particle Physics **28** (2002), 2453–2474.

[4] B. Arvidsson, K. Dunn, C. Issever, B.T. Huffman, M. Jones, J. Kierstead, G. Kuyt, T. Liu, A. Povey, E. Regnier, A.R. Weidberg, A. Xiang, and J. Ye, *The radiation tolerance of specific optical fibres exposed to 650 kGy(Si) of ionizing radiation*, Journal of Instrumentation **7** (2009).

[5] Francis Berghmans, Benoit Brichard, Alberto Fernandez, Andrei Gusarov, Marco van Uffelen, and Sylvain Girard, *An Introduction to Radiation Effects on Optical Components and Fiber Optic Sensors*, Optical Waveguide Sensing and Imaging (2008), 127–165.

[6] ATLAS Collaboration, *The ATLAS Experiment at the CERN Large Hadron Collider*, JINST **3** (2008).

[7] G. Coppa and P. DiVita, *Effects of joints on mode power distribution and losses in multimode optical fibres*, Optical and Quantum Electronics **15** (1983), 143–153.

[8] I Dawson, *The SLHC prospects at ATLAS and CMS*, Journal of Physics: Conference Series (2008).

[9] I. Dawson and L. Nicolas, *Radiation Background Issues For the Upgrade Inner Tracker*, (2008), 1–21.

[10] K Dunn, BT Huffman, C Issever, A Povey, and Tony Weidberg, *Fibre tests – optical properties: Summer 2008*, Tech. report, 2008.

[11] LB Felson, *Rays and modes in optical fibres*, Electronics Letters **10** (1974), no. 7, 95–96.

[12] E Joseph Friebele, Peter B Lyons, James Blackburn, Henning Henschel, Alain Johan, Jeffrey A Krinsky, Alan Robinson, Schneider, Smith, and Taylor, *Laboratory Comparison of Radiation-Induced Attenuation in Optical Fibers. Part III: Transient Exposures*, Journal of Lightwave Technology **8** (1990), no. 6, 977–989.

[13] EJ Friebele, EW Taylor, G Turguet de Beauregard, JA Wall, and CE Barnes, *Interlaboratory comparison of radiation-induced attenuation inoptical fibers. I. Steady-state exposures*, Journal of Lightwave Technology **6** (1988), no. 2, 165–171.

[14] K Gan, B Abi, W Fernando, H Kagan, and R Kass, *Radiation-hard/high-speed data transmission using optical links*, Nuclear Instruments and Methods in Physics Research (2009).

[15] K Gan, W Fernando, H Kagan, R Kass, and A Law, *Radiation-hard optical link for SLHC*, Nuclear Inst. and Methods (2008).

[16] KK Gan, W Fernando, HP Kagan, RD Kass, A Law, MRM Lebbai, PL Skubic, and DS Smith, *Bandwidths of micro twisted-pair cables and fusion spliced SIMM-GRIN fiber and radiation hardness of PIN/VCSEL arrays*, Nuclear Physics B (Proceedings Supplements) **172** (2007), 190–193.

[17] KK Gan, Karl Gill, Jan Troska, Francois Vasey, Todd Huffman, Cigdem Issever, Tony Weidberg, Jingbo Ye, Pat Skubic, Rusty Boyd, and Flera Fizatdinova, *Joint ATLAS-CMS working group on optoelectronics for SLHC: Report from sub-group B Optical System Irradiation Guidelines*, Tech. report.

[18] D Goff, *Fiber optic reference guide*, Jan 2002.

[19] MJ Hackert, *Evolution of power distributions in fiber optic systems: Development of a measurement strategy*, Fiber and Integrated Optics **8** (1989), no. 2, 163–267.

[20] MG Hajra, K Mehta, and GG Chase, *Effects of humidity, temperature, and nanofibers on drop coalescence in glass fiber media*, Separation and Purification Technology **30** (2003), 79–88.

[21] Henning Henschel and Eduard Baumann, *Effect of Natural Radioactivity on Optical Fibers of Undersea Cables*, Journal of Lightwave Technology **14** (1996), no. 5, 724–731.

[22] N Hessey, *ATLAS and CMS Detector Upgrades for sLHC*, Physics at LHC 2008 (2008).

[23] TA Heumier and JL Carlsten, *Mode hopping in semiconductor lasers*, ILX Lightwave Corporation (2005), no. 8.

[24] Y Hibino, *Silica-based planar lightwave circuits and their applications*, MRS Bulletin (2003).

[25] A Himeno, K Kato, and T Miya, *Silica-based planar lightwave circuits*, IEEE Journal of Selected Topics in Quantum Electronics (1998).

[26] Dr. Todd Huffman, personal communication, 2010.

[27] Akira Ilno and Junich Tamura, *Radiation Resistivity in Silica Optical Fibers*, Journal of Lightwave Technology **6** (1988), no. 2, 145–149.

[28] C Issever, *Readout systems for inner detectors at the LHC and SLHC*, Nuclear Inst. and Methods in Physics Research, A **569** (2006), no. 1, 77–79.

[29] H Kanamori, H Yokota, G Tanaka, M Watanabe, Y Ishiguro, I Yoshida, T Kakii, S Itoh, Y Asano, and S Tanaka, *Transmission characteristics and reliability of pure-silica-core single-mode fibers*, Journal of Lightwave Technology **4** (1986), no. 8, 1144–1150.

[30] Hiroo Kanamori, Hiroshi Yokota, Gotaro Tanaka, Minoru Watanabe, Yoichi Ishiguro, Ichiro, Yoshida, Toshiaki, Kakii, Shigeru Itoh, Yasuo Asano, and Shigeru Tanaka, *Transmission Characteristics and Reliability of Pure-Silica-Core Single-Mode Fibers*, Journal of Lightwave Technology **LT-4** (1986), no. 8, 1144–1150.

[31] Gerd Keiser, *Optical Fiber Communications*, 2000.

[32] Mike Letheren and Francois Vasey, *Electronics for the LHC-era experiments and beyond*, CERN Courier (2008).

[33] Paolo Morettini, PANIC 08, 2008.

[34] E Neumann, *Single-mode fibers: Fundamentals*, 1988.

[35] Newport, *Fiber Tutorial*, Photonics (2002), 1–5.

[36] Alain Pham, *Planar lightguide circuits: An emerging market for refractive index profile analysis*, (2004), 1–6.

[37] R Richter, *Upgrade of ATLAS for high luminosity at the SHLC*, 2008.

[38] Piet J W Severin and Wim H Bardoel, *Differential mode loss and mode conversion in passive fiber components measured using the chromatic launching and the central spot far field techniques*, Journal of Lightwave Technology **LT-4** (1986), no. 11, 1640–1646.

[39] A. K. Shrivastava, *Effect of Low Temperature on Mechanical Properties of Bidirectional Glass Fiber Composites*, Journal of Composite Materials **42** (2008), no. 22, 2407–2432.

[40] L Slifkin, *Dynamics of self-trapped hole processes in AgCl*, Journal of Physics: Condensed Matter **13** (2001), 2347–2353.

[41] W Smith, *Physics and Detectors at the LHC and the SLHC*, Arxiv preprint hep-ex (2005).

[42] R. Steel and J. Torrie, *Principles and procedures of statistics*, (1960).

[43] A Strässner and the ATLAS collaboration, *Development of new readout electronics for the ATLAS LAr calorimeter at the sLHC*, Imprint (2009).

[44] H Takahashi, *Planar lightwave circuit devices for optical communication: present and future*, Proc. of SPIE Vol.

[45] Edward W Taylor, E Joseph Friebele, Henning Henschel, Ronald H West, Jeffrey A Krinsky, and CE Barnes, *Interlaboratory Comparison of Radiation-Induced Attenuation in Optical Fibers. Part II: Steady-State Exposures*, Journal of Lightwave Technology **8** (1990), no. 6, 967–976.

[46] Sylvain Theriault, *Radiation effects on COTS laser-optimized graded-index multimode fibers exposed to intense gamma radiation fields.*

[47] A Tricomi, *SLHC: The LHC luminosity upgrade*, Nuclear Inst. and Methods in Physics Research (2008).

[48] Francois Vasey, Jan Troska, Christian Olivetto, Jean-Marie Brom, Cigdem Issever, Todd Huffman, Tony Weidberg, and Jingbo Ye, *The Versatile Link Common Project*, Tech. Report V2.2, 16.

[49] M Weber, *SLHC upgrades: challenges and strategies in ATLAS*, Proceedings of the The 16th International Workshop on Vertex Detectors (2007).

[50] Quan Yu, Paul-Hubert Zongo, and Paul Facq, *Refractive-index profile influences on mode coupling effects at optical fiber splices and connectors*, Journal of Lightwave Technology **11** (1993), no. 8, 1270–1273.